


U.S. DEPARTMENT OF ENERGY
Office of Energy Efficiency and Renewable Energy (EERE)
Water Power Technologies Office (WPTO)
Lab Collaboration Project (LCP) for Marine Energy
Task 10: Quantifying Collision Risk for Fish and Turbines
Final Technical Report

Award Number: DE-EE-0006816.0000
Originating FOA: DE-FOA-0001098: Marine and Hydrokinetic Research and Development University Consortium; LCP: DNFA
Recipient: Oregon State University
Principal Investigator: Dr. Bryson Robertson, Bryson.robertson@oregonstate.edu, (541) 737-8286
Project Objectives: Accelerate the development of next-generation marine energy conversion systems.
Date of Report: July 2024
Project Period: 8/3/2018 – 6/30/2024
OSU DUNS Number: 053599908

Report Submitted By: Jennifer Thornhill, jennifer.thornhill@oregonstate.edu, (541) 737-9012

Signature: 
Bryson Robertson, PMEC Co-Director

Recipient Team and Partners:

Name	Organization & Title	Project Role	Email	Phone
Dr. Bryson Robertson	Oregon State University PMEC Co-Director	Principal Investigator	bryson.robertson@oregonstate.edu	(541) 737-8286
Dr. Ted Brekken	Oregon State University Task 11 Lead PI	Co-PI	Ted.brekken@oregonstate.edu	(541) 737-2995
Dr. Brian Polagye	University of Washington, PMEC Director	Co-PI	bpolagye@u.washington.edu	(206) 543-7544
Dr. Jeremy Kasper	University of Alaska Fairbanks PMEC Co-Director	Co-PI	jkasper@alaska.edu	(907) 474-5694

DOE Team: Water Power Technologies Office

Name	Title/Role	Email	Phone
William McShane	DOE Technology Manager	William.mcshane@ee.doe.gov	202-586-6396
Yana Shiningier	DOE Technical Project Officer	Yana.shiningier@ee.doe.gov	240-562-1376
Michael Carella	Project Monitor	Michael.carella@ee.doe.gov	240-562-1323
Laura Merrick	DOE Contract Officer	Laura.merrick@ee.doe.gov	240-562-1698
Jane Sanders	DOE Grants Mgmt. Specialist	Jane.sanders@ee.doe.gov	240-562-1771

ALFA Task 10: Quantifying Collision Risk for Fish and Turbines

Section Authorship

- *Section 1: Introduction and Overview*: Brian Polagye (UW)
- *Section 2: Task 10.1: Fish Collision*: Chris Bassett (UW), Mitchell Scott (UW/MarineSitu), Emma Cotter (PNNL/UW), James Joslin (MarineSitu), and Brian Polagye (UW)
- *Section 3: Task 10.1: Acoustic Characterization*: Lindsey Jones (UW), Brian Poagye (UW), and Chris Bassett (UW)
- *Section 4: Task 10.2: Velocity Field Characterization*: Brian Polagye (UW), Greg Talpey (UW), Abigale Snortland (UW)
- *Section 5: Task 10.3: Behavioral Evaluation*: Kyle Newton (OSU), Mitchell Scott (UW/MarineSitu), and Sarah Henkel (OSU)
- *Section 6: Task 10.4: Collision and Encounter Risk Modeling*: Jezella Peraza (UW) and John Horne (UW)
- *Section 7: Conclusions*: Brian Polagye (UW) and Chris Bassett (UW)

1 Introduction and Overview

A persistent environmental concern for the widespread deployment of tidal turbines is the potential for fish and marine mammals to collide with rotating blades (Copping et al. 2016, Copping and Hemery 2020). This is a consequence of well-documented bird and bat mortalities around wind turbines (Smallwood 2007, Thompson et al. 2017), as well as fish mortality at conventional hydropower dams (Pracheil et al. 2016) and tidal barrages (Dadswell and Rulifson 1994). However, unlike hydropower dams or barrages, tidal turbines do not involve structures that channel all flow through the turbines. Similarly, while functionally similar to wind turbines, tidal turbines often operate at lower relative velocities and, depending on the end-use application, may be significantly smaller than utility-scale wind turbines. Both of these factors reduce the likelihood and severity of collision, but the knowledge base on this topic remains limited.

The objective of this task was to add to that knowledge base in four areas:

1. To collect data on fish interactions with an operating tidal turbine;
2. To contextualize these interactions with the changes the turbine makes to the physical environment – specifically, the proximate flow disturbance and radiated noise that are a consequence of energy harvesting;
3. To interpret the behavior of fish interacting with the turbine and how this could increase or mitigate collision risk; and
4. To employ models for these interactions that could be used in a predictive manner at other locations.

The project was initiated in 2017 as a collaboration between Pacific Northwest National Laboratory (PNNL) and PMEC researchers at the University of Washington (UW) and University of Alaska Fairbanks (UAF). Fish interactions were to be monitored around a pair of cross-flow turbines with a rated power output of 1 kW that were to be deployed in Sequim Bay, WA at PNNL's Marine & Coastal Research Laboratory (MCRL). Because of uncertainties about the ability of optical or active acoustic sensors to detect and track individual fish targets in close proximity to the turbine rotor (Cotter and Polagye 2020),

PNNL planned to implant JSATS tags (McMichael et al. 2010) in a representative fish species that would allow individual fish to be tracked with high precision.

The project deviated from this initial plan in several ways.

First, during the initial phase of the project, PNNL tagged 100 juvenile sablefish and released them upstream of an Adaptable Monitoring Package (AMP, Polagye et al. 2020) deployed at the intended turbine location at MCRL. However, only one of these fish definitively entered the field of view for the AMP's imaging sonars and none entered the camera field of view. Because of this, it was determined that an infeasibly large number of fish would need to be tagged for a reasonable sample size of released fish to interact with the turbine rotor. Consequently, this activity was removed from the project scope.

Second, the turbine deployment was substantially delayed relative to the initial timeline for multiple reasons. The turbine was a prototype cross-flow device on a gravity lander being developed by UW with parallel support from the Department of Defense's Naval Facilities and Engineering Systems Command (NAVFAC). The engineering development of this system took substantially longer than anticipated, such that the first system test with a fully submersible power take-off unit did not occur until summer 2020, two years after the initial deployment target at MCRL. In addition, NEPA and permitting processes took substantially longer than anticipated. Key issues involved a delay of nearly two years for one resource agency's Endangered Species Act consultation and protracted legal discussions over relatively minor points between UW, PNNL, and the Department of Natural Resources on the terms of the seabed lease for turbine deployment. Because of this, a decision was made in early 2022 to conduct the data collection aspect of the project around an endurance test for the turbine in Agate Pass, WA with the turbine deployed from a moored vessel.

Third, because of the project delays, UAF was unable to identify staff or students to conduct the behavioral evaluation of data from the Agate Pass deployment. Consequently, this portion of the scope was transferred to researchers at Oregon State University (OSU).

Despite these challenges and changes, the task was successful in meeting many of its objectives.

Important outcomes included:

- Demonstrated automated trajectory tracking of small fish targets using stereo-optical cameras and machine learning;
- An increased understanding of the capabilities and limitations of optical and acoustic systems for tracking fish around tidal turbines;
- A novel method for hypothesizing potential radiated noise from a deployed turbine and successful employment of acoustic localization of radiated noise in a tidal channel;
- An understanding of the extent and magnitude of flow field disturbances around cross-flow turbines;
- A framework for quantifying collision risk using physical attributes of marine animal motion relative to a turbine; and
- Statistical and agent-based evaluations of encounter and collision risk, assessing sensitivity to key parameters.

In addition, several of the approaches developed under this project were employed during the eventual turbine deployment at MCRL.

This report is broken down into five sections, each of which describes a functional subtask:

- Task 10.1: Fish Interaction with a Turbine: Field data collection of fish trajectories, including the baseline tracking of fish implanted with JSATS tags, cooperative target testing during turbine

shakedown tests, and development of automatic detection and tracking capabilities for optical data streams

- Task 10.1: Acoustic Characterization: Acoustic measurements around the turbine deployment in Agate Pass, contextualized by close range measurements of the turbine being motored in a dockside setting
- Task 10.2: Velocity Field Characterization: Hydrodynamic disturbances around a laboratory-scale model of the field turbine, measured using Particle Image Velocimetry
- Task 10.3: Behavioral Evaluation: Development and preliminary application of a model framework that can assign a collision risk based on quantitative metrics derived from
- Task 10.4: Collision and Encounter Risk Modeling: Development and application of statistical and agent-based simulation to predict the likelihood of collision risk

2 Task 10.1: Field Data Collection: Fish Interaction with a Turbine

2.1 Introduction

The objective of this task was to develop and demonstrate techniques that could automatically detect and track fish around tidal turbines, using optical and acoustic imagery. The analysis focused on a data set collected in Agate Pass, WA over a 10-day period during an endurance test for a cross-flow turbine. During this test, the turbine was suspended from a moored platform and observed with optical cameras and active sonars.

2.2 Methods

2.2.1 Cross-flow Turbine and Deployment Platform

The turbine was a cross-flow variant developed by the University of Washington with a rotor 1.19 m tall and 0.85 m in diameter. The rotor consisted of four straight blades with a blade chord length of 0.098 m. Four struts with cross-sections roughly matching the chord length connected the blades to the drive shaft. The rotor was coupled to a generator using an oil-filled bearing pack and a magnetic coupling. As configured for deployment on *R/V Russell Davis Light* (RDL), the rotor was cantilevered below the generator housing and bearing pack (Figure 1 and Figure 2).

RDL was designed primarily for testing tidal turbines and used to test the turbine on Lake Washington and in Agate Pass (tidal channel adjacent to the main basin of Puget Sound). RDL is a 20 m long, dual-hull vessel with a wheelhouse located near the stern. Between the hulls, near the bow, an open section of the deck hosts a gantry/frame system to which various pieces of equipment can be mounted. This system can be used to lower equipment approximately 2.5 m, placing it below the region disturbed by the vessel's hulls and enabling turbines to be "tow tested" by driving the vessel in quiescent water to simulate natural currents. Likewise, the vessel can be moored in areas with strong currents to test turbines in natural currents. The testing described in the subsequent sections uses both of these approaches.

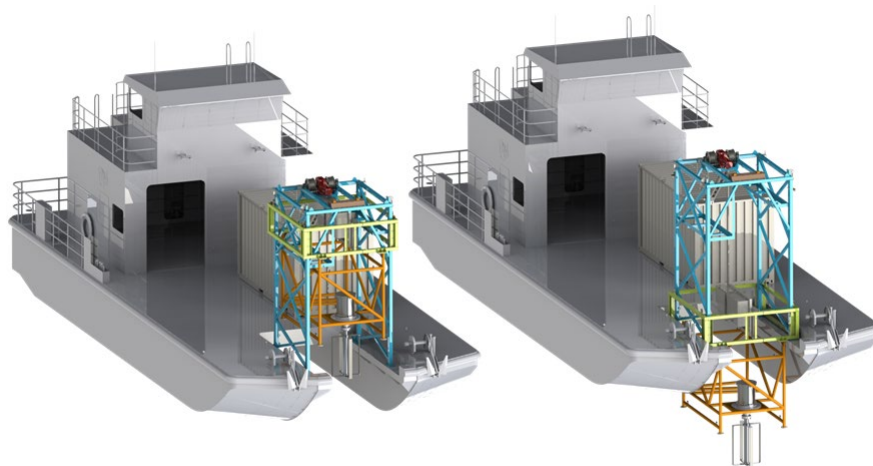


Figure 1: A rendering of R/V Russel Davis Light showing its forward gantry with UW's cross flow turbine in the position for transit and storage (right) and testing under propulsion or moored (left). The wheelhouse is set up and towards the stern.

During tests, the turbine rotor and PTO are deployed forward near the bow of the vessel and undisturbed inflow conditions are measured by acoustic Doppler instrumentation mounted forward of

the rotor. Any additional equipment for optical or acoustic monitoring of the rotor is generally installed aft of the rotor, primarily due to overall space constraints. From all instruments, cables run along various support structures on the gantry to a shipping container office that serves as a data collection station. In this configuration, the rotor and generator housing were submerged such that the top of the generator housing and rotor are approximately 0.2 m and 1 m below the surface, respectively.



Figure 2: A picture of the Turbine Lander rotor and PTO installed on RDL prior to testing in Agate Pass, WA.

Previous characterization of the rotor carried out on RDL has been used to estimate the turbine's water-to-wire efficiency (Figure 3), while other laboratory dynamometry tests have been performed to characterize PTO system inefficiencies and estimate the rotor's coefficient of performance. The turbine's cut-in speed is approximately 1 m/s and its rated speed is approximately 2.5 m/s. Water-to-wire efficiencies increase from near 0% around cut-in speed due to losses in the system and peak near 25% around the rated speed. Tip-speed ratios vary between 1.8 and 2.1 across the operational range. This corresponds to rotation rates between approximately 60-110 rpm for conditions between the cut-in and rated speeds. The turbine's efficiency increases with inflow condition due to increased blade-level performance at higher Reynolds number and a reduction in the relative contribution of fixed system losses.

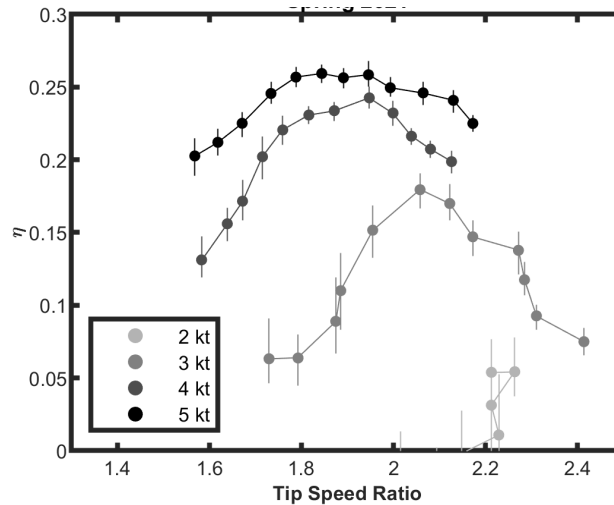


Figure 3: Water-to-wire efficiency vs tip speed ratio for four vessel speeds. These data are from system testing aboard RDL in spring 2021. Scatter in the figures is associated with challenges in maintain targeted speeds and headings during testing. 1 knot (kt) corresponds to 0.514 m/s.

2.2.2 Adaptable Monitoring Package (AMP)

During vessel-based testing, environmental measurements are made using a variant of the Adaptable Monitoring Package (AMP) (Polagye et al. 2020). The AMP allows for integrated measurements and data acquisition of data streams from a broad range of sensors, which can be customized to meet the needs of specific applications. Sensing packages employed in prior AMP deployments have included acoustic Doppler profilers, hydrophone arrays, numerous imaging sonars, stereo optical camera systems, echosounders, and ancillary components to mitigate biofouling and to adjust the orientation (pitch) of the sensors. Figure 4 shows a picture of an AMP prior to deployment in Sequim Bay, while Table 1 includes a summary of the instruments used in different AMP deployments described in this report.



Figure 4. The 3G-AMP prior to deployment in Sequim Bay. The sensor package includes stereo-optical cameras, an echosounder, two imaging sonars, an ADCP, and a hydrophone array. Biofouling mitigation (mechanical wipers and UV lighting) are integrated with most sensors and the pitch angle of the sensors can be adjusted by an internal motor.

Table 1: Instrument configurations for AMP deployments. Instrument settings are generally modified throughout deployments based on changes in environmental conditions and between deployments based on objectives.

Deployment	Instruments
MCRL	Acoustic Doppler current profiler, stereo optical cameras and associated lights, Trittech Gemini, BlueView, hydrophone array
Lake Washington	Acoustic Doppler current profiler, stereo optical cameras and associated lights, Trittech Gemini, BlueView
Agate Pass	Acoustic Doppler current profiler, stereo optical cameras and associated lights, Trittech Gemini ¹ , BlueView (x2).

2.2.3 Sequim Bay: Tagged Fish Evaluation

An initial test was conducted in in Sequim Bay, WA in collaboration with Pacific Northwest National Laboratory prior to any turbine installation in March 2019. This activity was intended to inform (1) preferred methods for fish release, (2) the behavior of the fish following release, and (3) the effectiveness of different sensor systems for detecting and tracking the fish. Two sensor systems were used to monitor the released fish: the Juvenile Salmon Acoustic Telemetry System (JSATS) deployed by

¹ Although deployed, data from the Trittech Gemini was not analyzed because of poor data quality associated with a suboptimal configuration that was driven by space limitations.

PNNL and the AMP deployed by UW. JSATS is a fish tracking system that uses an array of hydrophones to track fish that have been implanted with an acoustic transmitter. Table 2 provides details the AMP sensors of interest for detecting the released fish. Using the AMP's integrated pitch motor, the angle of the instrument head was adjusted over the course of the fish releases to improve the signal-to-noise ratio in the active acoustic data streams by minimizing the interference from the intersection of the sonar swaths with the water surface and seafloor. Because of weakness of the AMP sensors is that it is not possible to reliably discriminate between fish and debris using only multibeam sonars, data from the AMP sensors were reviewed for time periods when the JSATS tracking system reported that a tagged fish could be within the field of view.

Table 2: AMP sensors during tagged fish releases.

Instrument Type	Instrument Make and Model	Field of View
Multibeam sonar	BlueView M900-2250	130° horizontal swath, 20° vertical swath, 10 m maximum range
Multibeam sonar	Tritech Gemini 720is	120° horizontal swath, 20° vertical swath, 150 m maximum range (sensor was operated at 10 and 20 m ranges during testing)
Optical Camera	Allied Vision Manta 507	~54° conical swath, range of visibility varies with light and water clarity. 5 m maximum range used to isolate potential concurrent detections with JSATS.

JSATS detection data were provided by PNNL, and included the time, fish tag ID, GPS coordinate, and depth of each detection. To select JSATS detections that were potentially detectable by the AMP sensors, the JSATS detection data were first shifted to the AMP coordinate system (position relative to the AMP given the rotation angle of the AMP instrument head). The JSATS detections were then grouped into "tracks" – detections of the same fish separated in time by 5 seconds or less. The list of tracks was then trimmed to only include those that passed through the field-of-view of an AMP sensor. Following this, a 60-second window of AMP sensor data centered around each potential concurrent detection was manually reviewed.

An exception to this review was the track associated with fish tag ID G724633CD, which produced over 3000 detections within the AMP field-of-view over a 2-hour period on March 29, 2019. Figure 5 shows a representative segment of this track. The reported depth of the fish (bottom panel) instantaneously jumps between approximately 11 m and 4 m depth. The limited variation in horizontal position suggests that the fish was taking refuge near the seafloor (depth of approximately 11 m), a position where it would not be detectable by the AMP sensors, and the jumps in depth are the result of ambiguity in the acoustic localization.

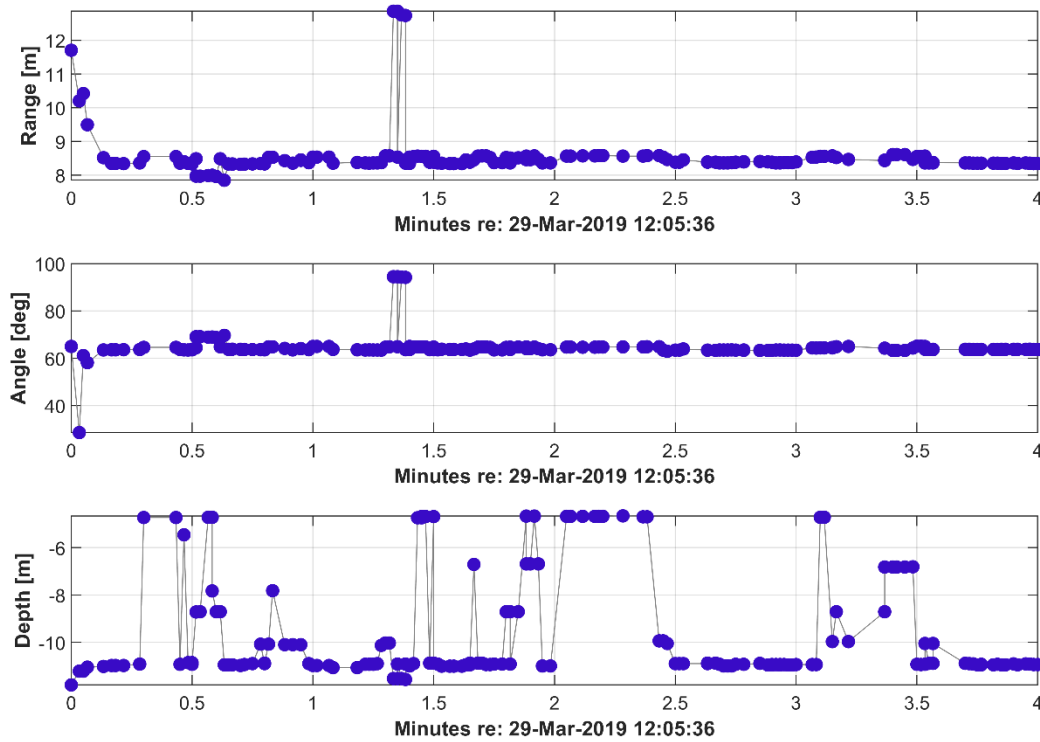


Figure 5: 4-minute representative window of the track from fish tag G724633CD on March 29, 2019. The top and middle panels shows the range and angle of the reported JSATS detection from the AMP in the horizontal plane (calculated using GPS position), and the bottom panel shows the depth of the fish reported by the JSATS array.

2.2.4 Lake Washington: Cooperative Target Evaluation

Lake Washington serves as a local test facility for in-water testing of field-scale turbines. Lake Washington is located just east of the University of Washington and the Applied Physics Laboratory's vessel moorage in Seattle. The surface area of Lake Washington exceeds 33 km² and its average depth is greater than 30 m. Thus, the large lake provides the opportunity for vessel-propelled testing of field-scale turbines during which the inflow conditions can be held roughly constant by maintaining a specific heading.

For cooperating target testing, RDL was equipped with the turbine rotor and power take-off, in addition to a stripped-down, more compact version of the 3G-AMP (Polagye et al. 2020), referred to as the "vessel AMP" or VAMP. The VAMP included Blueview and Tritech Gemini imaging sonars, as well as a stereo optical camera system (Table 1). To avoid disturbing the inflow to the turbine during vessel-propelled testing, these instruments were mounted aft of the rotor. Inflow velocities were measured using an acoustic Doppler velocimeter (Nortek Vector) deployed forward of the rotor.

At the start of this project, while versions of the AMP had been previously deployed several times in Sequim Bay (Polagye et al. 2020), data had not yet been acquired in the vicinity of a tidal turbine. Furthermore, during prior testing of the turbine on RDL with an AMP, no opportunistic observations of biological targets had been made. To evaluate the potential algorithms for detection of targets moving through the field of view and the ability to exclude detections associated with the moving rotor in optical and acoustic imaging data streams, we adopted an approach to testing "cooperative targets." While relatively simple in principle, cooperative testing is made more difficult by the fact that the vessel must be in motion and the rotor itself represents a fouling risk for any tethered target. Therefore, after

performing dockside (i.e., not moving) tests using a rubber fish target, we opted to perform our cooperative tests using an inert/biodegradable object. After some research, we identified potatoes as biodegradable object roughly the size of a fish, denser than water, and available at low cost. During cooperative target tests, potatoes were dropped into the water upstream of the vessel and rotor. As they sank the vessel/rotor would cross their path, allowing the VAMP instruments to image them as they vessel moved past. The tests were repeated numerous times to capture images of individual potatoes moving through around and the rotor.

2.2.5 Agate Pass: Opportunistic Target Evaluation

Agate Pass is a tidal channel separating the north end of Bainbridge Island and the Kitsap Peninsula in Puget Sound, Washington. Mixed semidiurnal tides in the region drive strong tidal exchange through this relatively narrow (~250 m) and shallow (~6 m) passage connecting the main basin of Puget Sound to the waters surrounding western Kitsap County (Figure 6). Tidally driven currents in Agate Pass can reach 2.5 m/s during strong spring tides. Agate Pass was selected for testing a tidal turbine mounted to a moored vessel due the combination of strong currents and proximity to the University of Washington in Seattle. Operations associated with the Agate Pass deployment were performed from 15-25 April 2022 with turbine and AMP operations occurring from 16-24 April. During this period, the maximum observed currents were approximately 2.0 m/s, which occurred during the afternoon flood.

Relatively high volumes of vessel traffic and the narrow width of Agate Pass dictated that the turbine be positioned outside of the most constricted areas with highest currents (Harrison et. al. 2023). Consequently, RDL was moored in 8 m of water at the southern end of Agate Pass at 47.7070° N, 122.5705° W (Figure 6). This location offered a combination of moderate currents, shallow water, sandy substrate favorable for anchors, and relative protection from the metocean conditions of Puget Sound's main basin.

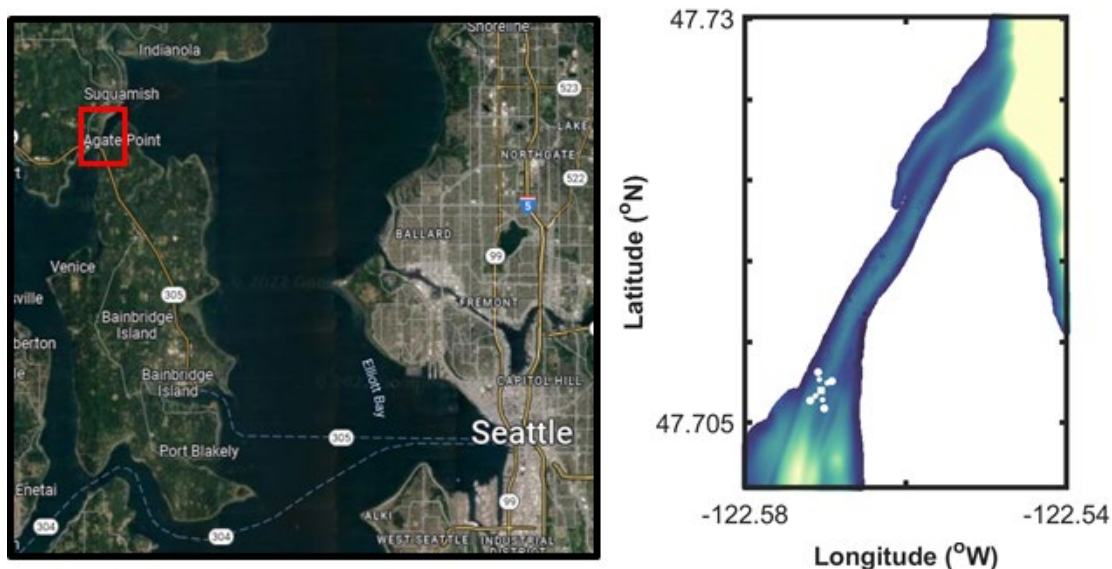


Figure 6: (left) Central Puget Sound region with a red box highlighting Agate Pass. (right) Bathymetry and RDL's mooring layout during the experiment (colorbar limits 0 to 20 m depth).

During these tests, a downward-facing acoustic Doppler current profiler (ADCP, Nortek Signature 1000) was deployed approximately 1 m from the rotor on RDL's gantry. Two-minute running averages of horizontal velocities corresponding to depth bins approximately 1 m below the bottom of the rotor were used as a turbine control system input. Based on the average current speed, the controller regulated the

rotation rate of the turbine to maintain a time-averaged tip-speed ratio (ratio of blade rotational speed to inflow velocity) of 1.8. This tip-speed ratio corresponds to the approximate maximum rotor mechanical conversion efficiency (Figure 3). ADCP measurements revealed minimal vertical shear in the upper water column such that a velocity measurement below the rotor plane approximated the inflow condition, while remaining unaffected by the rotor wake on ebb or flood tide. Figure 7 shows a picture of the power take-off, rotor, and AMP as mounted to RDL in Agate Pass and Figure 8 shows a rendering of the system with the turbine and AMP deployed below the water surface.

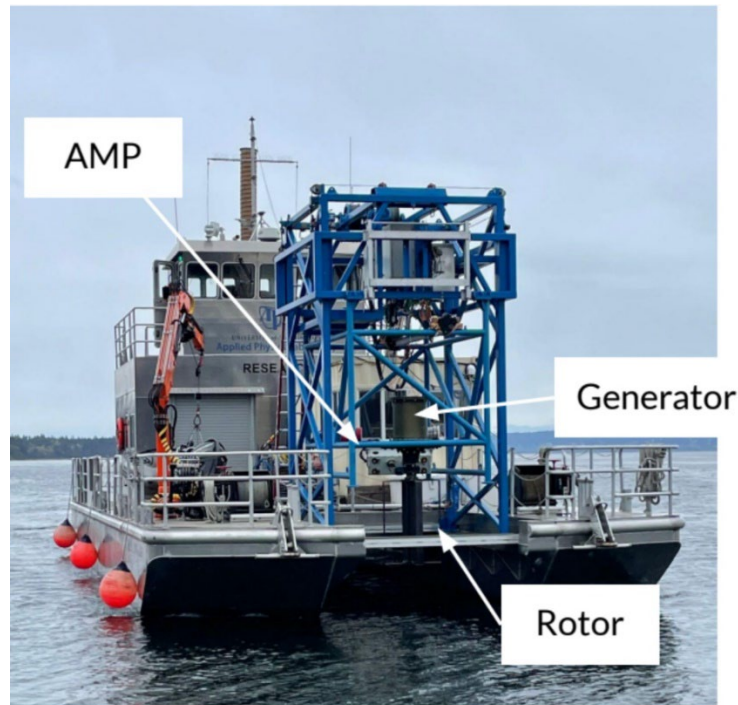


Figure 7: Configuration of rotor, power take-off, and RDL for Agate Pass.

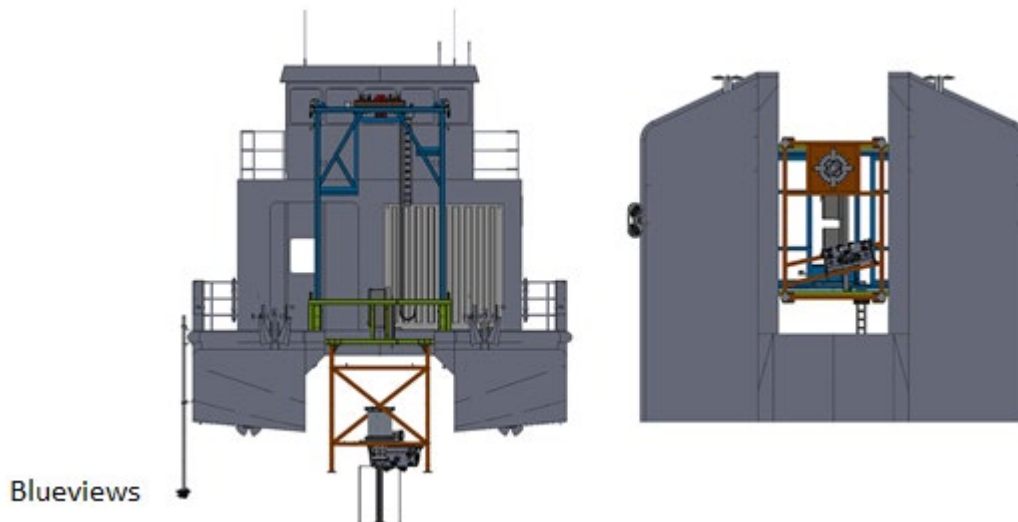


Figure 8: Rendering of the turbine and AMP underwater with the Blueview sonars pole-mounted on the starboard side of the vessel at the depth of the rotor.

During sampling, the turbine programmed to operate when inflow velocities exceeded 0.6 m/s. These are below the units standard cut-in speed (where net power generation begins) of about 1 m/s, meaning that the turbine consumed power to operate. However, this approach was beneficial because the total duration of the experiment was limited, and this increased the total rotor operation time. Because RDL could not be deployed in the area with the strongest currents, the ebb currents were quite weak and generally did not exceed 1 m/s. Using this approach, over 40 hours of data with the rotor spinning were recorded (Figure 9).

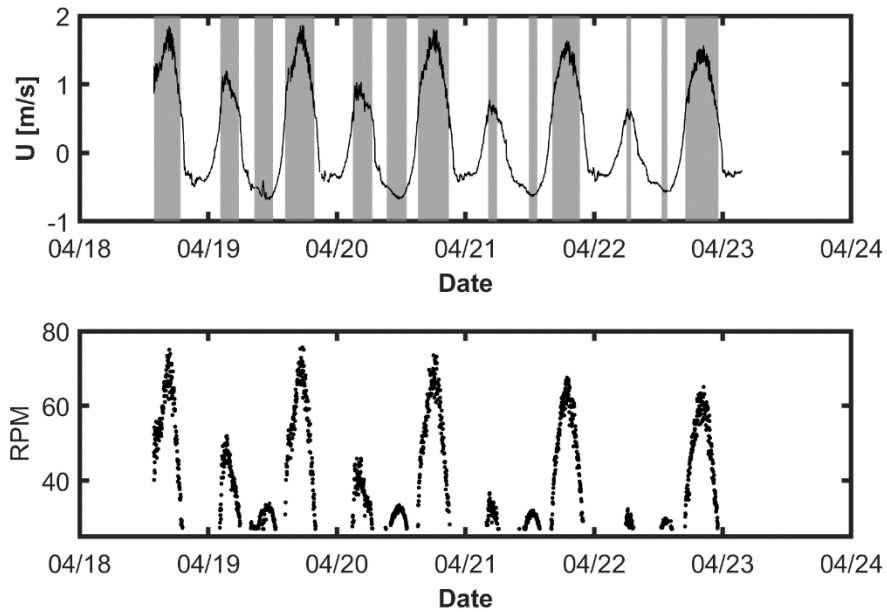


Figure 9: (top) Inflow velocities during the Agate Pass test. Shaded areas show periods during which the rotor was active. (bottom) Rotor speeds through the Agate Pass operations.

The stereo camera pair and imaging sonars were positioned to capture as much of the scene as possible (Figure 10). The optical cameras were located near the rotor and oriented along the principal axis of the flow (i.e., during flood tides the direction of the flow was approximately straight towards the cameras through the rotor). The sonars were pole mounted approximately 5 m away from the rotor and oriented roughly perpendicular to the currents, capturing information upstream and downstream of the rotor.



Figure 10: Optical and sonar images of the turbine during deployment. This display was visible aboard the vessel and used to populate a log of events of interest by the real-time observer.

Throughout the test, the imaging sonars and optical cameras operated with frame rates at or exceeding 20 frames per second. The AMP and turbine data were regularly monitored in real-time by a staff member present on RDL. Poor optical clarity attributed to high volumes of suspended particulate was observed throughout the experiment, which significantly limited the range at which targets could be detected and resulted in optical backscattering when artificial illumination was used. Real-time observations included unidentified suspended plant matter, krill, small unidentified fishes, and high numbers of jellyfish (observed more clearly with artificial illumination). Examples of some of these targets are shown in Figure 11. The small fish were occasionally observed in what appeared as tumbling patterns, but were mostly observed to be moving in controlled patterns around the rotor (e.g., in multiple cases they were observed swimming near the rotor tips in their wake). The krill were generally observed only in a single camera and their size in the images suggests they were quite close to the camera during image acquisition. Therefore, no quantitative statements about their interactions with the rotor can be made. In contrast to these targets, the high abundance and swimming capabilities of jellyfish resulted in many observations of jellyfish passing through and around the rotor, in addition to occasional collisions.

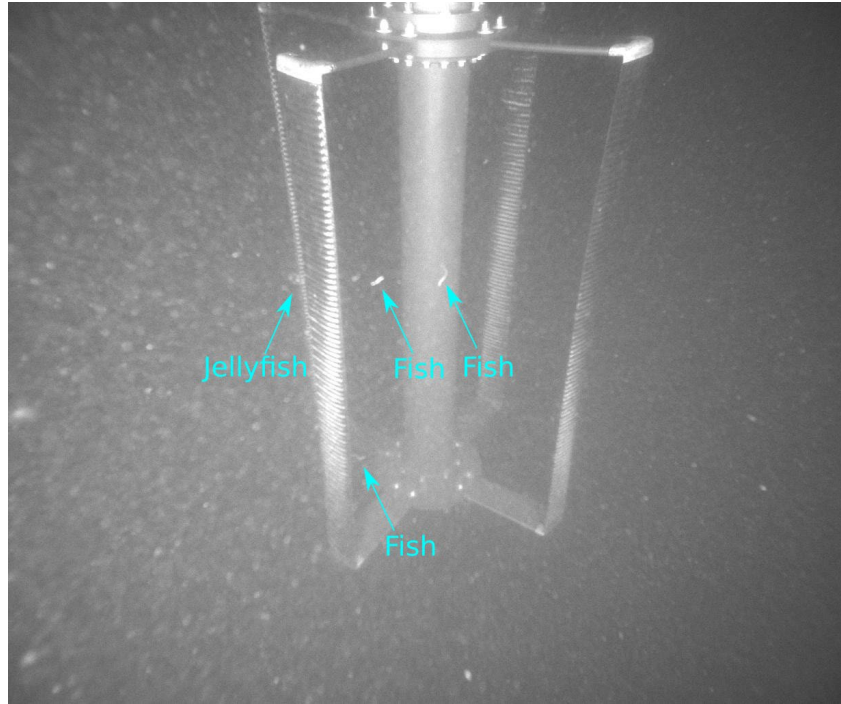


Figure 11: A representative image of collected data at the site containing small fish and a jellyfish. The fish and jellyfish are not well distinguished from the background and the image quality is poor due to high levels of backscattering from suspended particulate the water column.

2.2.6 Optical Data Analysis

Optical analysis focused developing machine learning (ML) models for the automated detection of targets in stereo images and tracking targets through subsequent temporal frames. This information can be used to track the position of the targets in three-dimensional space, relating their position to turbine. While ML methods for the autonomous detection of targets has been demonstrated in a variety of fields, the marine environment can be particularly challenging given the potential for low optical clarity and infrequent targets of interest. Thus, pre-trained models using cached imagery from either standard image datasets (e.g., ImageNet) or previous underwater camera deployments could not yield models of sufficient accuracy for the study. It was therefore necessary to build suitable models based on the data acquired during testing in Agate Pass. This began with an initial, manual annotation of the dataset focused on periods noted by the real-time observer. After this dataset of 8,467 targets was curated, we utilized an ML-in-the-loop approach, where an intermediate low-fidelity ML model (YOLO-v3) was trained to further identify periods of fish passage. However, due to the low accuracy of this intermediate model, a substantial amount of human review was still required in this phase. Human-in-the-loop review is also required to avoid a positive model feedback loop, where a model augmentation continues to reinforce its incorrect predictions. Next, we limited data review to only binary-target classification for fish species. That is, all candidate fish were classified as “fish”, with no further taxonomic discrimination. Substantial numbers of jellyfish were also labeled, but they were not investigated in detail. In total, 22,724 fish were identified and labeled as part of this process. Heads and tails were individually labeled for downstream model development (Figure 12), resulting in 45,448 fish “key points” identified. We note that a “fish” in this regard is a fish observed in an individual image, not a single fish observed over several, successive frames (e.g., one fish which swims through 20 successive frames is considered “20 fish” by this counting methodology).

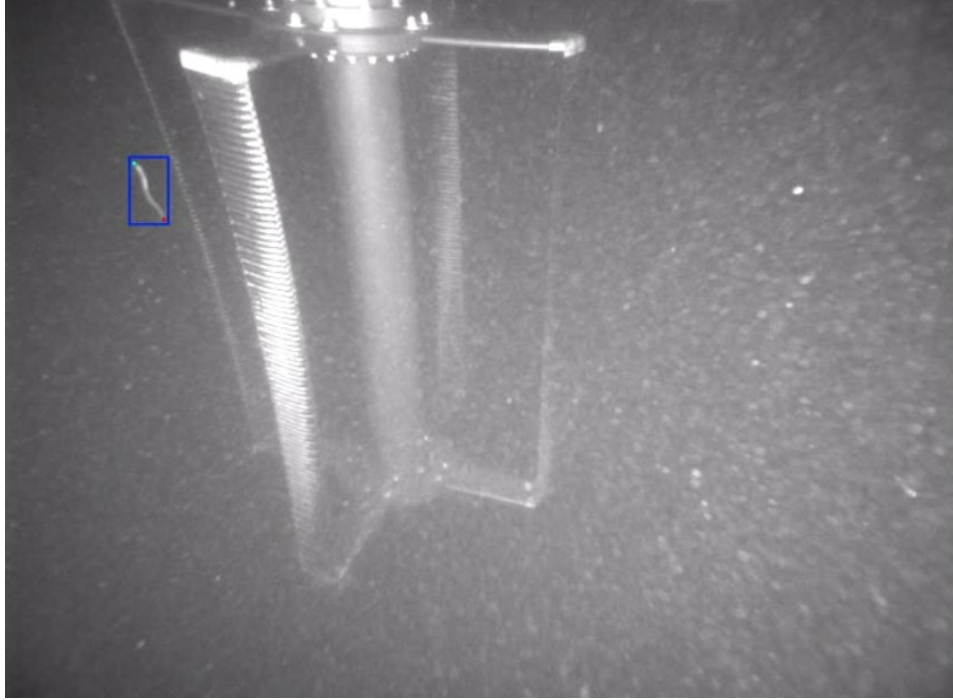


Figure 12: Example image of a target with head (turquoise) and tail (purple) identified. Note that the head and tail look similar, which is problematic for downstream analysis.

Following the data collection and labeling phase, we tested several different model archetypes for target detection. These detection methods were the first step in the full detection-tracking pipeline and consisted of:

1. **Custom bounding box model:** For this model development, the goal output was a bounding box around each potential target in the individual stereo images (regardless of target “pose”) and associated classification.
2. **“Off the shelf” feature point model:** In contrast to the bounding box model, a feature point model is concerned with identifying high-interest regions in images. These points can be defined for any uniquely identifying pixel in the candidate images. Given the relatively low-resolution imagery, number of targets, and lack of distinguishing features among identified targets, we focused solely on identifying the endpoints of the targets (heads and tails) using a common model used for biological behavior analysis: DeepLabCut.
3. **Custom feature point model:** Like the off the shelf model, this approach focuses on the identification of consistent head-tail feature points. We trained the model on site-specific data, specifically pixel-wise head/tail locations. The model was trained on the 45,448 fish key points curated during the data collection phase and outputs head and tail pose predictions for every unique fish instance.

Model performance was evaluated using two common metrics for ML model analysis: precision and recall. Precision is a calculation of the ratio of true positives to total positives:

$$p = \frac{t_p}{t_p + f_p}$$

where p is precision, t_p is the number of true positives and f_p is the number of false positives. Recall (also known as the true positive rate) is the ratio of true positives to total positives in the considered dataset:

$$r = \frac{t_p}{t_p + f_n}$$

where f_n is the number of false negatives, and indicates probability that a target will be detected by the model if it exists in the dataset. The goal of ML model development is generally to simultaneously maximize the value of these two metrics, but, in practice, changes to increase one value often leads to a decrease in the other. For example, increasing the likelihood of true positive detection often increases the false positive detection rate.

Following detection, the images can be triangulated to three-dimensional position to track them across multiple frames. The accuracy of this triangulation was benchmarked against the known distance from the cameras to the turbine. For target tracking, the triangulation method varied depending on whether the bounding box or feature point model was utilized. For bounding boxes, individual fish instances were first corresponded between intra-frame stereo pairs. Bounding box corners (i.e., top-left, bottom-right) between the corresponding instances were then triangulated for 3D pose estimation. For feature points, the correspondence is determined for each feature point before triangulation. In both the bounding box and feature point cases, output data were two 3D points indicating the target's location and endpoints. These points were then tracked as targets moved through the frames to quantify behavior (Task 10.3, Section 2.3.3).

2.3 Results and Discussion

2.3.1 Fish Tracking (Milestone 10.1.1)

The section describes the results tagged fish releases around an AMP in Sequim Bay, WA, where fish locations were tracked by a JSATS array deployed on the seafloor.

Multibeam Sonar Detections

There were seven time windows when a fish detected by the JSATS array was within the BlueView sonar swath. The tagged fish was only clearly visible in the BlueView data in one of these time-windows, which occurred on March 8 at 17:21 and is also present in the Gemini sonar data. Figure 13 shows the acoustic representation of the fish in both multibeam sonar data streams, as well as the co-temporal position reported by the JSATS array. One additional fish may have been observable in data from March 15 which was lost due to an archiving error.

On one other occasion (March 8 at 15:00), a small, faint target moving independently of the tidal currents was detected approximately 4 meters away and a JSATS detection occurred 25 seconds before the AMP detection. While it is likely that this was a tagged fish, this cannot be stated with complete certainty. Finally, on March 29 at 14:58, a bird was observed in the BlueView imagery in close temporal proximity to the JSATS detection. While no fish was visible, it is possible that the bird was diving for the tagged fish.

There were 16 time-windows where a fish detected by the JSATS array was within the Gemini swath. However, beyond the range where the Gemini intersected the water surface (approximately 12 meters range, varying with sensor orientation), it was difficult to separate fish from surface interference or targets on the surface (e.g., floating bird). In several cases, there were relatively high-intensity targets detected at long range concurrently with JSATS detections, but because they were not in the same position, it was not possible to say whether they were a tagged fish. In one particularly interesting case, several targets were observed concurrently, which may have been an interaction between fish and a predator (seal or bird). Bubbles were observed trailing behind the targets, which indicates that the target was likely diving (entrained air). Unambiguously characterizing such rich events is a significant challenge for any non-optical sensor.

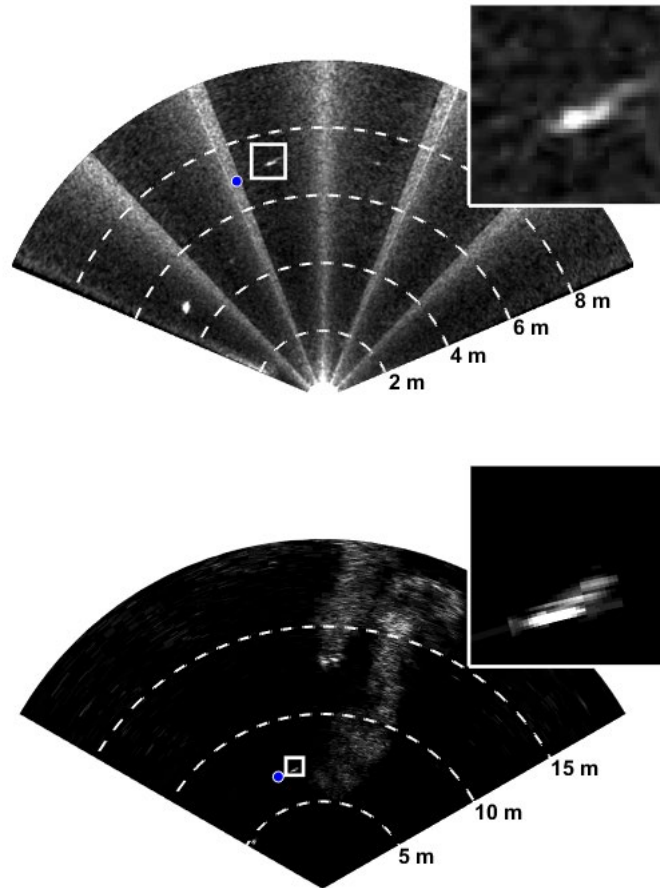


Figure 13: Concurrent Gemini (bottom) and BlueView (top) detection of a tagged fish. The GPS position of the JSATS detection is indicated in blue, and a 1x1 m region around the fish is shown in the insets. The JSATS detection and sonar imagery are offset by 0.8 seconds to show the clearest image. The colormaps of both sonar images have been adjusted to highlight the fish. A hydrophone from the JSATS array is visible around 5 m on the left hand side of both sonar images, and a boat wake is visible in the Gemini image.

Optical Camera Detections

There was only one JSATS detection within the field of view of the optical cameras, which occurred on April 8 at 14:28 (fish tag ID G724A45A5). At this time, a vessel was observed passing over the AMP with suspended instrumentation. This is suspected to be the cage used for release of the fish, and the detected fish may have remained in the cage.

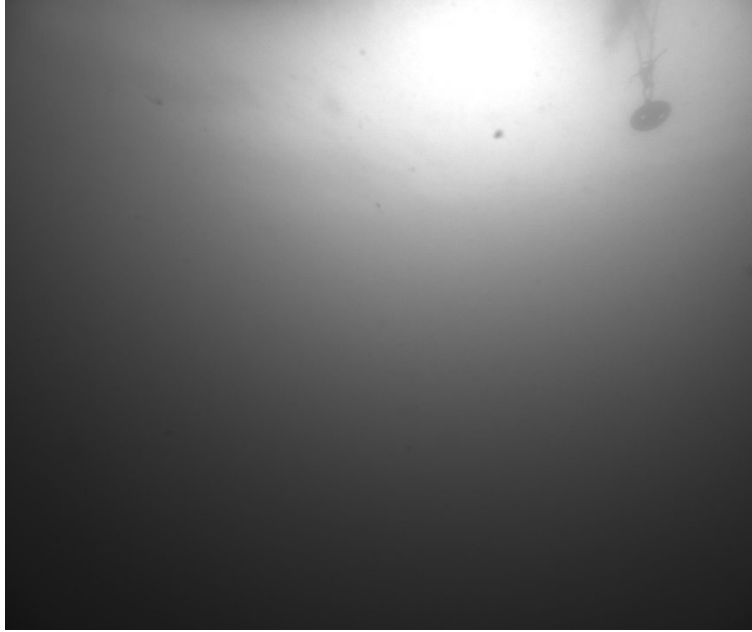


Figure 14: Optical camera data at the time of concurrent detection, believed to show deployment vessel passing overhead.

Inadvertent Data Loss

Data from fish releases on March 15, 2019 were accidentally deleted prior to analysis. This occurred during a batch clean-up of archived data where it was incorrectly assumed that the files had been backed up UW, but this was not the case because of their larger size. Based on JSATS track data, two of the released fish may have been in the view of the multibeam sonars. One of these is a single tag detection, while the other is a series of tag detections split across two events. In the other releases, approximately 1/7 of fish that were potentially in the sonar swath on the basis of JSATS detections were actually visible in the sonar swath. Consequently, we believe that there is a 37% chance that one of the fish would have been observable in the AMP sonar swath. In other words, there is worse than coin toss odds that the lost data contained a second, unambiguous detection.

Study Outcomes

Both multibeam sonars were able to detect the fish within a 10 m range. While there is a small sample size (only clear one detection on both sonars), several inferences can be made. The high-intensity segments between sectors of the BlueView sonar swath (an artifact of the physical layout of the instrument) masked the fish as it swam through those regions. This suggests that tracking will be generally simplified using a sonar without such artifacts (e.g., the Gemini). The fish also produced relatively high-intensity sonar artifacts in other portions of the BlueView image, and no sonar artifacts were observed in the Gemini data as a result of the fish. However, the BlueView sonar has higher resolution, which aids in classification.

Given the low yield of detected fish relative to those released, WPTO made the decision not to move forward with additional tagging and releases during a turbine deployment. However, the subsequent decision to focus analysis on data collected in Agate Pass due to delays in turbine deployment at Sequim rendered that change in scope moot.

2.3.2 Agate Pass Preliminary Data Review (Milestone 10.1.3)

This section describes the results of the initial review of optical camera and sonar data from the Agate Pass deployment.

Optical Cameras

As previously discussed, two biological targets frequently present in the optical data: a small forage fish and jellyfish. The forage fish species was assumed to be Pacific sand lance (*Ammodytes hexapterus*) due to the widespread presence in the region and the shape as observed in optical images. Other fish species were intermittently present (e.g., Figure 15), but not often enough to allow for a model to be trained for their detection. Several examples of hand-labeled targets passing through the field of view are given in Figure 16.

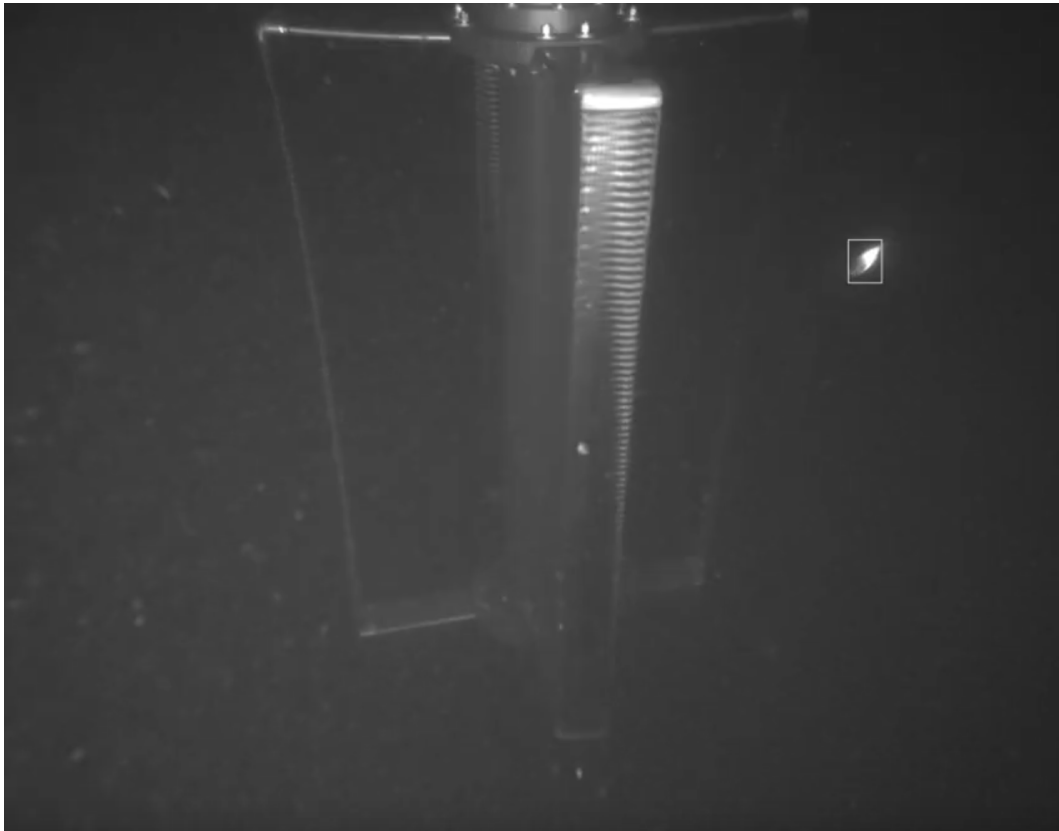


Figure 15: Example of a non-forage fish swimming near the turbine (hand labeled bounding box in white).

As previously discussed (Section 2.2.6), optical data analysis involved a progression of ML-in-the-loop training and detection. The initial step, guided by the real-time observer logs, provided the following information:

1. Large fish were not observed in the data set from either camera. We initially attributed this to the limited sample size, but subsequent review verified that large fish were not present.
2. Most targets were observed at night. We attributed this to the higher contrast provided by the strobes due to the high suspended particulate concentrations.
3. Collision events were seen for jellyfish and debris (e.g., algae), but not for any forage fish.
4. We were generally able to determine if a fish was in front or behind the turbine, but this required both of the stereo images.

Given the relatively small sample size, the initial ML model had a false positive rate of about 35%. Based on these observations, we determined that continuing to study this optical dataset and refine the models was an appropriate step forward.

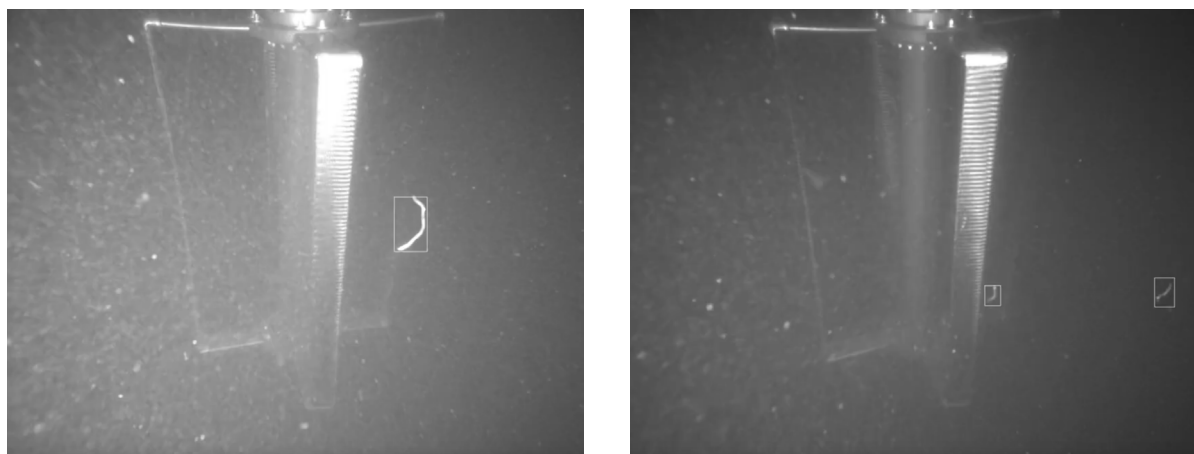


Figure 16: Examples of hand-annotated targets around the turbine

Active Sonar

Using the curated data from the optical cameras, sonar data was manually reviewed for targets. First, a blob detection algorithm was used to find candidate targets, following the methodology demonstrated Cotter and Polagye (2020) during previous AMP deployments. Specifically, candidate targets exceeding a threshold size were tracked through multiple frames using a Kalman filter. Unfortunately, upon review of this data, we found that this approach was unable to detect fish of interest, as the blob detection and tracking method could not reliably distinguish fish from bubbles. Therefore, one minute of data per recorded hour was manually reviewed for targets of interest. This manual review did not identify any larger targets outside the range of the optical cameras, nor could correspondence between optical and acoustic targets be established.

We note that this weakness in the multibeam sonar data set does not necessarily generalize to other settings. First, high concentrations of bubbles were common. These are strong acoustic scatterers and regularly masked other potential targets in the frame. We attributed these bubbles both to discharge from the vessel itself as well as the entrained of bubbles as currents interacted with the vessel. Without the vessel, we believe acoustic image quality would have been substantially improved². Second, most of the acoustic targets observed were relatively small and did not scatter enough energy to be clearly identified in the acoustic images relative to the noise floor. With fewer bubbles, less suspended particulate, or larger acoustic targets, we would generally expect acoustic images to yield informative data.

2.3.3 AMP Target Tracking (Milestone 10.1.4)

Tracking fish across successive frames is critical in understanding fish behavior in the presence of objects. Additionally, the absolute size of fish targets and their location/orientation relative to the turbine rotor can be more robustly estimated using data aggregations over a sequence of measurements instead of relying on noisy, individual snapshots. The ability to track potential collision targets first requires the detection and localization of events in the optical imagery, followed by successive transfer of these detections to a tracking algorithm to produce a full object track over a specific time period.

² This hypothesis was borne out during the subsequent deployment in Sequim Bay, WA (Section 7.1.2)

Automatic Target Detection with Machine Learning

A summary of the ML model performance is given in Table 3. All models used the maximum quantity of training data available. The bounding box model achieved reasonably high recall for fish, but as subsequently discussed, this model has weaknesses for 3D target tracking. The “off the shelf” feature point model (Deep Lab Cut) was unsuccessful, as it required more training data than available to achieve a basic level of functionality. The custom feature point model, while time-consuming to train, was able to detect fish instances, but precision was relatively low. This is attributed to incorrect identification of particulate and debris as fish, as well as improper identification of the heads and tails of the targets. The latter consideration counts against this model in a manner that has no analogue for the bounding box model. That being said, the precision for both models is relatively low, meaning that the trained models produce a significant number of false positive detections requiring human review. This is caused by two factors: (1) relatively low quantities of known, representative fish data for model training and (2) similarities between the appearance of fish and debris at this site. Specifically, even if the rate at which debris is incorrectly identified as fish (false positive) is relatively low, the absolute number of debris present is much higher than the absolute number of fish, leading to a high absolute number of false positives. For these types of targets, none of the models were able to achieve the desired precision and recall of 0.95, though the recall for the bounding box and custom feature point model both approached this goal.

Table 3: Summary of fish detection metrics and the strengths and weaknesses of different detection models.

Model	Precision (<i>p</i>)	Recall (<i>r</i>)	Strengths	Weaknesses
Bounding box	0.78	0.91	<ul style="list-style-type: none"> Good at identifying fish in field of view 	<ul style="list-style-type: none"> Debris often incorrectly categorized as fish 3D track requires establishing correspondence between bounding box on targets identified in each camera
“Deep Lab Cut” feature point model	N/A	N/A	<ul style="list-style-type: none"> Out of the box model (easy to work with) Correspondence between cameras established with feature points (fish heads and tails) 	<ul style="list-style-type: none"> Data requirements too high to effectively train with this data set
Custom feature point model	0.63 ^a	0.94	<ul style="list-style-type: none"> Good at identifying fish in field of view Correspondence between cameras established with feature points (fish heads and tails) 	<ul style="list-style-type: none"> Debris often incorrectly categorized as fish Time-consuming to train Difficult to differentiate heads and tails in still images

^a False positives include cases where a fish is correctly detected, but the head and tail are mislabeled, so this is a relatively conservative description of precisions relative to the bounding box model.

Stereo Target Tracking

The distance from the camera to the turbine was estimated from stereo processing to be 1.19±0.04 m, which compares favorably to the actual distance of 1.15 m. This suggests that the stereo calibration is sufficiently accurate to estimate the 3D pose of fish targets, provided that target correspondence can be established across the pair of camera frames. While the bounding box model has good precision and

recall, the correspondence step is challenging, given that the bounding box dimensions often differ between the two cameras and extracting a common location for tracking within the box requires a set of empirical rules. In contrast, the feature point model performs identification and correspondence as a single step. This is effective at resolving the 3D target and pose, as shown in Figure 17.

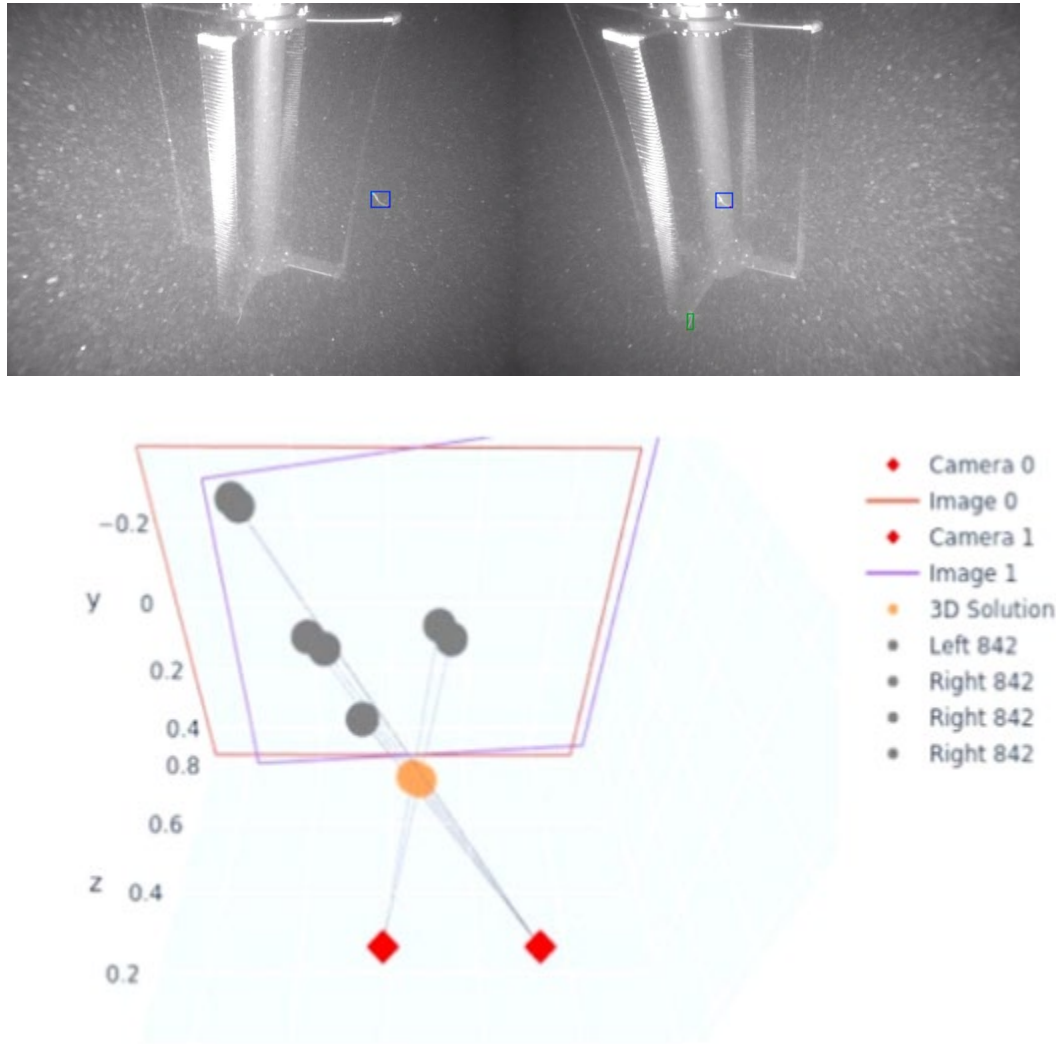


Figure 17: An example of correspondence and 3D triangulation for a single target. The optical images show a target bounding box in blue for both cameras. The bottom panel shows the predicted 3D location of the head and tail key points, which in both cases is estimated to be approximately 0.6 to 0.7m from the left camera. The units on the axes are meters.

However, track fragmentation remains a challenge for targets like these with limited distinguishing features. An example of this is shown in Figure 18. A single, small fish is apparent in all six image frames while the turbine rotates. The feature point model initially classifies it as a target (a), then classifies it as a new target (b-d), and then re-identifies it as the original target (e-f). This misclassification issue occurs independently for each camera, such that fragmentation can vary between images in a notional pair. The overall issue is likely a consequence of the relatively indistinct shape and would be mitigated for larger targets.

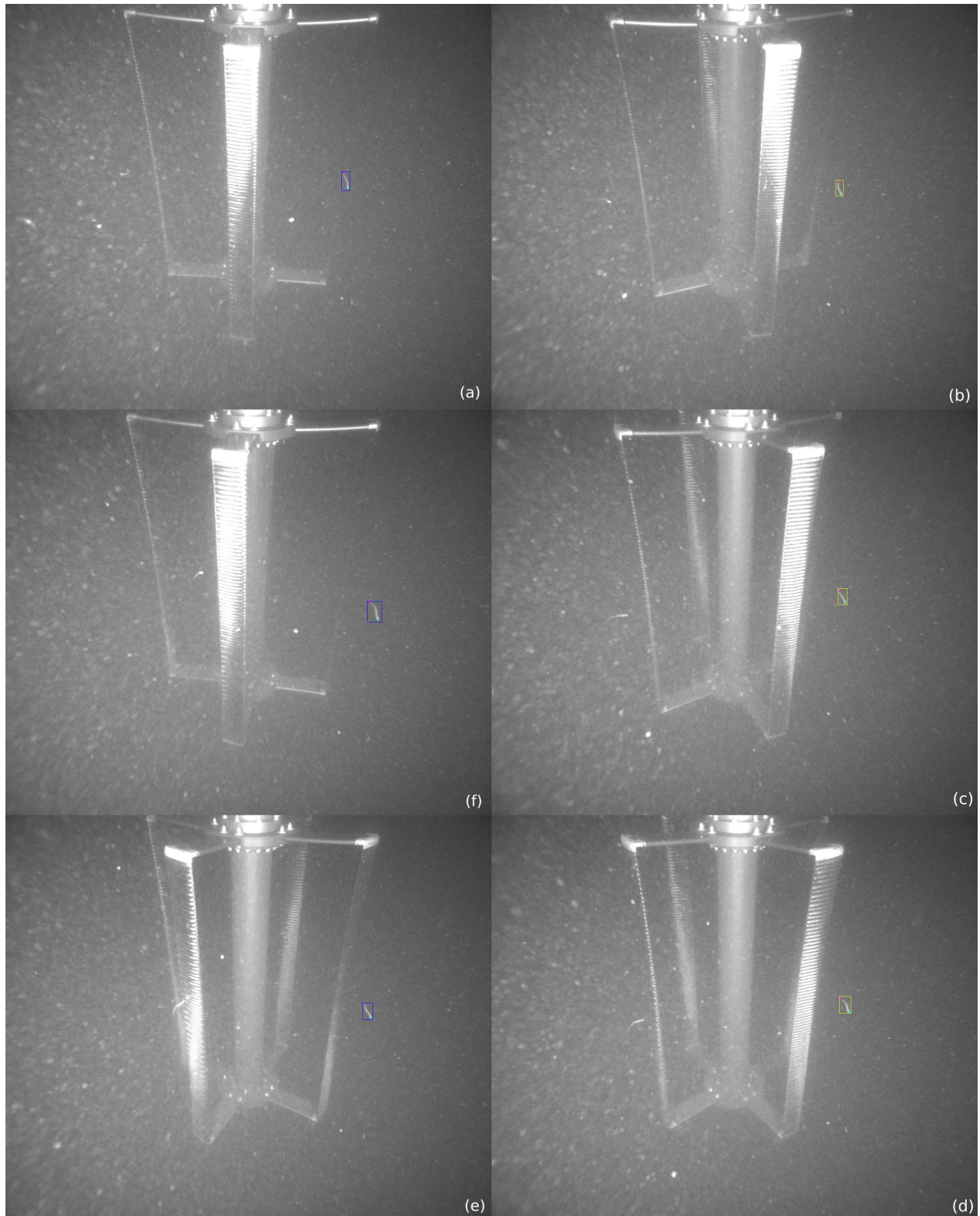


Figure 18: An example of track fragmentation for a single target using the feature point model. The temporal image sequence is shown in the clockwise progression from (a) to (f). Target ID 1 is designated by the blue bounding box and Target ID 2 is designated by yellow bounding box. Head and tail features are designated by the green and red dots, respectively.

2.3.4 Collision Detection with Optical Cameras

To evaluate the general ability of the cameras to resolve collision events with the turbine rotor, we consider four representative cases: cooperative targets in Lake Washington, jellyfish collision at Agate Pass, debris passage through the turbine at Agate Pass, and fish passage through the turbine at Agate Pass.

Figure 19 shows a collision between the rotating turbine and a cooperative target (potato) during the Lake Washington tests. An interesting observation from this testing is that, because of the structure of the flow field around the turbine (Task 10.2, Section 4), even a passive object can have the appearance of changing trajectory to avoid the turbine. This has implications for observations of motive targets around turbines. During the Agate Pass test only two obvious collisions events between the rotor and jellyfish were observed. These obvious events (Figure 21), were characterized by the clear deformation of the body in response to the collision. While it is possible, perhaps likely, that more collisions occurred during test, few of these had similarly concrete evidence. We attribute this uncertainty to multiple factors: (1) the jellyfish observed were generally quite small (on the order of a couple inches diameter or less), (2) the water clarity was generally poor and jellyfish were only readily observed with artificial illumination, and (3) much of the time spent operating with artificial illumination corresponded to flood tides, during which the jellyfish advected by the current were moving towards the cameras from the other side of the rotor making it difficult to image upstream interactions. Unlike marine animals, collisions with plant matter were relatively common (e.g., Figure 22 shows a piece of drifting plant matter being caught on the turbine blade during operation).

Overall, these examples suggest that camera resolution is sufficient to identify collision and passage events. Higher frame rates could improve this, but would come at the cost of reduced resolution, given bandwidth constraints between the cameras and integration hub on the AMP (1 Gbps).

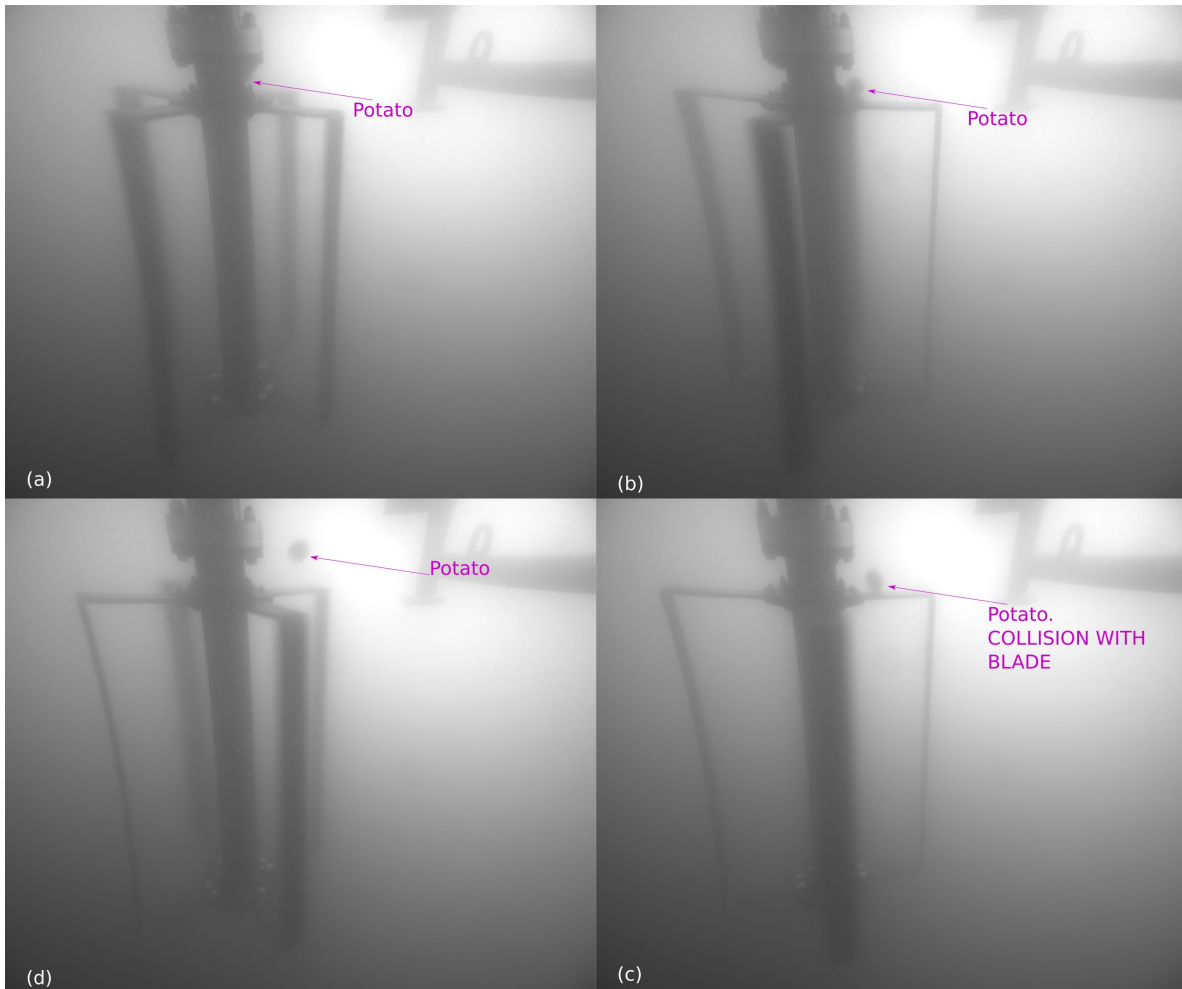


Figure 20: Example potato collision shown in chronological order starting with (a) and moving clockwise to image (d). (a) Potato becomes visible, partially occluded behind the rotor shaft. (b) Potato about to collide with the spinning turbine. (c) Potato collides with the rotor. (d) Potato deflects off blades on a new trajectory.

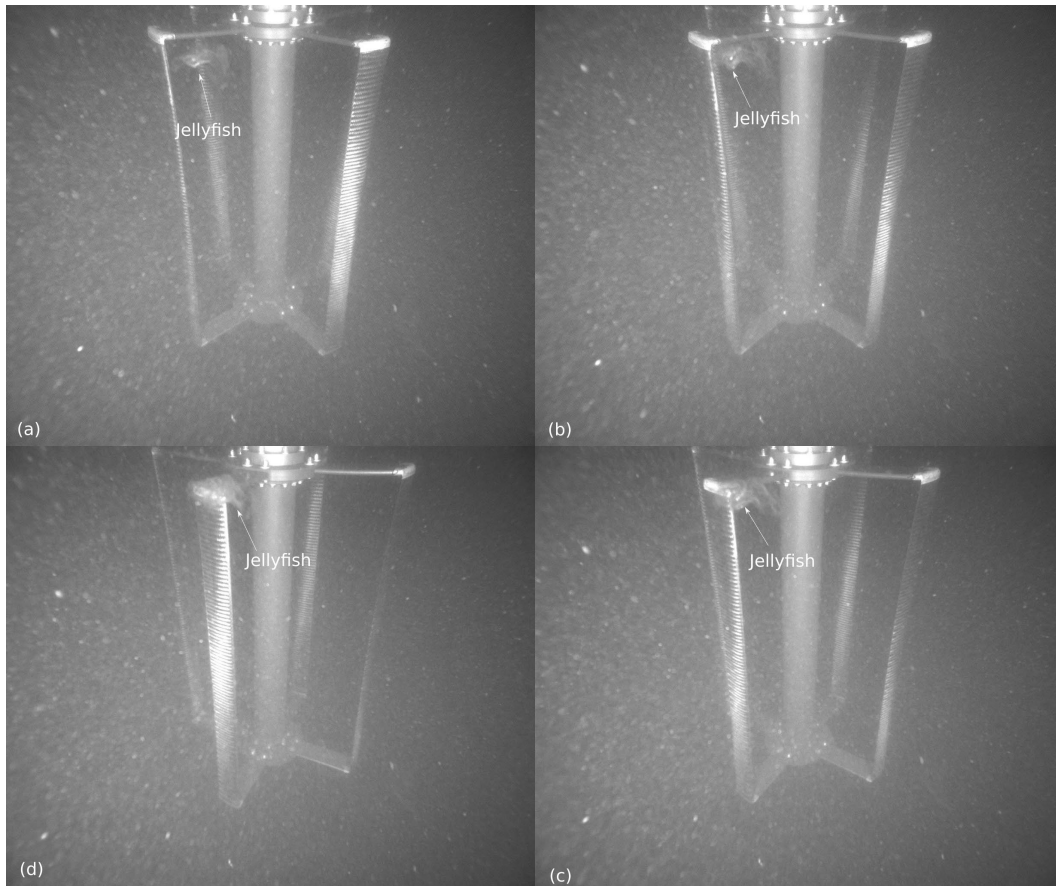


Figure 21: Example of a jellyfish colliding with the front of the turbine blade. This proceeds temporally starting with (a) and proceeding clockwise to (d). Collision occurs between frame (c) and (d).

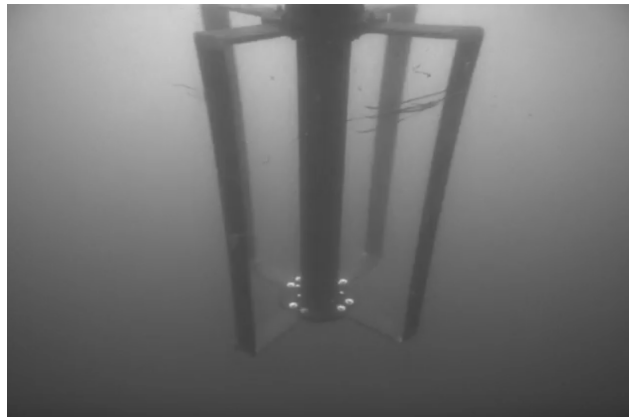


Figure 22: Image of debris caught on the rotor blades.

In the Agate Pass data, there are many instances where fish are visible in the optical data, in front of the turbine on ebb tide, having passed either around the rotors or between the blades. In none of these examples was fish collision observed. Figure 23 includes two examples of fish seen in front of the turbine using the cameras.

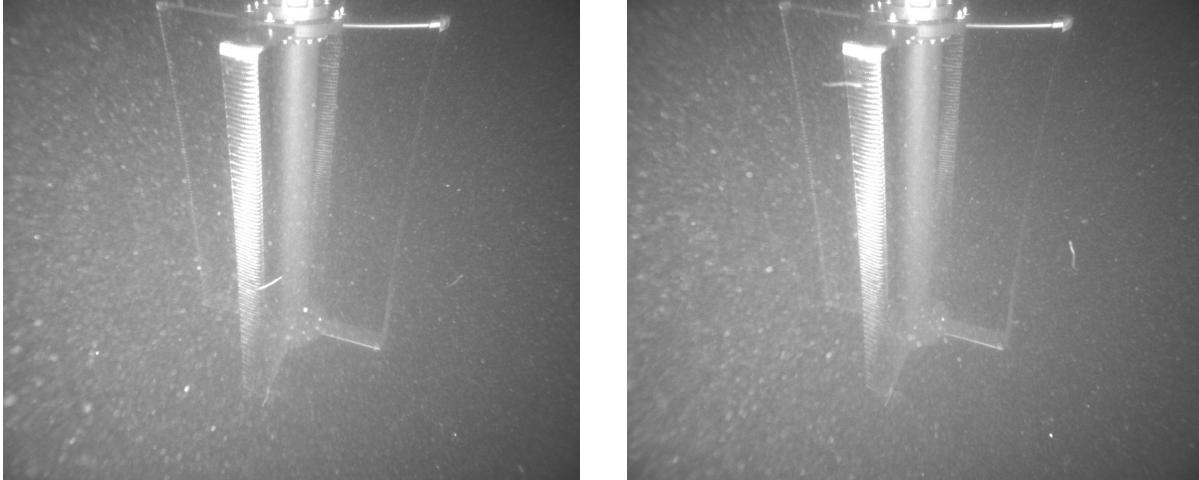


Figure 23: Representative examples of fish in front of the turbine. In both cases, the fish are approaching the cameras and moving in the direction of the currents.

2.3.5 Data Stream Fusion (Milestone 10.1.5)

Due to the lack of biological targets, all notable instances of co-registered targets on the cameras and imaging sonars were debris (typically plant matter). These targets were convenient for evaluating co-registration by the sensors, as it was common for drifting plant matter to become temporarily wrapped around a turbine blade for a number of rotations before breaking away and drifting downstream. One example of co-registered plant matter is shown in Figure 24. Additional lessons learned about data stream fusion are discussed in Section 2.4.

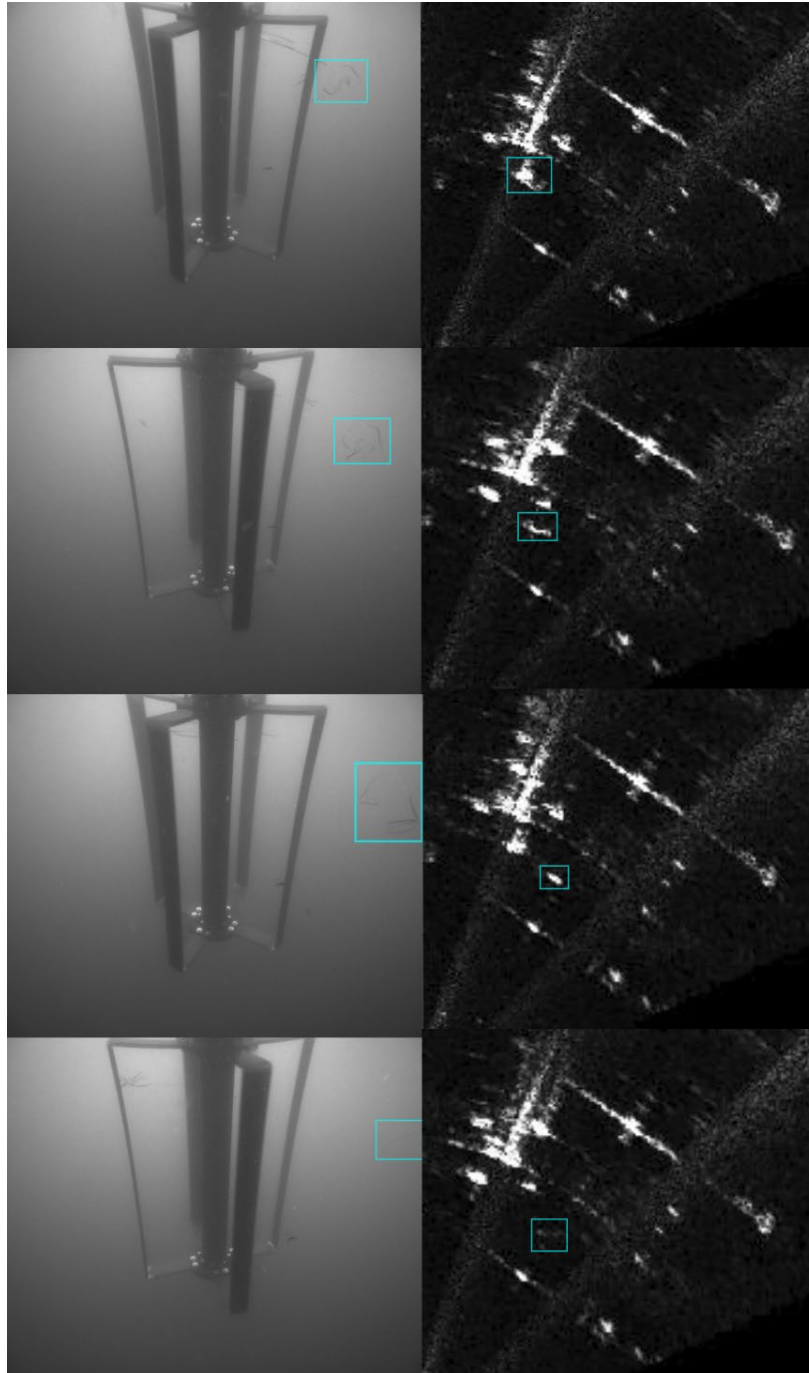


Figure 24: An example of passively drifting plant matter wrapped around the rotor breaking free and drifting downstream. This is clearly captured in the optical images and also apparent in the acoustic images. However, without the optical cameras, it would be difficult to interpret the acoustic images.

2.3.6 Tracking Individual Fish and Aggregations (Milestone 10.1.6)

Identifying Individual Fish in Active Sonar Data

The general feasibility of discriminating between fish and debris using only sonar data remains an important question that we hoped could be addressed with this work. Unfortunately, the measurements gathered in Agate Pass were insufficient to provide clarity on the subject due to a combination of a

limited number of target types and sonar characteristics (i.e., dynamic range, noise floor). In Agate Pass, we observed only small fish – presumed to be Pacific sand lance – and small jellyfish. Lacking gas bladders, both are weak acoustic targets whose scattering may be orders of magnitude less than larger, swimbladder bearing fishes (Thomas et al. 2002; Mutlu 1996), making them much harder to identify acoustically. Their weaker scattering strength is a result of their bodies having fluid-like properties, which is also true of targets like neutrally buoyant plant matter. However, with similar acoustic properties, the size because a critical factor in acoustic detection and in Agate Pass much of the plant matter observed was actually larger than the biological targets.

It is possible that future data sets will reveal that sonar data can be used to discriminate between debris and biological targets of interest. Efforts to do so will likely benefit from broader synthesis of supporting sensing packages. For example, debris should be assumed to be Lagrangian in nature while some biological targets of the scale that can be detected will be less likely to maintain a constant heading when observed over long periods. However, caution is required when interpreting targets at close range to an operating rotor, since the flow disturbance will cause even passive objects to change trajectory. Overall, even if the sonars lack the resolution to specifically resolve targets, behavior itself may provide an additional metric for classifying targets.

We also note that, in the time since this study was initiated, PNNL has conducted significant additional work on identifying fish using active sonar and highlights a number of general challenges, even when sonars with higher resolutions than the ones utilized here are deployed (Staines et al. 2022, Cotter and Staines 2023).

Automatic Detection and Tracking in Optical Data

Based on results to date, the models developed during this work are capable of producing detections of targets of interest in near-collision scenarios, although not without occasionally incorrectly predicting the presence of a relevant target. The most common incorrect predictions are false positives, which occurred primarily during ambient scene changes (i.e., changes in ambient light) or debris passage. False negatives were not as common, but still occurred. Examples of false positive and negative instances are shown in Figure 25. Although imperfect, these or similar models have inherent value in that they can be deployed to assist operators and identify when targets may fall within a set of spatial limits where collision is possible. This would substantially decrease the effort involved in manual review to identify collision events.

Full end-to-end tracking of objects in this dataset ultimately proved unreliable and the autonomous recognition of tracks with enough accuracy to remove human-in-the-loop review was not achieved. Track fragmentation and overall accuracy issues make full tracking particularly challenging in this dataset. We attribute this to three primary issues. First, being deployed on the vessel provided hard constraints on the locations where cameras could be installed. The fact that the fields of view were oriented along the primary axis of the flow and that targets were often occluded by the turbine meant that target could not be easily tracked up and downstream. However, there was insufficient clearance with the gantry to mount the AMP perpendicular to the flow direction and vessel stability would be compromised if moored perpendicular to the currents. Second, water clarity was unexpectedly poor for optical measurements, which is attributed to both bubbles injected by the vessel and the overlap between the deployment and periods of high primary biological productivity. In addition to these factors, most of the targets detected were small and many had poor contrast (e.g., jellyfish), further increasing the challenge of tracking the targets. Full end-to-end tracking and autonomous alerting is still possible, perhaps likely, where different sets of environmental conditions and targets simplify the data. For example, Figure 26,

shows camera data collected during a prior AMP deployment in Sequim Bay, WA where image clarity is substantially higher with the same set of camera hardware.

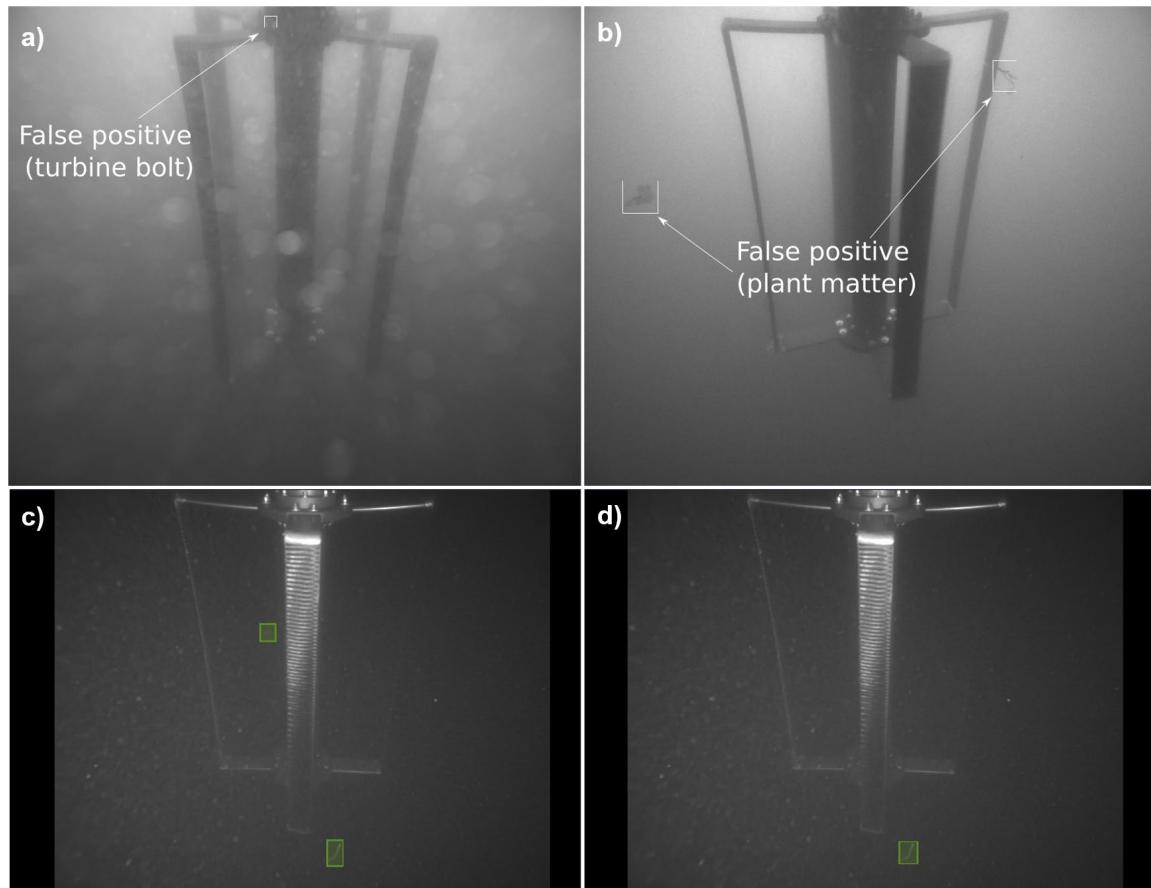


Figure 25: Examples of false positive fish detections for a bolt (a) and drifting plant matter (b) by the YOLO-v3 bounding box method. Example of a false negative detections for (c) hand-labeled detections of two fish and (d) bounding box detection of the same frame showing a single fish.

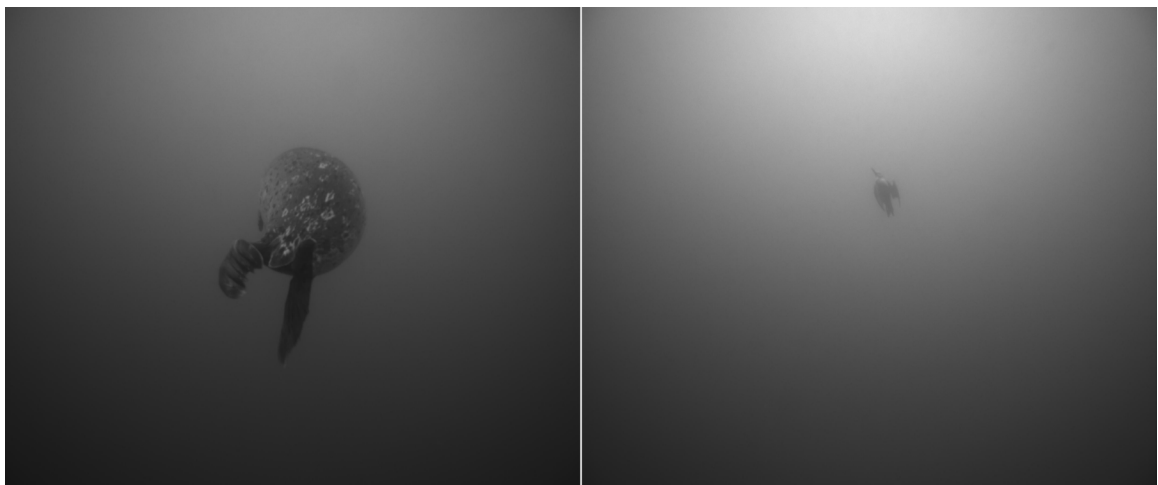


Figure 26: Example data recorded in Sequim Bay, WA near PNNL's Marine and Coastal Research Laboratory. The data, collected in 2019 under clearer optical conditions than observed in Agate Pass, show a seal (left) and diving bird (right).

2.4 Lessons Learned

The choice to perform this study during the vessel-based turbine deployment in Agate Pass was driven primarily by uncertainties associated with permitting of a seabed-based turbine in Sequim Bay (Section 1). At the time the decision to conduct the study in Agate Pass was made, there were no indications of when the relevant authorizations would be received for a Sequim Bay deployment. Therefore, we proceeded to perform the best possible study within the constraints. However, numerous unexpected challenges emerged during the experiments (e.g., low water clarity, limited variety of targets). These impacted our ability to draw some of the intended conclusions from the activities conducted.

Surface-based platforms are not ideal platforms for performing studies related to interactions. While animals may not avoid vessels, they are much larger than the rotors mounted on them and are, themselves, artificial structures that may impact presence, absence, and behavior. In addition, their presence has significant potential to impact data quality. First, vessel structures can entrain bubbles as waves break or flow responds to them. Second, if the vessels have larger generators, seawater is typically used as a coolant. The discharge of this cooling water entrains a significant numbers of bubbles. On RDL, this discharge occurs near the stern, so on ebb tides the turbine was downstream of the discharge point and the bubbles functionally masked most of the acoustic images. Lastly, frames and associated super structure also resulted in significant, and unavoidable, acoustic scattering that impacted acoustic imagery. There may be some circumstances in which surface platforms can be made suitable for such studies (e.g., Staines et al. 2022), but we would recommend exercising caution when planning a similar study in the future.

Environmental conditions also have a significant impact on data quality – particularly for optical cameras. While these challenges are difficult to avoid entirely, if schedules are flexible, some can be mitigated. This includes surveying outside of the peaks in primary productivity (e.g., spring in the northern hemisphere) and periods of the year when large run-off events increase sediment loads (e.g., spring melt, fall storms in the northern hemisphere). These challenges may also be mitigated by a longer study duration such that intermittent environmental factors are unlikely to dominate in the collection period. Longer study durations also help with the fundamental limitation that if any collisions occur, they are likely to be relatively rare events, such that the likelihood of observing one increases with study duration. Unfortunately, this study's timing was set by the neap-spring cycle for anchor deployment and recovery, operator availability to staff the vessel 24/7, and the cost of such personnel-intensive operation. Effectively, operating from a surface vessel had a compounding effect on data quality and utility.

Some fundamental limitations in sampling for collision applications were also observed in this study. Specifically, we found that our pre-existing system AMP configurations had insufficient bandwidth to permit both high-frame rate sampling and high-resolution imagery. We ultimately chose to sacrifice image resolution to obtain higher frame rate data. For reference, with rotor rotation rates on the order of 60 rpm, a rate of 20 frames per second in optical or acoustic data corresponds to an 18 degree change in blade position between images. This corresponds to a translation path of approximately 14 cm, which is appreciable compared to the size of targets of interest. In a recent AMP deployment, changing the network switches allowed a higher bandwidth data, thereby permitting both higher resolution imagery and higher frame rates. Because sonar imagery is less likely to resolve key interactions at small scales, we recommend prioritizing higher frame rate data for optical cameras and allocating network bandwidth for this purpose. We do, however, note that target identification can benefit from high resolution imagery, such that there may be a tension between target classification and observing collision.

We expect that the general framework of this study reflects best practices and that similar approaches adopted under more favorable conditions should yield meaningful outcomes. The risk and impacts of collisions with operating rotors remain uncertain and warrant continued study to reduce regulatory burdens for tidal and river turbine site developers. The methods demonstrated here are likely to perform better not just when environmental conditions are more favorable, but when larger targets are present at sites. Co-registration between acoustic images and optical images in the near-field of rotors will likely be critical in understanding avoidance and attraction behavior to better inform these risks. At the same time, we note that co-registration can be challenging due to mismatches in sensor range and resolution. Specifically, in this study, co-registration between optical, active acoustic, and passive acoustic (JSATS) data streams proved challenging. However, because all three of these data streams can provide unique information about marine animals and their interactions with turbines, employing multi-modal sensing packages is recommended, even when target co-registration is not possible.

3 Task 10.1: Field Data Collection: Acoustic Characterization

3.1 Introduction

Aquatic animals depend on sound for a wide range of activities, including communication, navigation, and foraging. Anthropogenic noise can impact their ability to perform these life-sustaining actions, lead them to alter their behavior, or, in extreme cases, even damage hearing or cause barotrauma (Polagye and Bassett 2020). While marine renewable energy has the potential to reduce negative impacts on the environment by reducing contributions to climate change, it is imperative to consider the full range of possible environmental effects. Therefore, we must be able to accurately measure and predict sound produced by marine energy converters to ensure that noise levels fall within regulatory limits, minimizing harm to marine animals.

Though studies to date suggest that sound produced by prototype tidal turbines are unlikely to impact aquatic animals (Polagye and Bassett 2020), identifying turbine noise *in situ* remains a major challenge. Specifically, relatively low levels of radiated sound from turbines can be difficult to distinguish from ambient noise. In addition, the various moving parts of the turbine—the power electronics, servomotor, and driveline—all have the potential to produce sound. The characteristics of these noises are not well established, making it difficult to predict overall radiated noise.

Our approach employs several measures to differentiate between turbine and ambient noise. First, we use drifting acoustic instruments to collect the data, minimizing flow noise. Second, before measuring the turbine operating in a tidal channel, we collected acoustic data at close range (< 2 m) while it was being motored dockside. This process identifies specific frequency ranges where turbine signals are most likely to present, making them easier to find in environments with a lower signal-to-noise ratio. Third, we use localization to attribute the source of acoustic signals. Though we could not identify any localizable signals from the turbine due to low signal-to-noise ratios, we do localize several other sounds that demonstrate the effectiveness of the methodology and its applicability to future turbine measurements.

3.2 Methods

3.2.1 Turbine and Deployment Site

Agate Pass is a tidal channel separating the north end of Bainbridge Island and the Kitsap Peninsula in Puget Sound, Washington. Mixed semidiurnal tides in the region drive strong tidal exchange through this relatively narrow (~250 m) and shallow (~6 m) passage connecting the main basin of Puget Sound to the waters surrounding western Kitsap County. Tidally driven currents in Agate Pass can reach 2.5 m/s during strong spring tides but only reached 2 m/s during our survey. Agate Pass was selected for testing a tidal turbine mounted to a moored vessel due the combination of strong currents and proximity to the University of Washington in Seattle.

Relatively high volumes of vessel traffic and the narrow width of Agate Pass dictated that the turbine be positioned outside of the most constricted areas with highest currents (Harrison et. al. 2023).

Consequently, R/V Russel David Light (RDL), the vessel on which the tidal turbine was mounted, was moored in 8 m of water at the southern end of Agate Pass at 47.7070° N, 122.5705° W (Figure 27) from 18-23 April 2022. This location offered a combination of moderate currents, shallow water, favorable sandy substrate for anchors, and relative protection from the metocean conditions of Puget Sound's main basin.

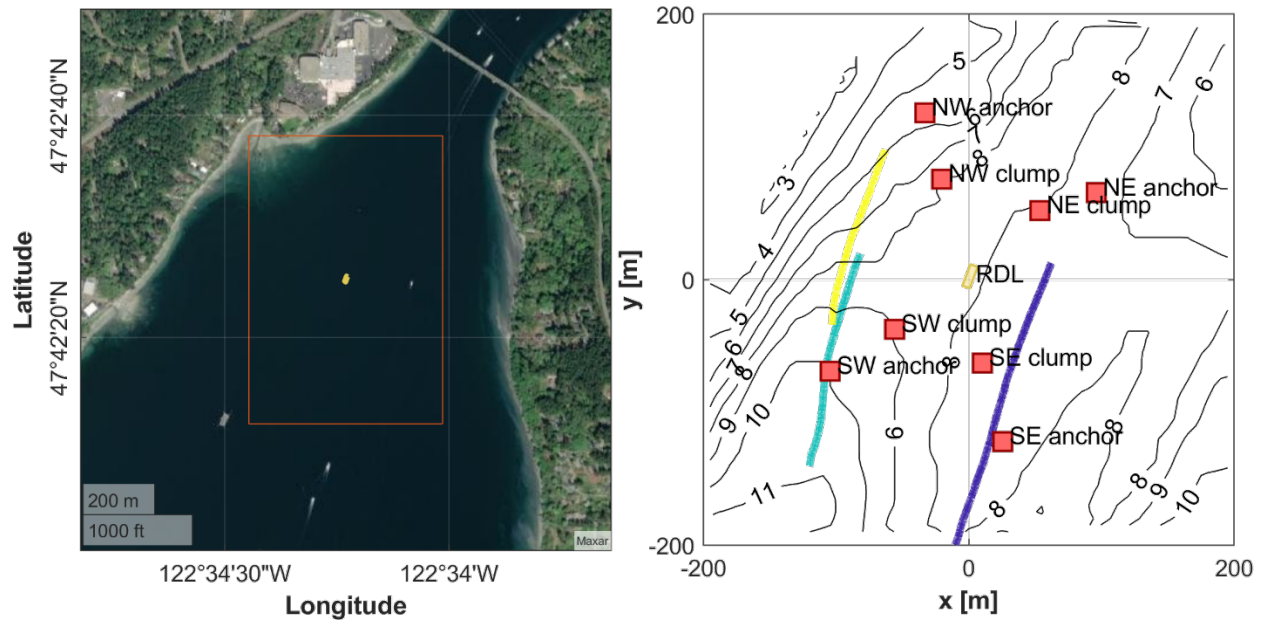


Figure 27: Agate Pass deployment site. (left) Satellite imagery of the southern portion of Agate Pass with RDL's location marked at the center of the box. (right) Overview of site bathymetry, components of the anchor system, location of RDL throughout the deployment, and three representative DAISY tracks.

Acoustic measurements were collected during a relatively strong flood tide on 20 April 2022 between 15:58-17:42 local time. During data collection, there was persistent light rain. Wind-driven waves were small (less than 15 cm), with little to no white capping. A few vessels passed by the deployment site, and measurements were paused while they were within approximately 2 km to minimize their presence in recordings. Vehicle traffic on the Agate Pass Bridge, located approximately 700 meters north of RDL, may have also contributed to the soundscape.

The turbine being characterized was deployed from a gantry aboard RDL, a 20-m long aluminum-hulled catamaran purpose-built for turbine testing. The gantry is located between the hulls near the bow of the vessel, forward of the lab spaces and wheelhouse. During testing, the rotor and generator housing were submerged such that the top of the generator housing and rotor were approximately 0.2 m and 1 m below the surface, respectively. For the duration of measurements, a 30 kW Northern Lights M30C3F generator (1800 rpm) was in operation to provide electrical power for RDL.

RDL was anchored in a four-point moor (Figure 27) with the bow facing roughly NNW into the flood currents. Each leg of the mooring included a 681 kg Danforth anchor with a large surface float. In-line between the anchor and RDL was 59 m of wire rope and chain terminating at a 1055 kg cast-iron clump weight (Figure 28). To support deployment and recovery operations, Viny 12B-3 floats were attached to chains near the anchors and clump weights. As discussed in Section 3.3.3.2, vibrations of the various floats, lines, shackles, and other supporting hardware, particularly the clump weights, produced noise.

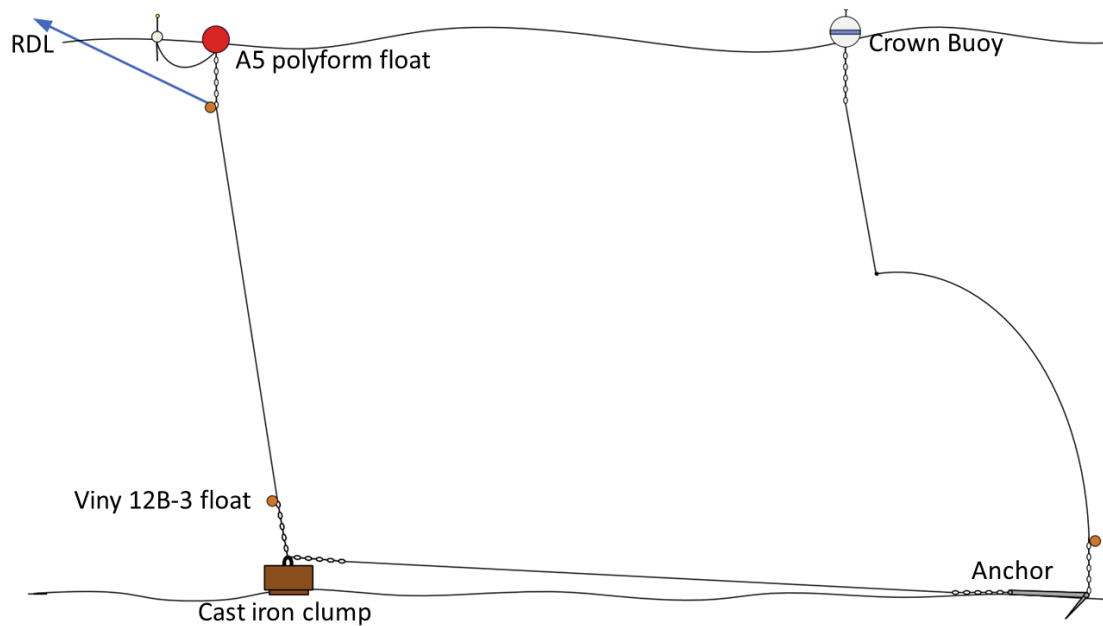


Figure 28: Annotated cartoon (not to scale) of one leg of the RDL mooring. Each mooring leg terminates at an anchor, marked on the surface by a buoy. The anchor is connected to a clump weight by a length of chain, and the clump weight is connected to the vessel by wire rope. At the end of the chain near the clump weight, there are several floats used in deployment and recovery. Note that under tension (while moored) the A5 polyform float is pulled below the surface.

The turbine was a cross-flow variant developed by the University of Washington with a rotor 1.19 m tall and 0.85 m in diameter. The rotor consisted of four straight blades with a blade chord length of 0.098 m. Four struts with cross-sections roughly matching the chord length connected the blades to the drive shaft. The rotor was coupled to a generator using an oil-filled bearing pack and a magnetic coupling. As configured for deployment on RDL, the rotor was cantilevered below the generator housing and bearing pack (Figure 29).

A downward-facing acoustic Doppler current profiler (ADCP, Nortek Signature 1000) was deployed approximately 1 m from the rotor on RDL's gantry. Two-minute running averages of horizontal velocities corresponding to depth bins approximately 1 m below the bottom of the rotor were used as a turbine control system input. Based on the average current speed, the controller regulated the rotation rate of the turbine to maintain a time-averaged tip-speed ratio (ratio of blade rotational speed to inflow velocity) of 1.8. This tip-speed ratio corresponds to the approximate maximum rotor mechanical conversion efficiency. ADCP measurements revealed minimal vertical shear in the upper water column such that a velocity measurement below the rotor plane approximated the inflow condition, while remaining unaffected by the rotor wake on ebb or flood tide.

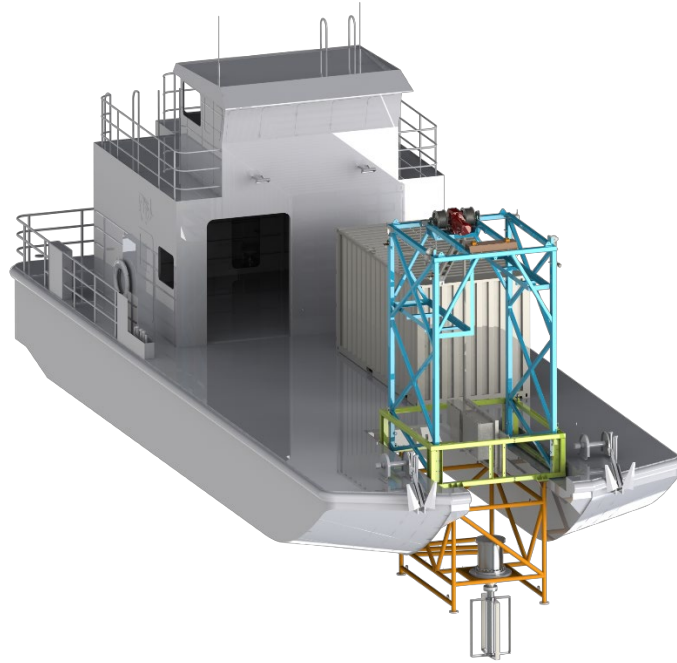


Figure 29: Model of RDL with the turbine. The turbine, suspended off the bow of the vessel, has a height of 1.19 m and a diameter of 0.85 m. The center of the rotor is ~2.06 m below the water surface.

3.2.2 Field Data Collection

To measure underwater noise, we used three Drifting Acoustic Instrumentation SYstems (DAISYs), the minimum number of receivers required to localize sound sources. Each DAISY includes a surface package, an underwater package, and a tether connecting the two (Figure 30). The surface package contains a GPS, compact meteorological station, inertial measurement unit, and data logger. Below the surface, coupled to the surface expressed by a 1 m rubber cord, is the noise measurement package consisting of a hydrophone (HTI 99-UHF), pressure sensor, and custom data acquisition system for logging the hydrophone voltage, pressure, and inertial measurement unit data. Each unit was also deployed with a Garmin Astro dog collar as a backup GPS to help locate the DAISY after deployment. DAISYs are designed to minimize the unwanted (non-acoustic) noise often observed in measurements in highly energetic environments (e.g., the hydrophone is surrounded by a flow shield that minimizes relative velocity during drifts).

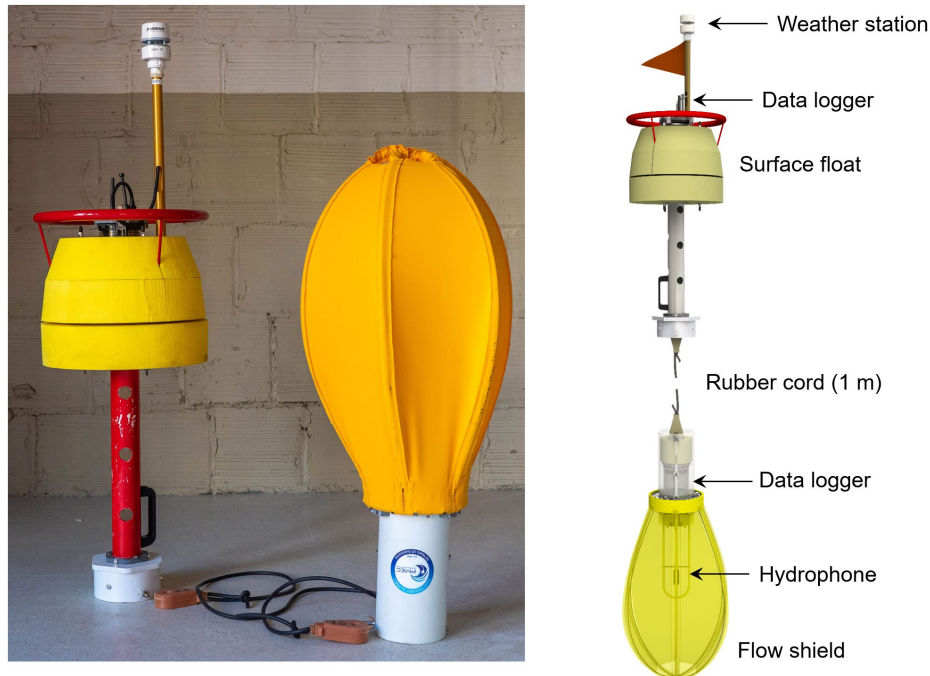


Figure 30: (left) Drifting Acoustic Instrumentation System (DAISY) optimized for tidal currents. (right) Annotated system schematic. The surface package includes a weather station, data logger with integrated GPS, and surface float. Connected to the upper portion by a 1 m rubber cord, the submerged package includes a data logger, hydrophone, pressure sensor, and flow shield.

The DAISYs were deployed from R/V Sounder. While deploying DAISYs, R/V Sounder drifted with the currents to minimize relative velocity and, following release, moved to a standoff distance and shut down all vessel systems to avoid contaminating the acoustic measurements. DAISYs were released upstream of RDL (to the north during the flood tide), drifted past RDL and the turbine, and were then recovered once all units had passed out of the survey area. Because of the risk of mooring entanglement, the DAISY drifts had to maintain a minimum standoff distances on the order of 50 m from RDL. A set of representative DAISY trajectories is shown on Figure 27.

To localize sounds originating from RDL and the turbine—and to investigate changes in radiated noise with inflow velocities and operating conditions—five drifts were conducted during the flood tide. During each drift, two DAISYs were deployed to pass RDL on the port side (weaker currents), and one was deployed on the starboard side. For each drift, means and standard deviations of DAISY speed over ground, wind speed measurement by one unit's meteorological station, and hydrophone depths were calculated from track metadata (Table 4).

Table 4: Track metadata for DAISYs deployed around *R/V Russell Davis Light* in Agate Pass

Localization Drift	DAISY No.	Speed over Ground [m/s]	Wind Speed [m/s]	Hydrophone Depth [m]
A	1	1.20 ± 0.07	0.9 ± 0.5	2.38 ± 0.02
	2	0.21 ± 0.07	-	2.38 ± 0.01
	3	0.70 ± 0.12	-	2.34 ± 0.02
B	1	0.69 ± 0.05	0.4 ± 0.2	2.38 ± 0.01
	2	1.30 ± 0.08	-	2.15 ± 0.01
	3	0.6 ± 0.16	-	2.35 ± 0.01
C	1	1.4 ± 0.14	1.2 ± 0.5	2.38 ± 0.01
	2	0.86 ± 0.08	-	2.37 ± 0.01
	3	0.72 ± 0.02	-	2.35 ± 0.01
D	1	0.72 ± 0.08	1.6 ± 0.6	2.38 ± 0.01
	2	1.00 ± 0.07	-	2.38 ± 0.01
	3	1.5 ± 0.09	-	2.35 ± 0.01
E	1	1.6 ± 0.12	0.9 ± 0.5	2.38 ± 0.02
	2	1.10 ± 0.10	-	2.37 ± 0.02
	3	0.99 ± 0.10	-	2.35 ± 0.01

To benchmark the effectiveness of the DAISY localization protocol, we employed a “cooperative” source with known timing and origin. Several times during localization drifts, one of the co-authors aboard RDL hit the deck with a steel pipe to create an impulsive sound. Although the noise had to propagate through the vessel and into the water, thus creating ambiguity in the source location, this approach provides some spatial constraints on the approximate source location (i.e., successful localization should fall within RDL’s footprint).

3.2.3 Dockside Test

Prior to testing in Agate Pass, we took acoustic measurements of the turbine in a dockside setting to predict the types and intensities of sound that might be detectable in the field. Tests were conducted on 23 March 2022 while RDL was at the University of Washington Applied Physics Laboratory dock in Portage Bay (Seattle, WA). The turbine was submerged to the same depth as in Agate Pass and motored by the generator from 60 to 110 rpm in increments of 5 rpm, a broader range of conditions than would later be experienced in Agate Pass. Speed, torque, and power data from the turbine system were recorded throughout the test, including when the power electronics and generator were energized and de-energized.

During these tests, a hydrophone (OceanSonics icListen HF) was positioned at a depth of 3 m and 2.5 m away from the axis of rotation. While vessel traffic was limited throughout the test, the dock is located directly under a bridge with heavy vehicle traffic. Prior measurements indicated relatively high levels of

ambient noise at the dock due to this traffic and other anthropogenic noise sources along the highly developed urban shoreline.

3.2.4 Data Analysis

Acoustic Data Processing

Hydrophone time series data were used to calculate multiple acoustic data products. First, raw time series data were split into 1-second windows ($N = 512,000$ points) with 50% overlap. These were tapered using a Hann window and processed using frequency-dependent calibrations to generate pressure spectral densities (PSD) with 1 Hz resolution. To reduce data volumes, variable band merging was used to calculate hybrid milli-decade levels (Martin et al. 2021a, 2021b), which have 1 Hz resolution below 435 Hz and lower resolution corresponding to 1/1000th of a decade (order of magnitude increase) at higher frequencies.

Extrapolation of Dockside Data to Field Site

Dockside sound generated while motoring the turbine power take-off was extrapolated to measurements at Agate Pass to inform comparisons between potential radiated noise from the operating rotor and ambient noise. Assuming that the power-take off produces similar radiated noise during power generation and motored operation, dockside acoustic data are used to predict received levels at Agate Pass using a hybrid spherical/cylindrical spreading model with negligible absorption. The PSD of turbine noise expected to be received by a DAISY is estimated as $PSD_{DAISY} = PSD_{dockside} - 15\log_{10}\left(\frac{r_{DAISY}}{r_{dockside}}\right)$, where subscripts denote location and r is the distance between the turbine and DAISY.

Localization

The goal of localization is to estimate the origination location of a signal to aid in source attribution. Localization requires knowledge of the location and geometry of the receiver array, as well as the ability to temporally resolve signals of interest. To perform a two-dimensional localization, at least three receivers are required. Here, we implement a time-difference-of-arrival (TDOA) technique on signals of interest identified in manual review. For example, Figure 31 shows received levels from the cooperative source on the three DAISYs in the drift, as well as the time and frequency ranges of interest. In this approach, the locations of the receivers—the three DAISYs—and the differences in the arrival time of the signal at each are used to estimate the source location.

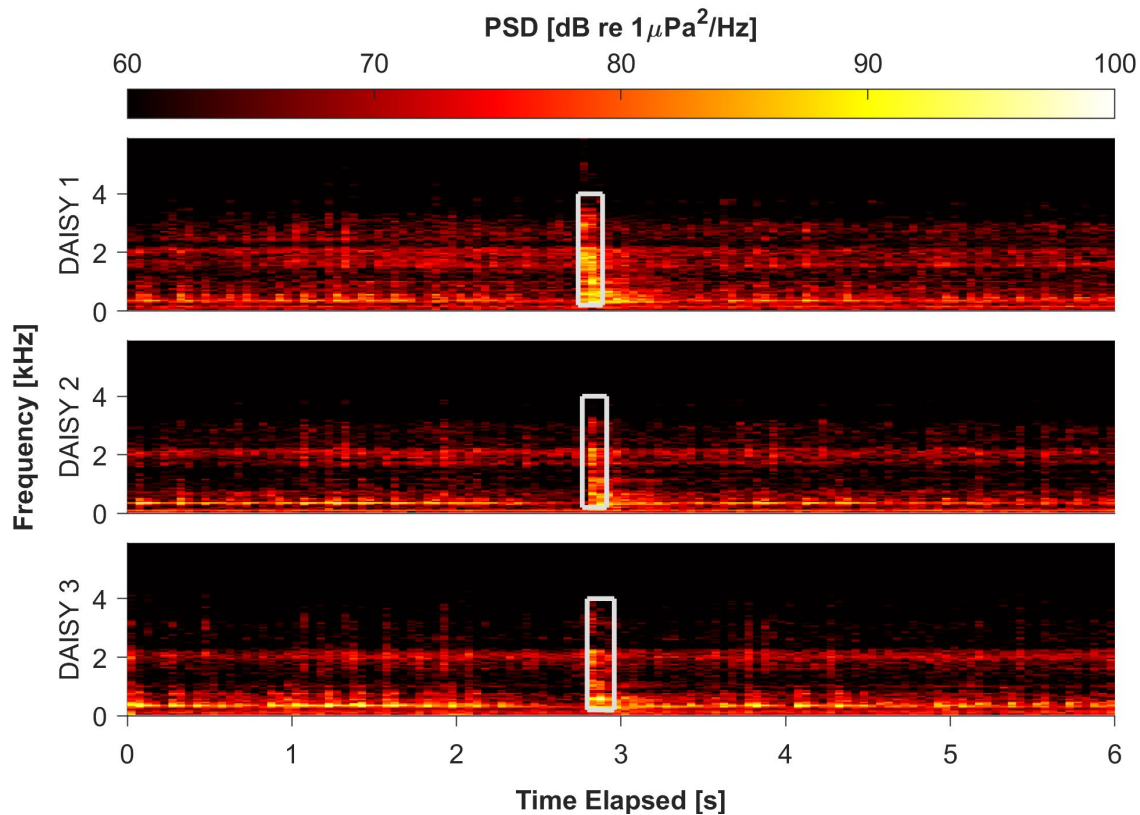


Figure 31: Spectrograms showing simultaneous received levels from the three DAISYs during a portion of Localization Drift 3. A cooperative strike is visible as an impulsive, broadband signals at ~3 s. White boxes denote the frequency and time ranges chosen for the strike to localize its source.

The first step in localization is to identify the arrival time and frequency ranges corresponding to signals of interest in each of the co-temporal DAISY tracks. For each event, we detrend the hydrophone voltage and apply a bandpass filter (typically ~200 – 4000 Hz) to suppress noise outside of the band of interest (Figure 32). In each event time series, the index of the maximum absolute value of the cross-correlation is taken as the reference time of arrival. By using the same portions of the time series on all units, the indices associated with the peak in the cross-correlation correspond to the time delay between the signals with added uncertainty introduced by complex propagation (multipath arrivals) and ambient noise.

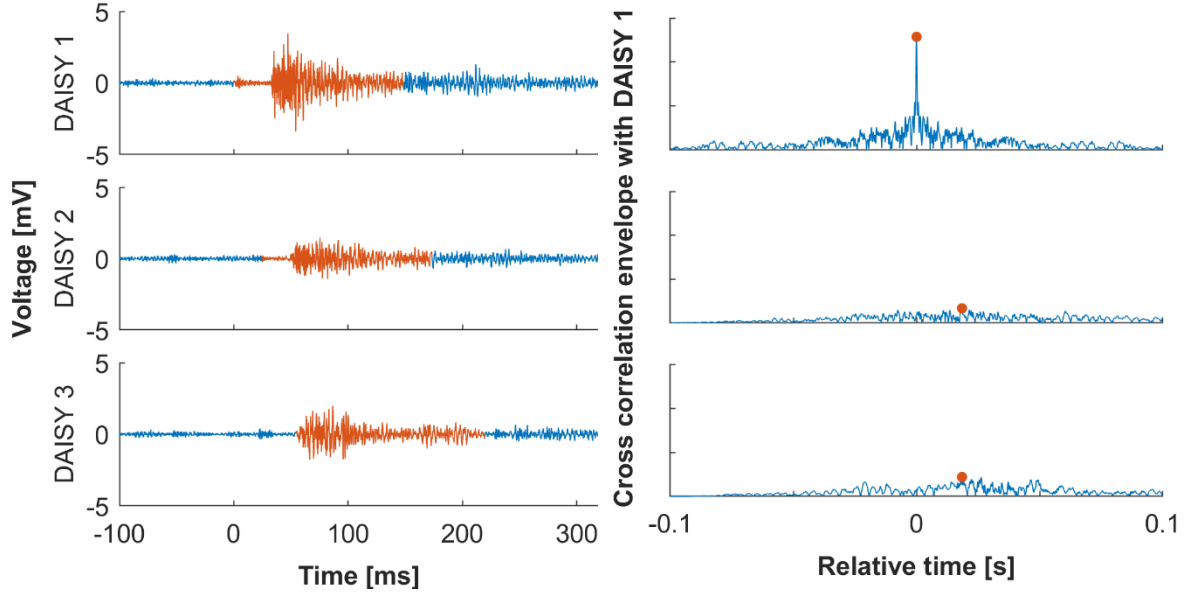


Figure 32: Intermediate localization results for a cooperative strike in drift C. (left) Hydrophone voltage around the strike after it has been de-meant and bandpass filtered to the frequency range of the strike sound (200-4000 Hz). The orange portion denotes the duration of the signal that is considered part of the event. (right) Auto-correlation of DAISY 1's signal and its cross-correlations with the other two DAISYs. The blue line is the envelope of the value of the cross-correlation, and the orange dot marks the point with the highest value. The relative time of this point is considered the time of arrival of the strike.

With these arrival times, we apply a TDOA localization method (Sayed et al. 2005, Guido 2014) to estimate the source location. Sound speed profiles show that the water column was well mixed throughout the measurement period, with a speed of sound of approximately 1480 m/s at DAISY depth. We can estimate the difference in the distances between the source and the i^{th} DAISY and the source and the j^{th} DAISY as

$$r_i - r_j = (t_i - t_j)c, \quad (\text{Eq. 1})$$

where r is the distance from the source to the subscripted DAISY, t is the reference time for the event, and c is the speed of sound in water (assumed constant for all DAISYs).

Using the difference in distance to the source for each pair of DAISYs, the source position can be calculated as a function of the distance from the closest DAISY (i.e., the first DAISY to receive the signal) to the source. This DAISY becomes the reference ("receiver 1") for the event analysis and, with three receivers, the source position as a function of the distance to the reference is given as

$$\begin{bmatrix} x_s \\ y_s \end{bmatrix} = \begin{bmatrix} x_2 & x_3 \\ y_2 & y_3 \end{bmatrix}^{-1} \left(r_1 c \begin{bmatrix} t_1 - t_2 \\ t_1 - t_3 \end{bmatrix} + \frac{1}{2} \begin{bmatrix} x_2^2 + y_2^2 - c^2(t_2 - t_1)^2 \\ x_3^2 + y_3^2 - c^2(t_3 - t_1)^2 \end{bmatrix} \right), \quad (\text{Eq. 2})$$

where x and y are the easting and northing positions. For the DAISYs, position is relatively well constrained by their surface expression GPS (accuracy of ± 2 m). Finally, substitution of this intermediate result—the source coordinates in terms of r_1 —into the geometric definition of r_1 ,

$$r_1^2 = (x_1 - x_s)^2 + (y_1 - y_s)^2, \quad (\text{Eq. 3})$$

yields a second-order polynomial. The largest real root of this polynomial is taken as r_1 and, from this, the location of the source can be identified using (Eq. 2).

3.3 Results

3.3.1 Dockside Test

Three notable features are apparent in measurements from dockside testing (Figure 33). First, when the system is powered and rotating, there is a notable tone at 8 kHz, which we attribute to the power electronics due to the relatively high frequency and the frequency invariance with rotation rate. Second, when the motor is powered on, a tone at approximately 4 kHz is present regardless of the rotor's rotation. The observed noise in this band varies as a function of rotation rate with broader spread between observed tones in the 3.9-4.1 kHz band as the rotation rate increases. Lastly, there are multiple tones generated in the 100 to 400 Hz range that are dependent on the rotation rate. The frequency of the highest intensity tone is strongly correlated with rotation rate (Figure 34a). In contrast, the intensity of the tone is not well correlated with rotation rate or power input to the rotor (Figure 34b).

3.3.2 Field Measurements

Five total drifts were conducted, but here, we focus on a single track, which had the highest signal-to-noise ratio and is therefore the most likely to reveal noise from the operating turbine. Measurements from Agate Pass (Figure 35) suggest that there are three main differences between the field measurements and dockside testing. First, the soundscape in Agate Pass during turbine operation (Figure 35) differs from the dockside tests (Figure 33), with higher levels of ambient noise over most frequencies. While somewhat surprising given the noisy environment of dockside testing, we attribute this, in part, to noise produced by RDL itself. Second, turbine operation also differs, with the rotor being driven by the currents (experiencing a thrust load absent in the dockside testing) and with rotation rates varying with inflow conditions. Third, the Agate Pass measurements were taken at a greater distance (Figure 35e). Due to these differences, over short periods of time (e.g., minutes), signals measured from the turbine in Agate Pass would not be expected to vary to the same extent nor be as prominent as those from dockside testing. However, the anticipated radiated noise signals from the turbine were not observed in Agate Pass. It is unclear whether this is directly attributed to masking by ambient noise or to differences in the radiated noise from the turbine under load. The 8 kHz tone from the servomotor was present, but only exceeded ambient noise at the beginning of the drift track (Figure 35b), and there was no discernible servomotor tone at 4 kHz (Figure 35c). At frequencies below 400 Hz, there are multiple signals present, including many narrowband tones with constant frequency. Since the rotor rotation rate was nearly constant, one might presume that these are attributable to the turbine rotor. However, at the predicted frequency for the driveline, only a relatively low intensity tone (170-175 Hz) during the initial part of the drift, was observed (Figure 36).

In summary, though the dockside test provides useful information for analysis of data collected in Agate Pass, the conditions—and resulting acoustics—at these two sites are disparate. The absence of anticipated sounds in the Agate Pass data could be attributed to two factors. First, the turbine could be producing a different sound in Agate Pass than during dockside testing because of the different operating mode (power generation under thrust versus motored, respectively). However, we believe that a second factor dominates. Namely, that the same signals are produced by the turbine, but the higher ambient noise in Agate Pass and lower received levels reduce the signal-to-noise ratios and mask the turbine signal at the measurement distance. Extrapolation from the most intense signal in the driveline noise range of the dockside data (Figure 34a) suggests that the inflow velocity during the drift shown in Figure 35 and Figure 36 would result in driveline noise at a peak of approximately 109 dB re $1\mu\text{Pa}^2/\text{Hz}$ at a range of approximately 2 m in the Agate Pass measurements. During this drift, measured ambient noise around the peak predicted frequencies (170-175 Hz) is approximately 65 dB re $1\mu\text{Pa}^2/\text{Hz}$ (Figure

35d). Thus, based on transmission losses and motor/generator assumptions, one might expect to observe rotor noise to a range of approximately 850 m without accounting for signal-to-noise ratios. The DAISY stayed within this range (Figure 35e) and therefore should have measured rotor noise well above the ambient noise threshold for the entirety of the drift. However, there are only marginal indications of this sound at the beginning of the track (Figure 36), and they never exceed 80 dB re

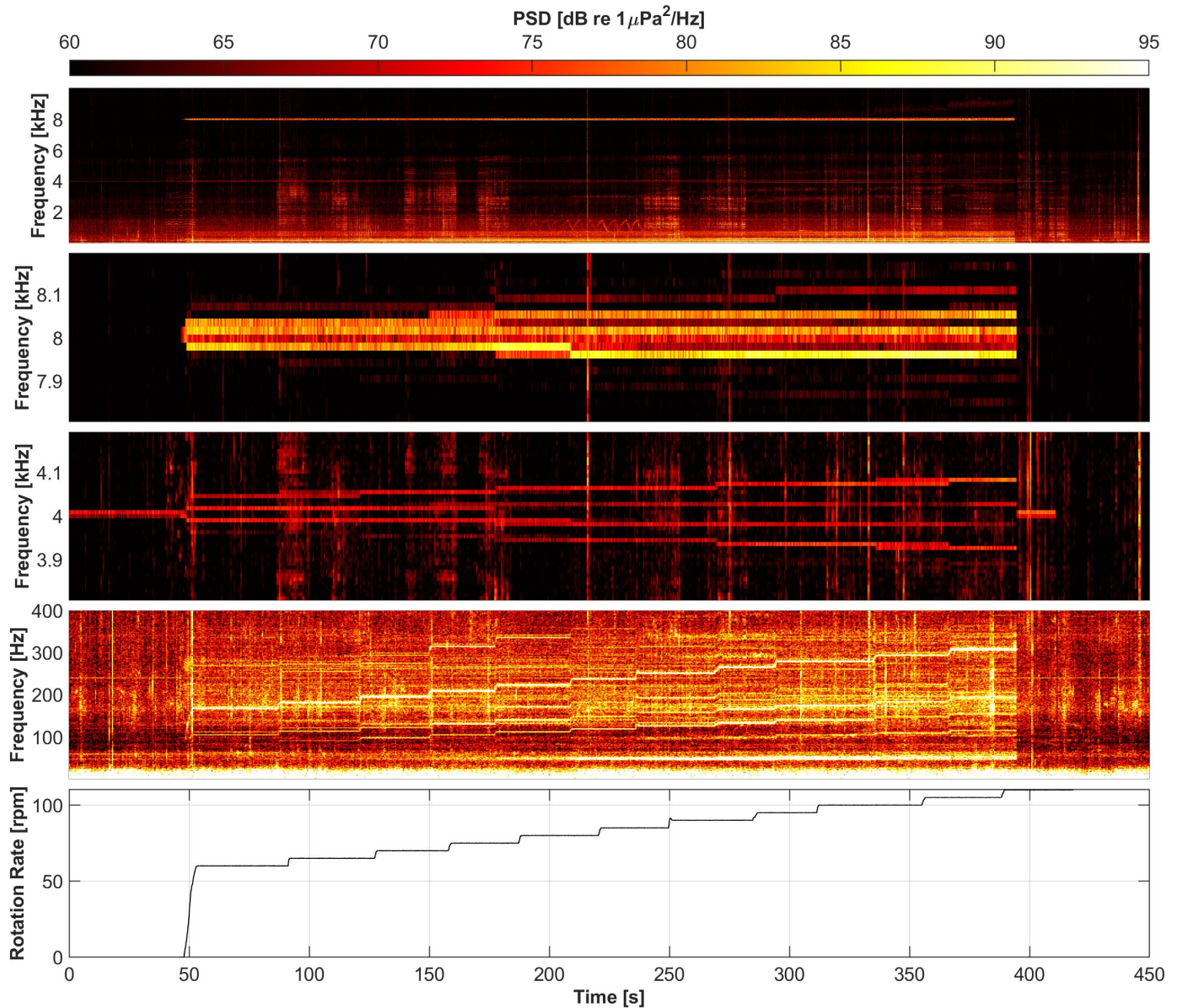


Figure 33: Measured noise during dockside turbine testing. The turbine rotates from 50-390 s and the servomotor is energized from 0-440 s. (a) Spectrogram over all frequencies of interest. Noise is most intense below 2 kHz. Once turbine rotation begins, intensity increases below 1 kHz, at 4 kHz, and at 8 kHz. (b) The spectrogram centered on 8 kHz shows a 7950-8100 Hz tone during turbine rotation, attributed to the power electronics. (c) The spectrogram centered on 4 kHz shows a 3900-4100 Hz signal while the servomotor is energized and is, therefore, attributed to the servomotor. Once turbine rotation begins, the signal bifurcates into four tones with increasing separation as the rotation rate increases. (d) The 0-400 Hz spectrogram shows

multiple tones that increase in frequency with rotation rate. (e) The rotation rate increases by 5 every 20-50 seconds, creating a step signal.

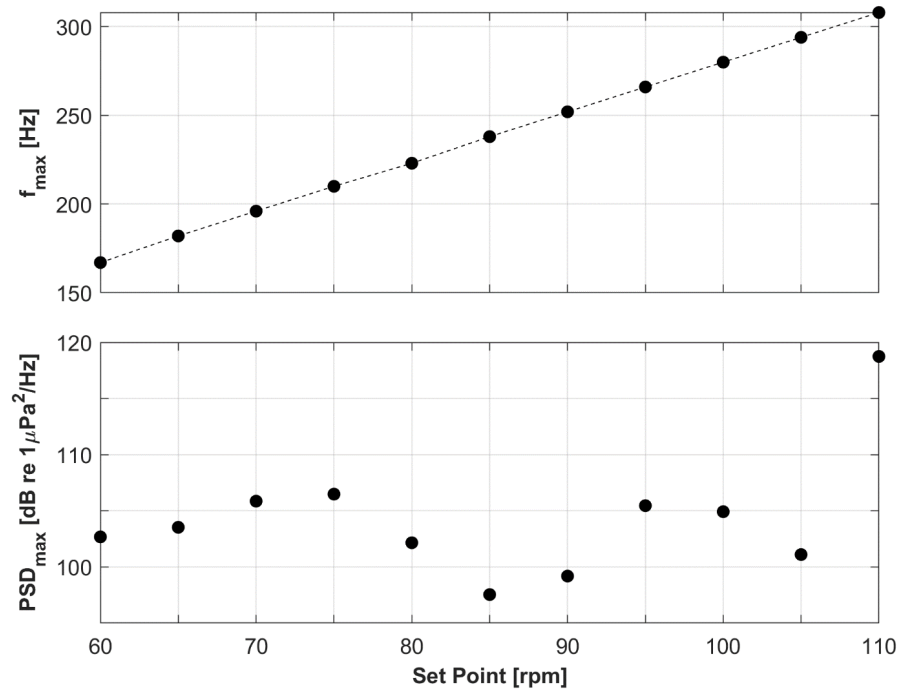


Figure 34: (top) Regression of frequency of maximum PSD in the 100 – 400 Hz range (rotor noise) against turbine rotation set point shows a linear relationship between rotation rate and frequency of peak tone. (bottom) Maximum PSD in the 100 – 400 Hz range as measured at range of 2.5 m from the axis of rotation of the turbine shows no clear dependency on rotation rate.

$1 \mu\text{Pa}^2/\text{Hz}$. This suggests that the intensity of the driveline noise changes with rotor thrust loading or that our spreading model under-predicts transmission loss between the source and the receiver. Similarly, indications of the power electronics noise around 8 kHz (Figure 35b) are lower intensity relative to the prediction, consistent with the hypothesis of higher transmission loss.

In general, ambient noise poses the greatest challenge to definitively attributing sounds to the turbine at frequencies below 3.5 kHz. In particular, the band where we had anticipated rotor noise overlaps with a variety of sound sources (Figure 37) not present in dockside testing, including contributions from RDL's generator, intermittent signals (subsequently attributed to RDL's moorings), and vessel traffic. The rationale for these attributions are now discussed.

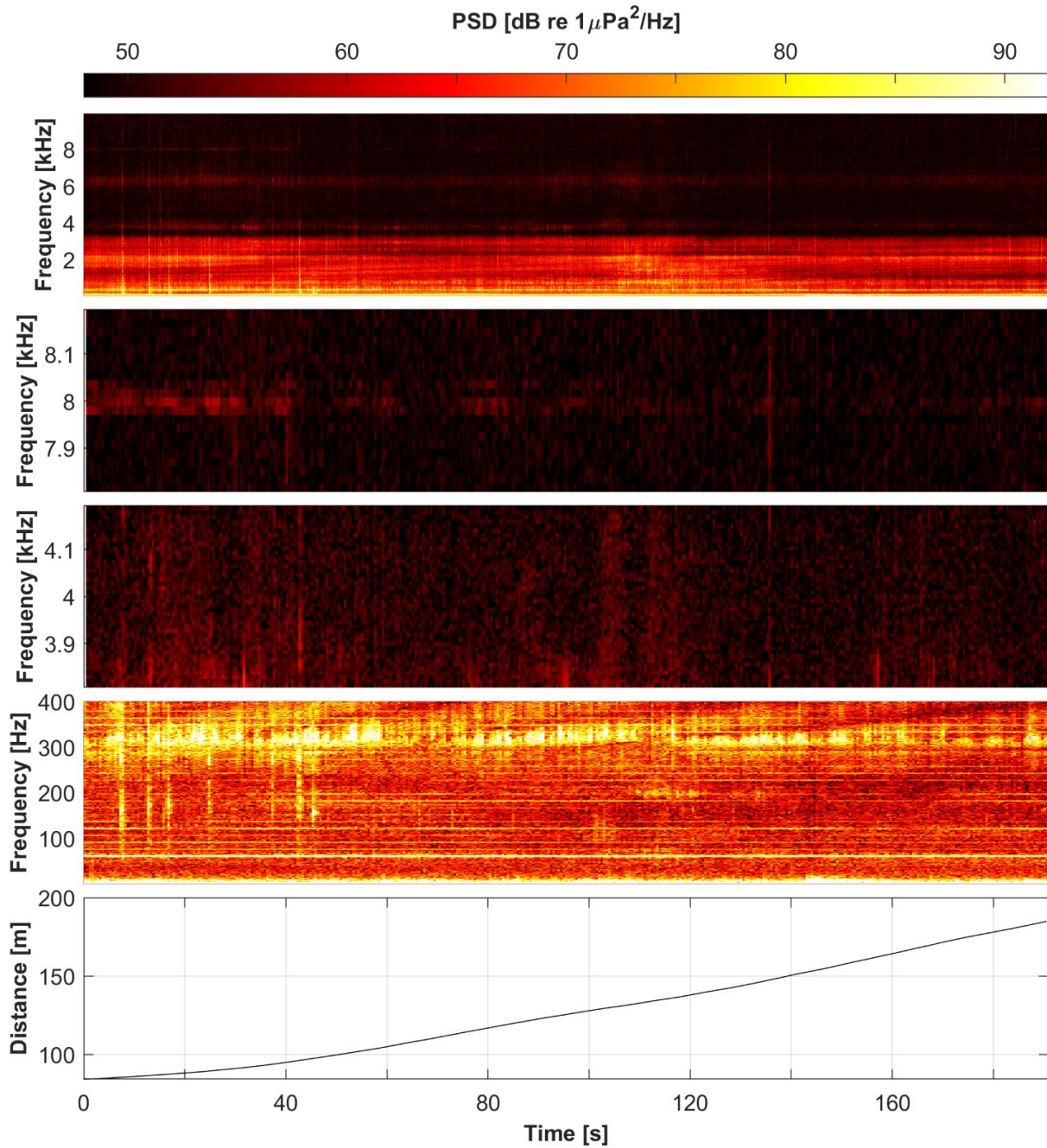


Figure 35: Measured noise during track C1, presented in the same frequency bands as for dockside testing to highlight presence/absence of turbine-attributed sound. During this drift, the turbine's rotation rate varied from 61-63 Hz. a) Spectrogram over all frequencies of interest, demonstrating that noise is most intense at frequencies below 3.5 kHz. (b) The spectrogram centered on 8 kHz shows a faint band of sound, apparent above ambient noise for the first 40 s of the track, that is attributed to the servomotor. (c) Unlike during dockside testing, the spectrogram centered at 4 kHz (expected servomotor sound) does not contain any narrowband signals. (d) The spectrogram from 0 – 400 Hz has multiple signals, including persistent narrowband and impulsive broadband signals. (e) The distance between the DAISY and the turbine steadily increases as the DAISY drifts with the

dominant currents. The weaker servomotor signal (b) is correlated with increasing distance between source and receiver.

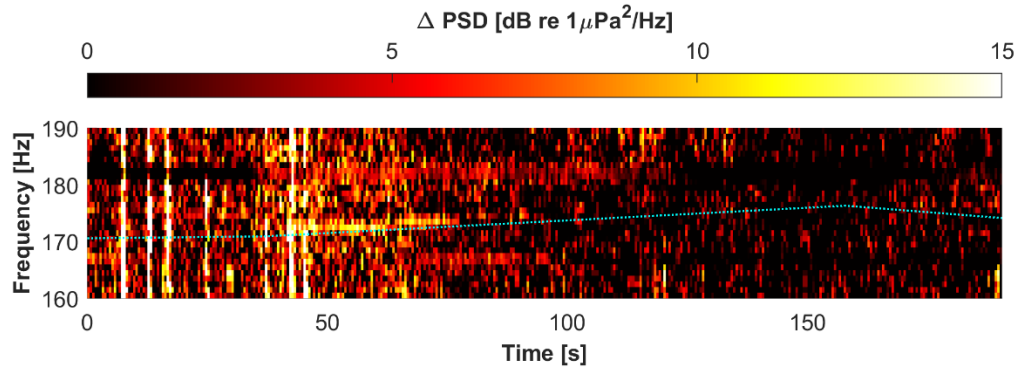


Figure 36: Normalized spectrogram highlighting anticipated turbine driveline noise from dockside testing (160-190 Hz) for the same period shown in Figure 35. This formulation shows the difference in PSD from the median PSD for each frequency, removing noise that persists across time at constant frequency. This aids in identification of low SNR horizontal banding structure (e.g., at approximately 165 Hz and 180 Hz in Figure 9), which is attributed to RDL's generator. The dotted cyan line reflects our prediction for the frequency of turbine rotor sound based on operating state and DAISY-turbine separation distance. There is increased intensity along this trajectory from ~40-80 s, which might be attributable to the turbine and overlaps with the period during which the servomotor sound is detected. For most of the drift, there is no sound above ambient at the predicted frequency.

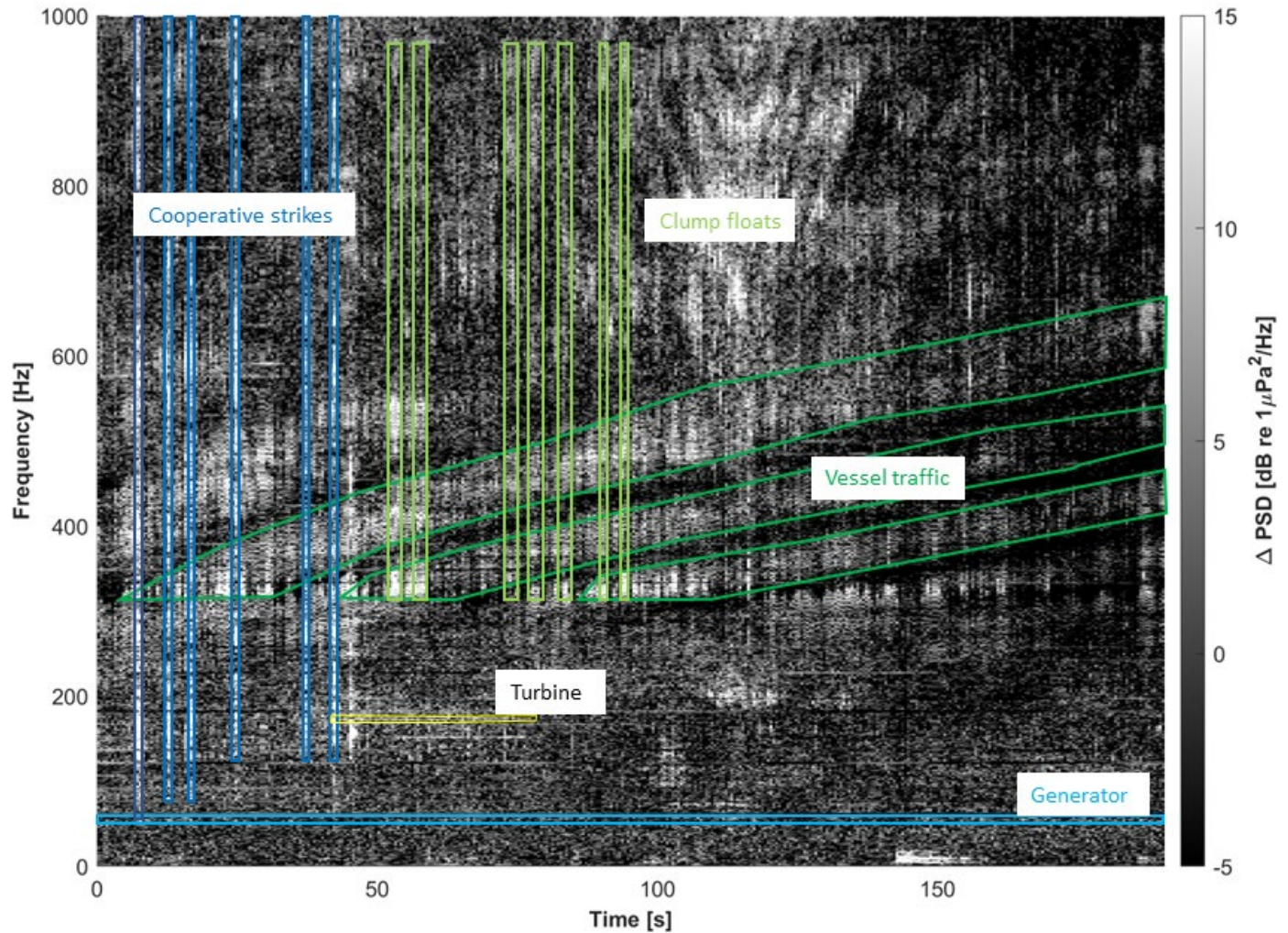


Figure 37: Soundscape from 0-1 kHz for track C1 with representative annotations denoting attributed sources—the turbine driveline (low certainty), RDL generator, cooperative strikes, clump floats, and vessel traffic. As a relative spectrogram, this visualization emphasizes signals that change over time. Noises attributed to the generator presents as a constant set of, narrow band signals that occur every 15 Hz, starting at 60 Hz. Relative PSD was chosen for visualization to prevent the generator signals from dominating the figure. Because they are relatively consistent in time, they appear as approximate nulls in the relative spectrogram. Limited noise attributed to the turbine driveline sound is visible, ~170 Hz from 40-80 s. Cooperative sounds created for testing appear as impulsive, broadband signals at the beginning of the drift. A series of impulsive 300-1000 Hz tones are attributed to clump floats on the RDL mooring. Finally, the diagonal bands of increased intensity are attributed to another vessel underway.

Of the ambient noise sources identified, the tones we attribute to the RDL generator (Figure 37) overlap the most with the predicted rotor noise frequency range. The main tone we attribute to the generator is a strong, narrowband tone at 60 Hz present in all drifts, with strong harmonics of this tone every 60 Hz (Figure 38). There are also less intense tones every 15 Hz starting at 75 Hz and extending to at least 1270 Hz where their intensity drops below the ambient noise floor. These can be attributed to the generator because of their frequency, consistency over time, and changes in intensity with location. The generator has two pole pairs and rotates at 1800 rpm. The frequency associated with this is given by the product of the rotation rate (in cycles/second) and the number of pole pairs, which, for this specific generator, is 60 Hz. Since the rotation rate remains constant, signals from the generator should not modulate in frequency, which is consistent with observations. Additionally, the 60 Hz tone is most intense near the port (west) side of the vessel (Figure 39), which is where the RDL generator was located. We note that localization (subsequently used to identify sound from the mooring) would be complicated by the consistency of this noise over short timescales (i.e., drift duration) and the long baseline of the DAISYs so is not employed here.

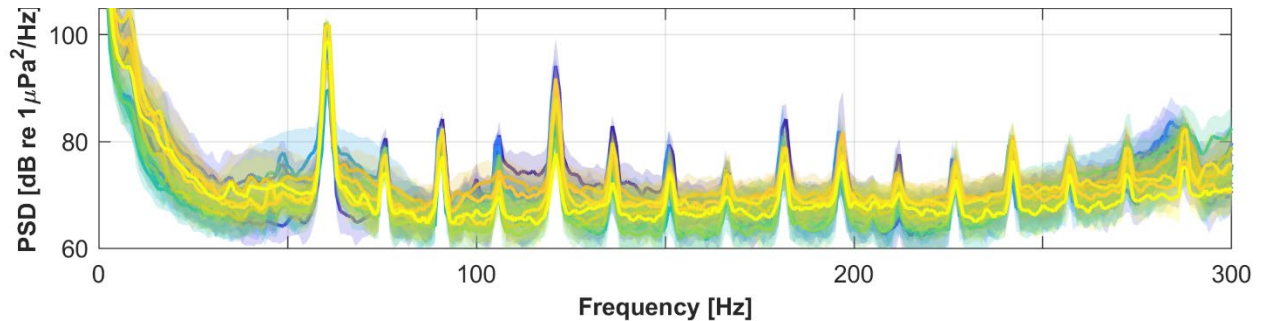


Figure 38: Composite periodograms of all tracks for the duration of their drifts. Each colored line represents the mean intensity at each frequency for a track with the translucent regions encompassing the 25-75th percentile. Starting at 60 Hz, all of the tracks have harmonic peaks every 15 Hz. These originate from the 60 Hz tone associated with the fundamental frequency of the RDL generator due to its rotation speed and number of pole pairs.

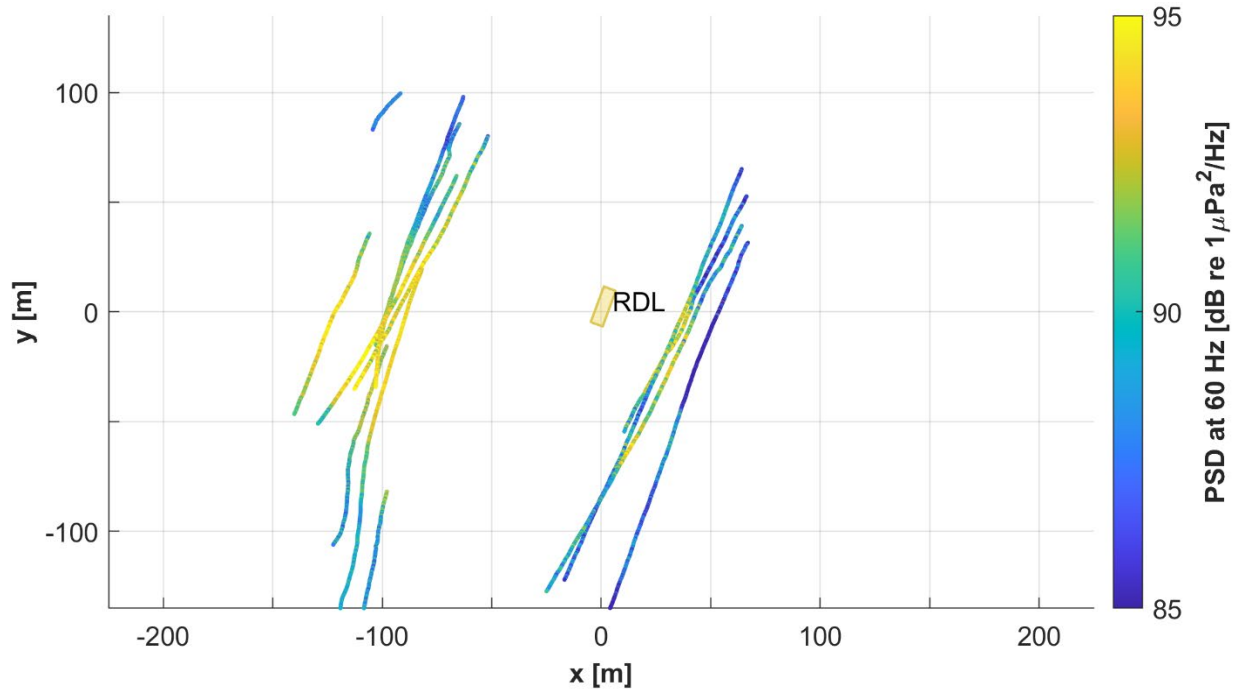


Figure 39: Spatial variation in intensity of the 60 Hz tone. The color of each track denotes the PSD at 60 Hz along a DAISY trajectory. The intensity is highest to the west of RDL, which corresponds to the location of the generator exhaust port.

As the generator signals are mostly consistent across time, they can be filtered for visualization by subtracting the median value (e.g., Figure 36). However, this strategy cannot be utilized in drifts where the rotor noise frequency is predicted to intersect with a generator frequency. For example, in the drift shown in Figure 14 the turbine is expected to produce sound at a frequency of 145-150 Hz. This overlaps with a generator harmonic at 100 s, likely masking any potential rotor sound during this period. In addition to the generator, other sound sources present in the dataset include another vessel and impulsive broadband sounds, which we attribute to cooperative testing and to the moorings (Section 3.3.3.3).

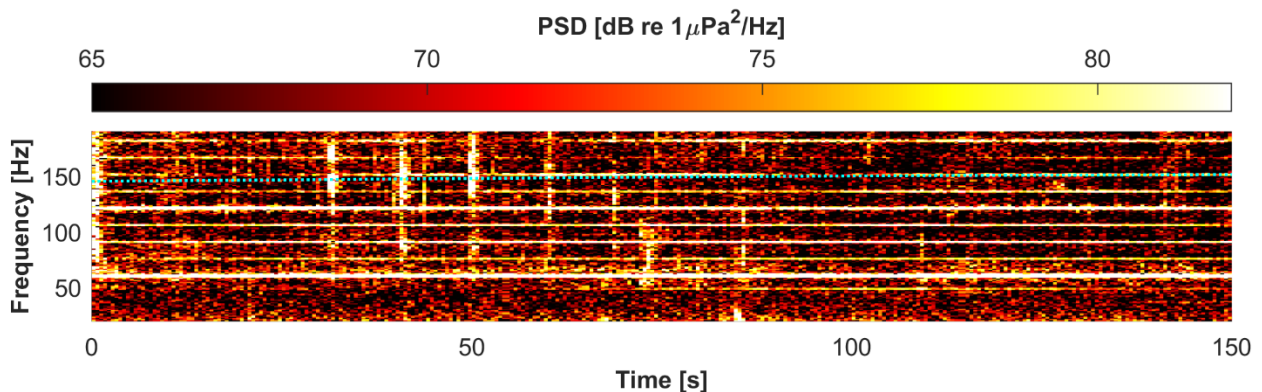


Figure 40: The spectrogram for track B1 shows the relatively intense signals attributed to RDL's generator. In addition to the primary tone at 60 Hz and first harmonic at 120 Hz, lower intensity peaks every 15 Hz are observed starting at 75 Hz. The harmonic at 150 Hz intersects the predicted turbine rotor sound frequency (dashed cyan line) at about 100 s, masking potential turbine rotor noise.

3.3.3 Source Localization for Attribution

As discussed in Section 2. *Localization*, the cooperative noises created by striking the RDL deck with a pipe create clear, broadband, impulsive signals. These could be easily attributed based on their known timing, but also serve as a test for localization methods. As shown in Figure 41, the strikes generally localized to within 20 m of RDL's location. This is indicative of the effectiveness of the overall localization strategy for sufficiently high signal-to-noise ratios (SNR) with the minimum number of required receivers. We note that given that the strike noise is radiated by the hull, the “point” source size is relatively large and on the same order as vessel size.

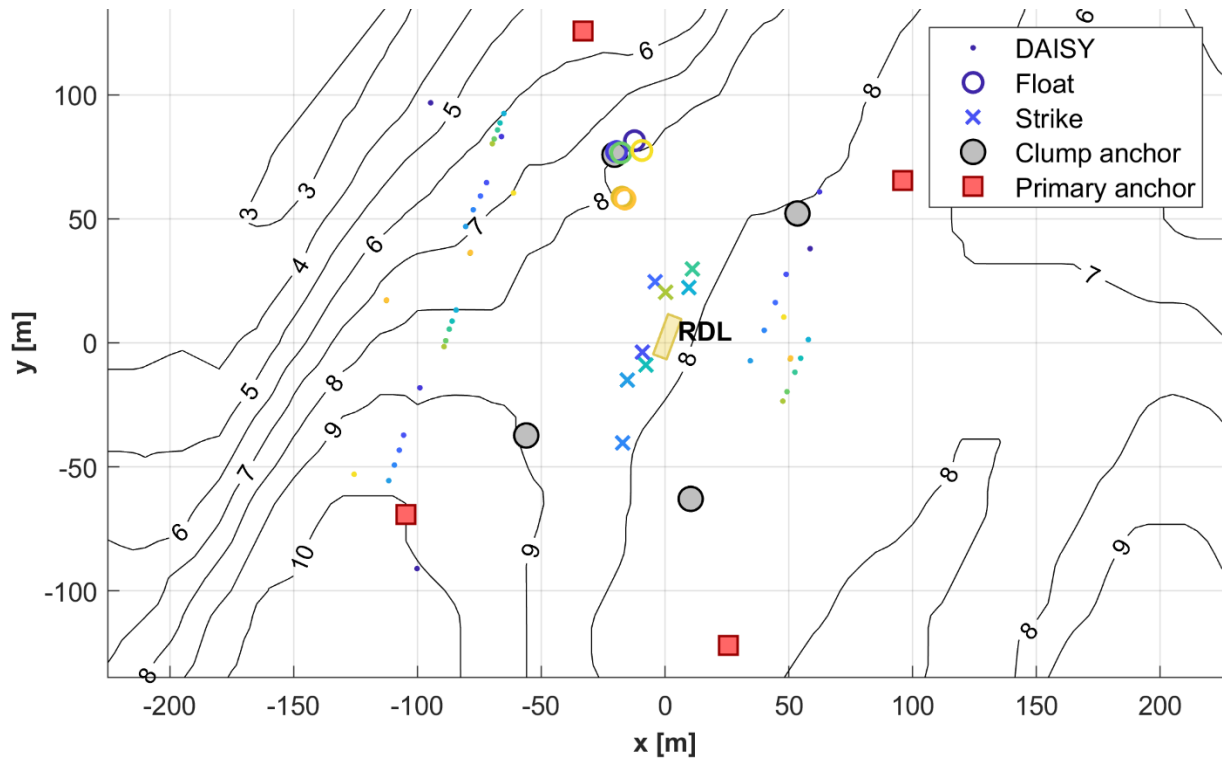


Figure 41: Composite localization results for all drifts. For each localized sound, there are three dots marking the locations of the three DAISYs at the time of the signal. The estimated location for the sound source is marked in the same color. The cooperative strike localizations are all within 50 m of RDL (all but one within 20 m). The float noise localizations are all within 20 m of the NW clump weight.

Similarly, we can employ localization to identify the source of the recurring sound between 300 and 1000 Hz (Figure 37, highest intensity in the 300-550 Hz range) that is present in all drifts. Localizations of several instances of this sound all produce results in the vicinity of the NW clump weight (Figure 41). Noise levels observed in the 300-550 Hz band are also highest in this region (Figure 42). These suggest that the sound is attributable to the clump weight. The sound presents as tapping, which we hypothesize

to originate from periodic contact between the floats located near the clump weights on this specific leg of the mooring.

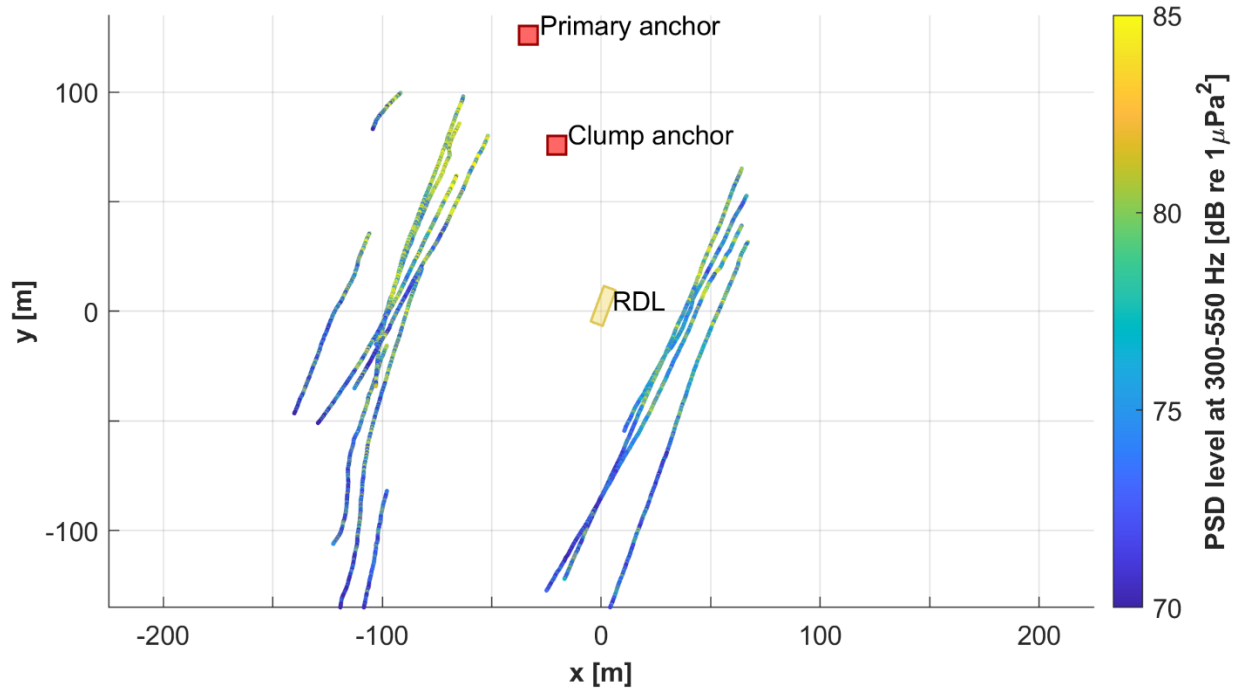


Figure 42: Spatial variation in intensity in the 300-550 Hz band across all drifts shows that this band is dominated by the periodic signal that is most intense in the vicinity of the NW clump weight.

3.4 Lessons Learned

The DAISY measurements demonstrate both the relatively small acoustic footprint associated with the turbine and the complexity of obtaining high-quality measurements under the test conditions. Rotor driveline noise could not be identified with high confidence, demonstrating that radiated noise from the system does not consistently exceed ambient spectral levels at these low frequencies (~ 65 dB re $1 \mu\text{Pa}^2/\text{Hz}$ at 130-180 Hz). Constituents at 4 and 8 kHz, attributed to the servomotor and power electronics, respectively, could be identified. However, at ranges of 40-150 m from the source, these signals had minimal SNRs (~ 6 dB), making them difficult to detect. Thus, across the entire range of measured frequencies, we only observed minor contributions to noise from the operating turbine.

In dockside testing, we were able to identify noise from the driveline (100-400 Hz), servomotor (~ 4 kHz), and power electronics (~ 8 kHz). There was a strong correlation between the rotation rate of the turbine and the frequency of the turbine noises, particularly in the driveline frequency range. However, there was no obvious correlation between the rotation rate and the intensity of the noise. Although we could not confidently identify driveline noise in our field data, the servomotor and power electronics noises both presented in the field at the same frequency ranges as in dockside testing. Dockside extrapolation was a valuable tool for identifying these signals in the much lower SNR field data. In future work, if driveline noise were observable, we recommend repeating dockside testing and comparing the driveline noise predictions to the field results.

Although we were not able to attempt localization of any turbine sounds due to low SNR and signal ambiguity, other sounds were successfully localized despite the challenging, shallow-water environment.

The cooperative sounds created by striking the RDL deck provided useful information about the accuracy of our localization methods. Most of the strikes localized to within 20 m of their source location. We attribute a portion of the localization error in these results to propagation of the strike sound through the metal hull, which is unlikely to act as a point source. In addition, the shallow water environment produces complex multi-path arrival structures with relatively small differences in arrival time, which makes identifying the precise signal arrival time more complex. This ambiguity will be decreased in situations with deeper water. Localization accuracy would also increase with an over-determined array of receivers (i.e., more than three DAISYs). In addition, we are continuing to develop alternate algorithms and improvements to more precisely identify arrival times.

Based on the strength of our results for the cooperative sounds with a known source location, we were able to use localization to identify unknown signals. We hypothesized that the 300-550 Hz tapping sound which persisted throughout the acoustic data came from mooring floats. Localization supported this hypothesis and attributed the sound specifically to clump floats on the NW mooring. Despite the lower SNR, these tapping sounds localized to a more precise area than the cooperative strike sounds did, most likely due to the smaller size of the source (the clump anchor floats v. the RDL hull). In addition to eliminating this sound as a possible turbine sound, these results tell us specifically which part of the mooring could be fixed or improved for future deployments to minimize noise.

In summary, the turbine did not produce a detectable acoustic signal and thus did not contribute a significant amount of noise relative to ambient conditions. Some of the ambient noise came from the vessel and its mooring, so in future operations, when the turbine is deployed on a gravity foundation, it should be easier to identify turbine signals. Localization, even in these shallow waters, has been demonstrated successfully and will be a valuable tool in future research. Further work on the subject should explore different arrival time algorithms that may reduce uncertainty.

4 Task 10.2: Velocity Field Characterization

4.1 Introduction

The objective of this task was to characterize the velocity field upstream and downstream of a cross-flow turbine rotor. This information could help to contextualize patterns of animal behavior around the turbine. Because of the difficulty of obtaining such information around a field-scale rotor, data collection was performed in a laboratory flume using a geometrically scaled model and particle image velocimetry (PIV³).

4.2 Methods

4.2.1 Flume

Experiments were performed in the University of Washington's Alice C. Tyler Flume in the Harris Hydraulics Laboratory. The flume's test section is 0.76 m wide and 4.88 m long. During these experiments, the dynamic water depth was maintained at 0.51 m, the inflow velocity, measured by an acoustic Doppler velocimeter (Nortek Vectrino Profiler) positioned 5 diameters upstream of the turbine was ~ 0.9 m/s, and the water temperature was maintained at 31 °C. Inflow turbulence intensity was 1-2% throughout experiments, substantially lower than at a real-world site (Thomson et al. 2012), but similar to conditions during self-propelled vessel-based turbine testing. The Tyler Flume's walls and base are glass, providing optical access for lasers and cameras.

4.2.2 Turbine Performance

The laboratory turbine was a 1:5 scale model of the full-size turbine. An exception to this scaling was the transition point between the blade profile and support struts, where the blade chord length was enlarged (Figure 43) to provide sufficient working area for alignment pins and a locking screw. In addition, the blade preset pitch angle (angle between the chord line and tangent line to rotation direction) was 6° versus 9° for the full-size turbine (see further discussion in Section 4.4). The blades and support struts were machined from 6061 aluminum, anodized for corrosion protection, and spray painted with black matte paint to reduce the risk of laser scattering during PIV measurements.



Figure 43: Scale-model turbine in the Tyler Flume. The blade-strut connection (blade ends) deviates from the actual turbine (Figure 11) due to the size of the mounting hardware required.

³ The PIV system used here was acquired with WPTO support for ALFA Task 5.

Turbine performance was characterized using a similar setup to Polagye et al. (2019), shown in Figure 44. Turbine rotation rate was regulated by a servomotor (Yaskawa SGMCS-05B3C41) with an integrated encoder (2^{16} counts per revolution). Torque and thrust were measured by a pair of 6-axis load cells: one between the servomotor and top mounting point (ATI Mini45-IP65) and one between a bottom bearing and bottom mounting point (ATI Mini45-IP68). The upper cell measured the torque required to maintain a constant rotation rate while the lower cell measured the torque imposed by the bearing. Torque and rotation data were acquired in MATLAB Simulink Desktop Realtime at 1 kHz. Rotation rate was calculated in post-processing through numerical differentiation of angular position from the encoder.

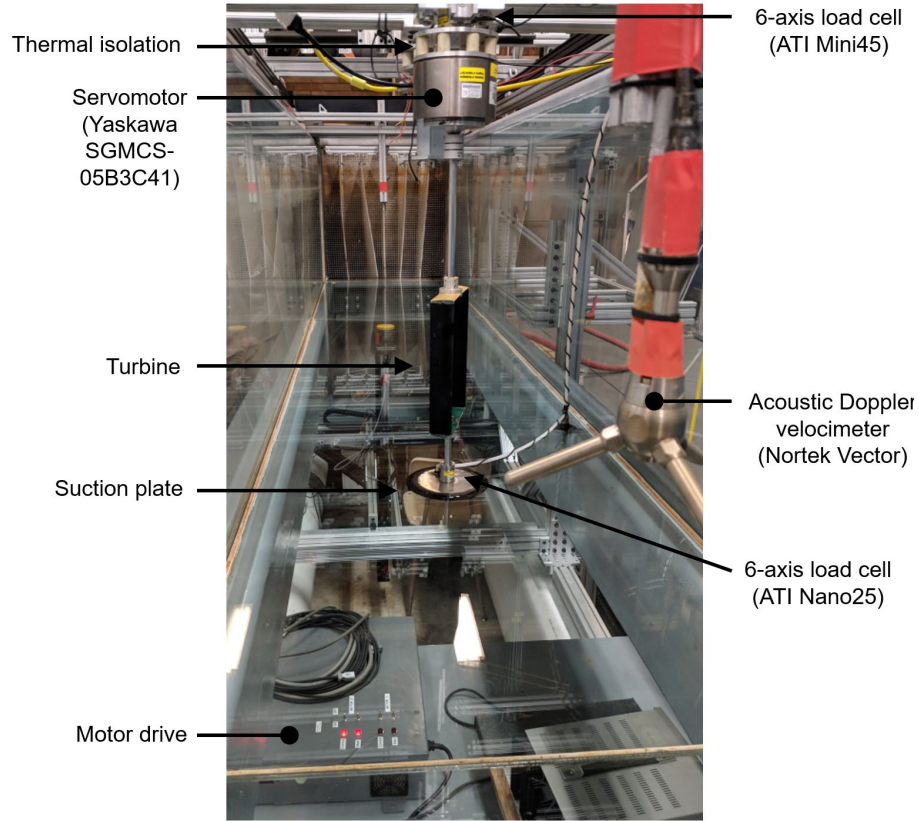


Figure 44: Performance measurement test rig (reproduced from Polagye et al. 2019). The differences between this setup and the one used for performance measurements in this study are a larger lower load cell and improved thermal isolation assembly between the servomotor and upper load cell.

Torque, thrust, and rotation rate were non-dimensionalized as a performance coefficient

$$C_P = \frac{Q\omega}{\rho U_o^3 R H'}$$

thrust coefficient

$$C_T = \frac{T}{\rho U_o^2 R H'}$$

and tip-speed ratio

$$\lambda = \frac{R\omega}{U_o}$$

where Q is the hydrodynamic torque produced by the turbine (equal to the measured torque when rotation rate is held constant), ω is the rotation rate, T is the hydrodynamic thrust, ρ is the water density

(995 kg/m^3), U_o is the inflow velocity measured by the ADV, R is the turbine radius, and H is the height (blade span and struts). These quantities are presented on a time-average basis for a given tip-speed ratio set point.

During these experiments, the blockage ratio was $\sim 10\%$ and the Reynolds number based on the turbine diameter and free stream velocity was 2×10^5 . This means that the laboratory-scale turbine is operating at reduced scale relative to the full-size system (Section 2.2.1), which depresses the performance coefficient since we are operating below the Reynolds-independent threshold, but at higher blockage, which enhances the performance coefficient (Ross and Polagye 2022). However, the flow disturbance is largely a consequence of the thrust coefficient, which is less sensitive to turbine scale and relatively small changes in blockage. As such, when the flow fields measured at laboratory scale are normalized by the inflow condition, they are expected to have reasonable quantitative agreement with the full-size turbine.

4.2.3 Particle Image Velocimetry

In general, PIV involves a combination of a relatively high speed laser and camera. The laser, located adjacent to the flume, passed through optics to generate a horizontal sheet in the flume test section. The camera, located below the flume, acquired image pairs in rapid sequence. In post-processing, software was used to correlate the motion of neutrally buoyant seeding particles ($10 \text{ }\mu\text{m}$ hollow glass beads) between frames, inferring the structure of the flow field. Here, a single camera was used to capture planar flow fields (along-channel and across-channel velocities). With a second camera, stereoscopic PIV methods could be used to characterize all three components of velocity.

Flow fields were captured using the PIV system largely described in Snortland et al. (2023). The laser in these experiments was a dual-cavity, Nd:YLF model (Continuum Terra PIV) capable of a repetition rate of 10 kHz . Images were acquired by a high-speed camera (Vision Research Phantom v641) with 2500×1600 resolution and a 50 mm lens (Snortland et al. employed a 105 mm lens for finer resolution and a smaller field of view). This arrangement resulted in a field of view (FoV) approximately 0.25 m streamwise ($1.5 D$) and 0.4 m cross-stream ($2.3 D$). The effective FoV was further reduced by variable illumination and shadowing from the turbine, but was sufficient to observe the upstream induction region where the flow around the rotor decelerates, as well as the wake and the bypass flow downstream. For logistical simplicity, the laser and cameras remained at a constant streamwise position, while the turbine was shifted between experiments to capture upstream and downstream FoV (Figure 45). The laser and camera were controlled by TSI Insight.

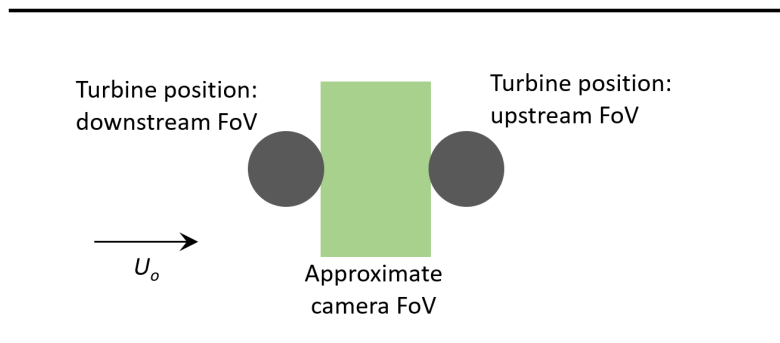


Figure 45: Top-down view of turbine and camera FoV. Turbine is centered in the flume. Blade sweep marginally intersects camera FoV.

PIV data was collected at three vertical planes defined by their elevation, z , referenced to the base of the turbine and normalized by the turbine height:

- $z/H = 0.5$: turbine mid-plane;
- $z/H = 0.9$: 90% span position; and
- $z/H = 1.1$: 110% span position (just above the turbine).

To acquire data at each elevation, the laser and camera systems were moved by motorized gantries. All data were collected at the optimal tip-speed ratio identified during performance characterization ($\lambda = 2.2$). Post-processing was performed in DaVis (version 10.2.1). This involved masking areas with low density of illuminated particles (edges of laser sheet, regions shadowed by the turbine), background subtraction using a high-pass Butterworth filter to limit the effects of illumination variability, and removal of outliers.

4.3 Results and Discussion

4.3.1 Scale-Model Performance

Turbine performance during characterization experiments and PIV flow field measurements is summarized in Figure 46. The performance coefficient (left), which does not include powertrain losses, is similar, but somewhat lower than observed for the full-size turbine (Figure 3) at similar inflow conditions. This is a combination of offsetting effects from a lower Reynolds number, higher blockage, and greater losses at the blade-strut interface due to modifications required for scale-model manufacturing. Performance was consistent and repeatable throughout the PIV measurements excepting one performance outlier caused by *one* of the clamping screws between the strut and blade loosening and backing out by ~ 3 mm. This reduced by performance coefficient by 50% and highlights the sensitivity of cross-flow turbine performance to relatively minor sources of drag near the rotor periphery. However, we observe that this had little effect on turbine thrust (Figure 46, right) which was consistent across all tests and is the primary influence on the flow field.

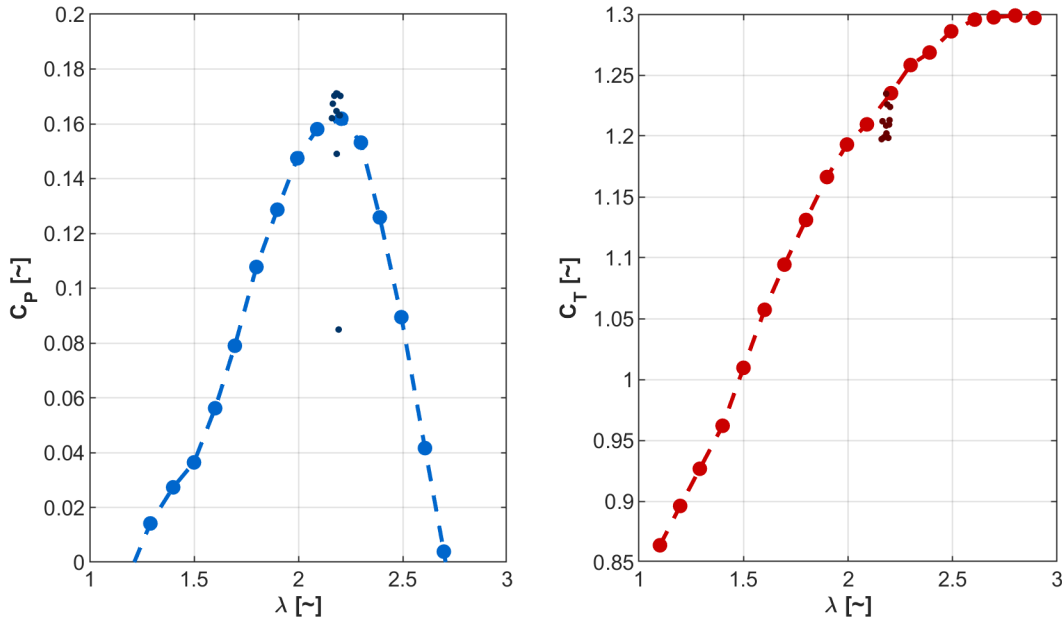


Figure 46: (left) Performance coefficient as a function of tip-speed ratio. Larger, light blue markers correspond to performance characterization to identify the optimal tip-speed ratio. Smaller, dark blue markets correspond to data acquisition during PIV flow-field visualization. (right) Same information for thrust coefficient.

4.3.2 Velocity Fields

Figure 47 shows the time-average velocity magnitude upstream and downstream of the turbine at the three vertical planes. Recall that $z/H = 0.5$ corresponds to the turbine midplane and that the velocity is largely symmetric about this axis. Regions without data are periodically shadowed by the blades.

Starting with the upstream position, we observe a slight deceleration of the velocity field within the blade span ($z/H = 0.5$ and $z/H = 0.9$). This “induction” is a consequence of the momentum loss associated with the turbine. Due to mass conservation, this deceleration through the rotor plane is accompanied by an acceleration of flow around the turbine. This deflects the incoming streamlines around the rotor and is the source of the apparent “evasion” of the turbine by passive objects (Section 2.3.4). Just outside of the blade span ($z/H = 1.1$), induction is relatively subtle. From this, we hypothesize that a fish approaching the turbine within the blade span would experience a force deflecting it laterally. Depending on the fish position, this might result in deflection entirely around the rotor or through a different portion of the rotor plane.

Downstream of the turbine, the momentum loss associated with the turbine produces a significant wake, in which the velocity is reduced to less than 10% of the inflow condition. This is most apparent within the blade span, but also apparent above the rotor plane due to wake mixing with the free stream. Similarly, we note that the wake velocity is lowest near the turbine mid-plane, while mixing with the free stream above the turbine is observable near the blade ends ($z/H = 0.9$). From this, we hypothesize that there is a relatively low energetic cost for a fish to hold position in the wake, similar to an area of refuge behind a solid structure.

4.4 Lessons Learned

During initial lab-scale testing, the maximum performance coefficient was found to be ~4%, substantially lower than for the full-size turbine. The root cause was identified as a misinterpretation of the preset pitch angle when the model was being designed in 2020. By rotating the blade about the leading edge of the profile at the strut-blade interface, rather than the quarter-chord point on the main profile, the resulting preset pitch angle was more than 10° degrees greater than intended. In discussing this issue with the project team, we discovered that a similar mistake had been made in the design of the full-scale turbine. However, because that blade has a constant profile along its span, the error in preset pitch was only a few degrees and, consequently, had less impact on performance. This demonstrates the benefits of benchmark comparisons at different scales and documentation of engineering conventions in cross-flow turbine design.

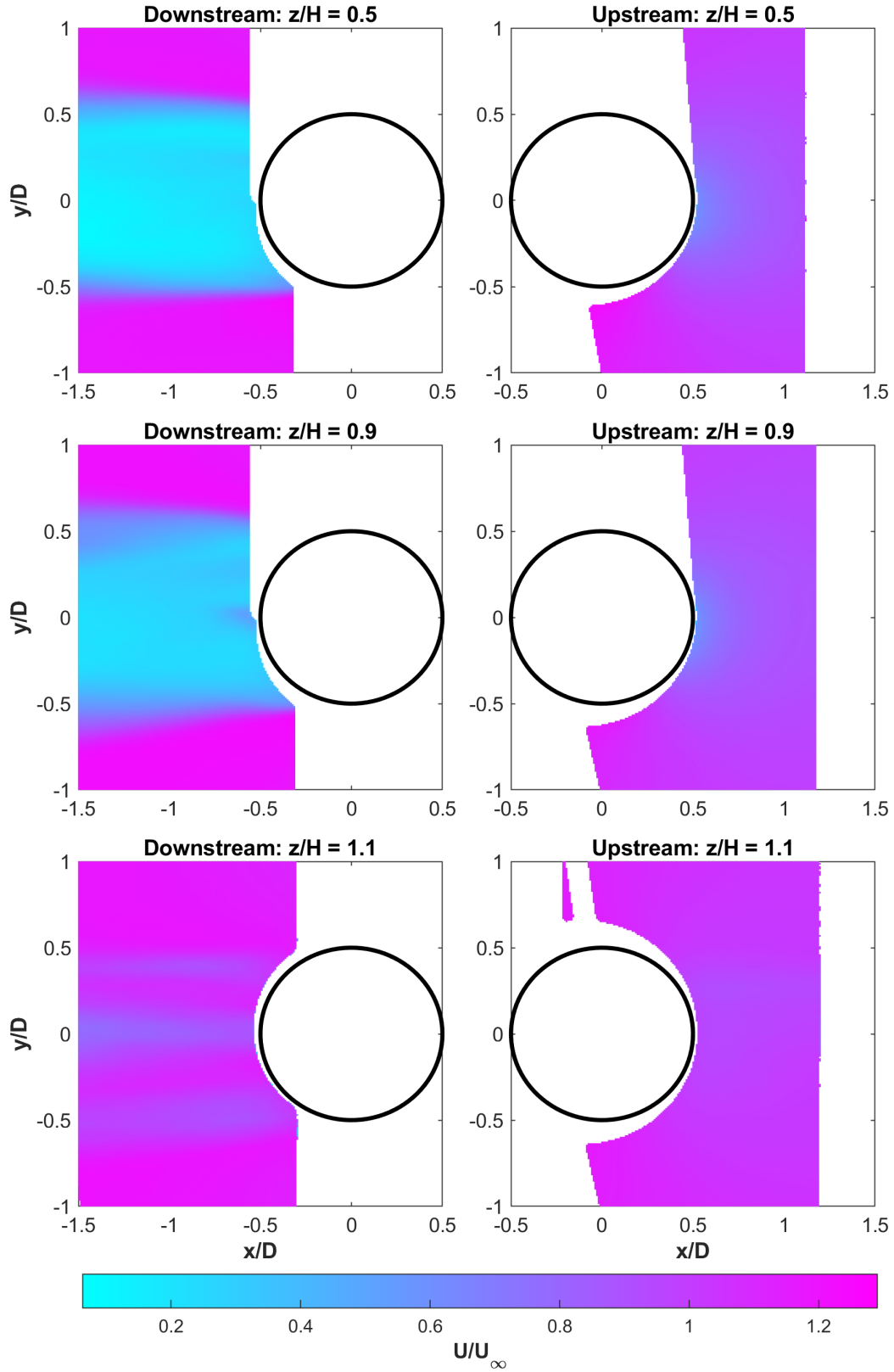


Figure 47: Velocity magnitude upstream and downstream of the turbine normalized by the inflow velocity, U_∞ , and turbine diameter, D . Inflow velocity is from left to right. Black circle denotes turbine swept area.

5 Task 10.3: Behavioral Evaluation

5.1 Introduction

The objectives for automated behavioral evaluation are to take the detection and tracking information (i.e., Task 10.1) and estimate target behavior type and associated collision risk. Through this process, we identified three general behaviors that could likely be tracked by a stereo camera system:

- Target avoids the turbine (either passively or actively);
- Target enters the turbine (either exits or remains within); and
- Target exits the turbine (either stays in the wake or moves through the wake).

5.2 Methods

Categorization

We developed a model for the characterization of target behavior when encountering a turbine. Given that the majority of the data available for this study were small fish (Section 2.3.2), we focused specifically on fish behavior characterization. The overall framework involves using attributes extracted from automatic stereo tracking of fish targets (e.g., fish velocity, body angle, distance from turbine) to categorize fish behaviors (Figure 48) and assign a quantitative collision risk (ranging from 0 to 1). Fish can either avoid the turbine by:

- Milling in place during slack tide (no ambient flow): “low” collision risk (~0.0)
- Passing around turbine (no change in trajectory): “low” collision risk (~ 0.25)
- Actively avoiding turbine (change in trajectory): “low” collision risk (~ 0.25)

or entering the turbine and then:

- Exiting turbine and moving through the wake: “medium” collision risk (~0.50)
- Exiting turbine and remaining in the wake: “high” collision risk (~0.75)
- Remaining within the swept area of turbine: “very high” collision risk (~1.0).

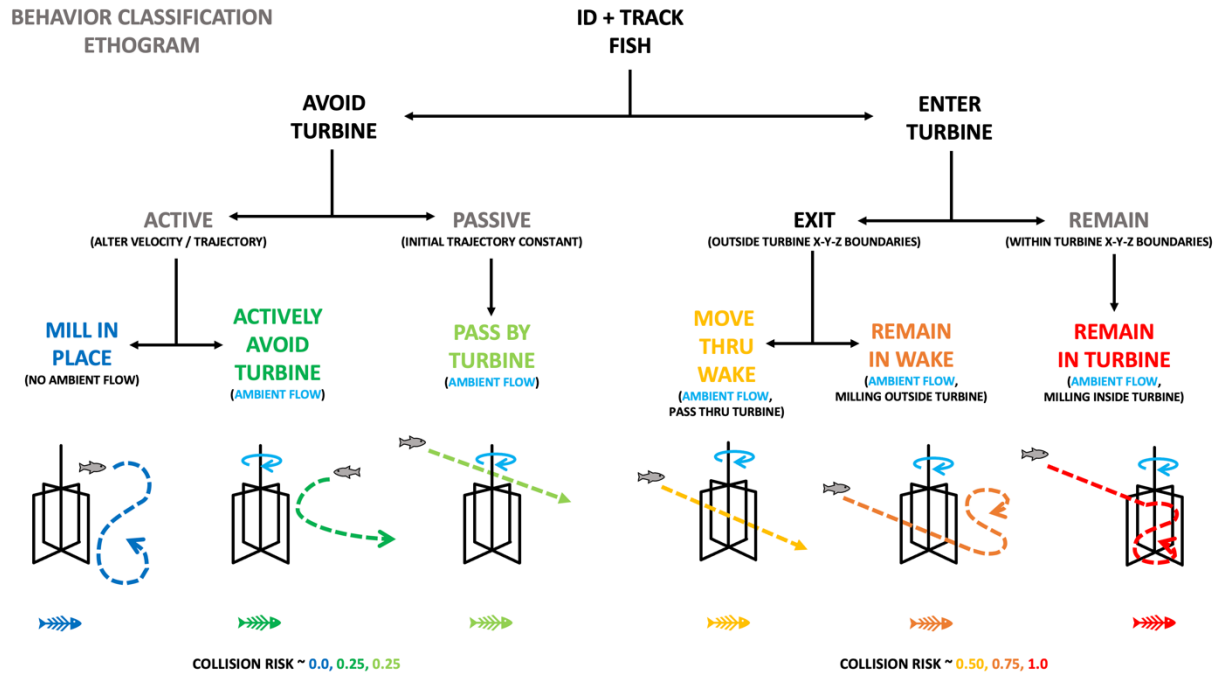


Figure 48: Collision risk ethogram based on Viehman and Zydlowski (2015). An ethogram is akin to a hierarchical “flow chart”, or dichotomous key, that relies on the presence or absence of opposing characteristics to qualitatively define behaviors in fish.

Given challenges developing sufficient end-to-end tracking on this dataset (Section 2.3.6), we focus on the development of a collision risk metric *if* such data were present. The pipeline uses the R programming language for easier integration with other similar stacks, but could be ported to Python or other languages for live collision detection. In this setup, the collision risk pipeline would be able to generate statistical information about the rates of occurrence for particular collision risk and a composite value for all detections of a certain target type.

The behavior feature extraction script would be able to extract relevant environmental data (e.g., turbidity, ambient lighting, tidal flow, turbine status) from source file nomenclature or metadata, and use it as factors for subsequent data analyses. The current script continuously calculates the distance traveled, velocity, acceleration, body angle, variance in body angle, and position of each fish relative to the turbine, as the raw tracking data files (x-y-z coordinates of head and tail feature points extracted from stereo optical camera data) are concatenated into a master data file for subsequent analysis. The quantitative identification of fish behaviors relies on a logical framework of mathematical definitions that define each behavior by the change in linear (e.g., relative velocity) and angular (e.g., mean body angle) movements of fish over time relative to that of the turbine (Table 5).

Table 5: Behavior matrix

ALFA task 10.3 Behavioral Characterization - Matrix								
Behavior	Slack tide only?	Distance (D) (fish → turbine)	Variance (Df-t)	Velocity (V, fish)	Variance (Vf-t)	Theta (avg body angle)	Variance (Theta, fish)	collision?
Mill in Place	Y	< 1 L (could be greater)	< 1 L ² (could be greater)	< 0.5 BL/s	± < pi/4 radian	averages ~ 0	MRL = < 0.5	low (~0.0)
Avoid Turbine	N	> 1 L (need 3D depth)	> 1 L ² (need 3D depth)	0.5 - 1.0 BL/s	± > pi/2 radian	~ 0	< 0.5	low (~0.25)
Pass Around Turbine (front/behind)	N	> 1 L	> 1 L ²	> 0.5 - 1.0 BL/s	± < pi/4 radian	~ ±1 (not 0)	0.75 - 1.0	low (~0.25)
Enter Turbine (active?)	N	(trend) > to < 1 L	(trend) > to < 1 L ²	< 0.5 - 1.0 BL/s	± < pi/4 radian	~ ±1 (not 0)	0.75 - 1.0	med. (~0.5)
Exit Turbine, move thru wake (active?)	N	(trend) < to > 1 L	(trend) < to > 1 L ²	> 0.5 - 1.0 BL/s	± > pi/2 radian	~ ±1 (not 0)	0.5 - 0.75	high (~0.75)
Exit Turbine, remain in wake (active?)	N	(trend) < to > 1 L	(trend) < to > 1 L ²	< 0.5 - 1.0 BL/s	± pi/4 - pi/2 radian	~ between ± 0.5, (incl 0)	0.5 - 0.75	high (~0.75)
Remain within turbine (active?)	N	(trend) < < 1 L	(trend) < < 1 L ²	< 0.5 BL/s ?	± < pi/4 radian	~ 0	< 0.5	very high (~1.0)
Assume some behaviors NOT possible during slack tide (e.g., remain in wake)								
Flow definition: range from +1 (incoming) to -1 (outgoing); 0 = slack								
Turbine definition = XY (lower left) - XY (upper right)								
Distance "L" = effect radius = ±1 L x W of turbine								
Fish definition = XY (head) - XY (tail)								
Centroid definition = (Xh+Xt)/2, (Yh+Yt)/2								
BL/s = body length of fish/sec								
Body angle (radians) definition = from XY (tail) to XY (head)								
Does theta correlate w/ flow direction? +1 to 0 to -1								
Variance in theta (radians) = Mean Resultant Length definition: 0 = high, 1 = no angle variance								

Reliable behavior identification will be accomplished by adjusting the set point values of each behavioral definition within the extraction script. By tabulating the identified behavioral observations across the data set, the script will calculate a collision risk factor (“none” to “very highly likely”, or 0.0 to 1.0), for each fish behavior. Assuming sufficient data, collision risk factors can be derived for a given species under the observed environmental conditions so that direct correlations between collision risk (e.g., low versus high) and ambient conditions (e.g., day versus night) can be made.

5.3 Results and Discussion

5.3.1 Demonstration of Manual Categorization

The challenge with developing a fully automated pipeline for fish detection and tracking is that any ML model would require significantly more annotated data than was collected during the Agate Pass deployment to perform reliably under a variety of environmental conditions. For example, changes in water clarity, water flow rates, ambient lighting, number of fish, and species composition all increase the dimensionality of necessary training data. A challenge for this particular data set is that the totality of data collection and water quality were insufficient to generate a sufficiently large collection of behavioral data and collision events to evaluate the framework.

Figure 49 and Figure 50 provide two examples of detection of fish and example behaviors that these fish took. In both cases, the turbine was not rotating.

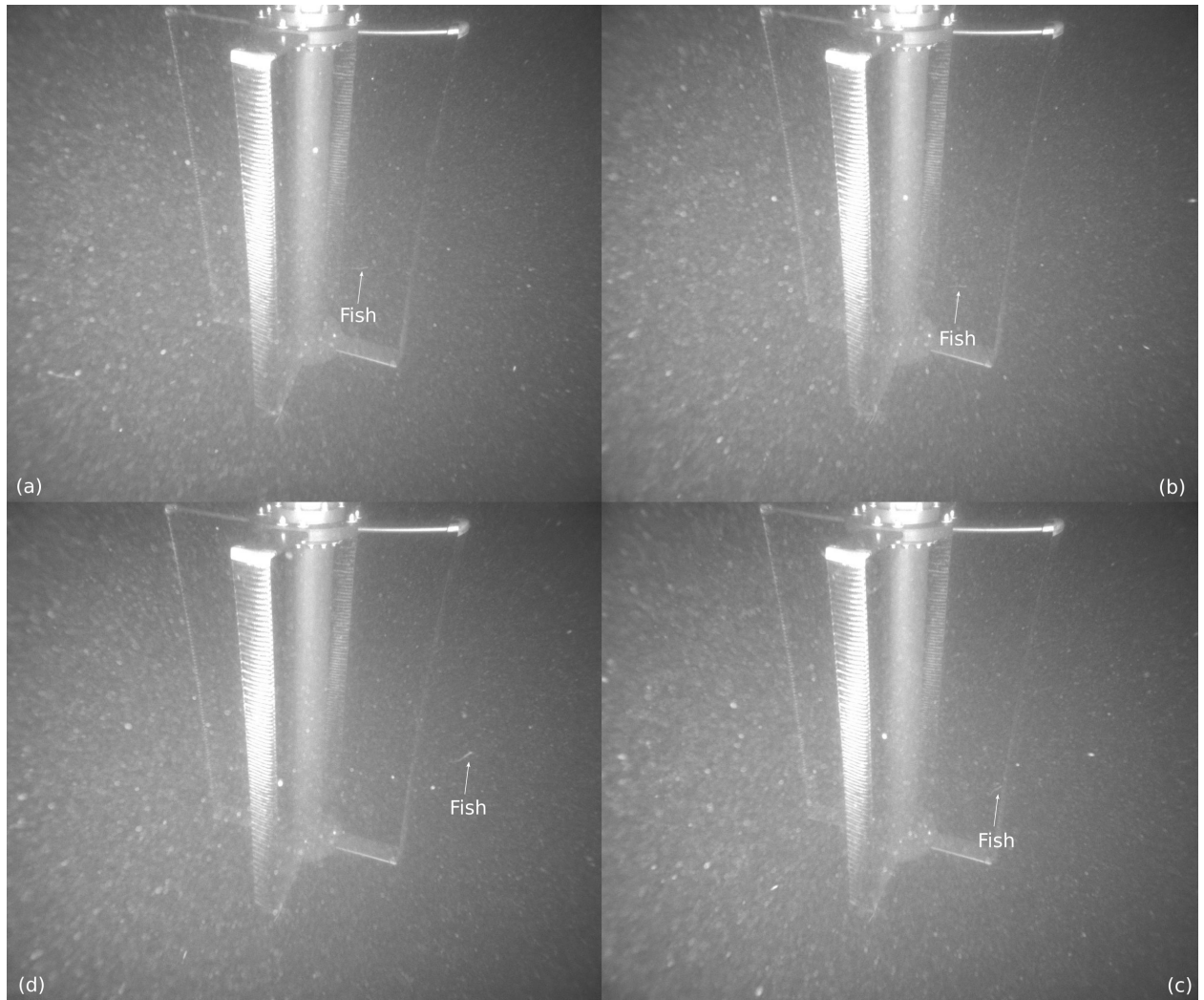


Figure 49: Example of a fish passing through the turbine, with frames increasing temporally in a clockwise manner from (a) to (d). Given that this fish entered the turbine “wake” before exiting the turbine with non-negligible velocity, this would be categorized as a “move through wake” example with a moderate collision risk if the turbine had been spinning.

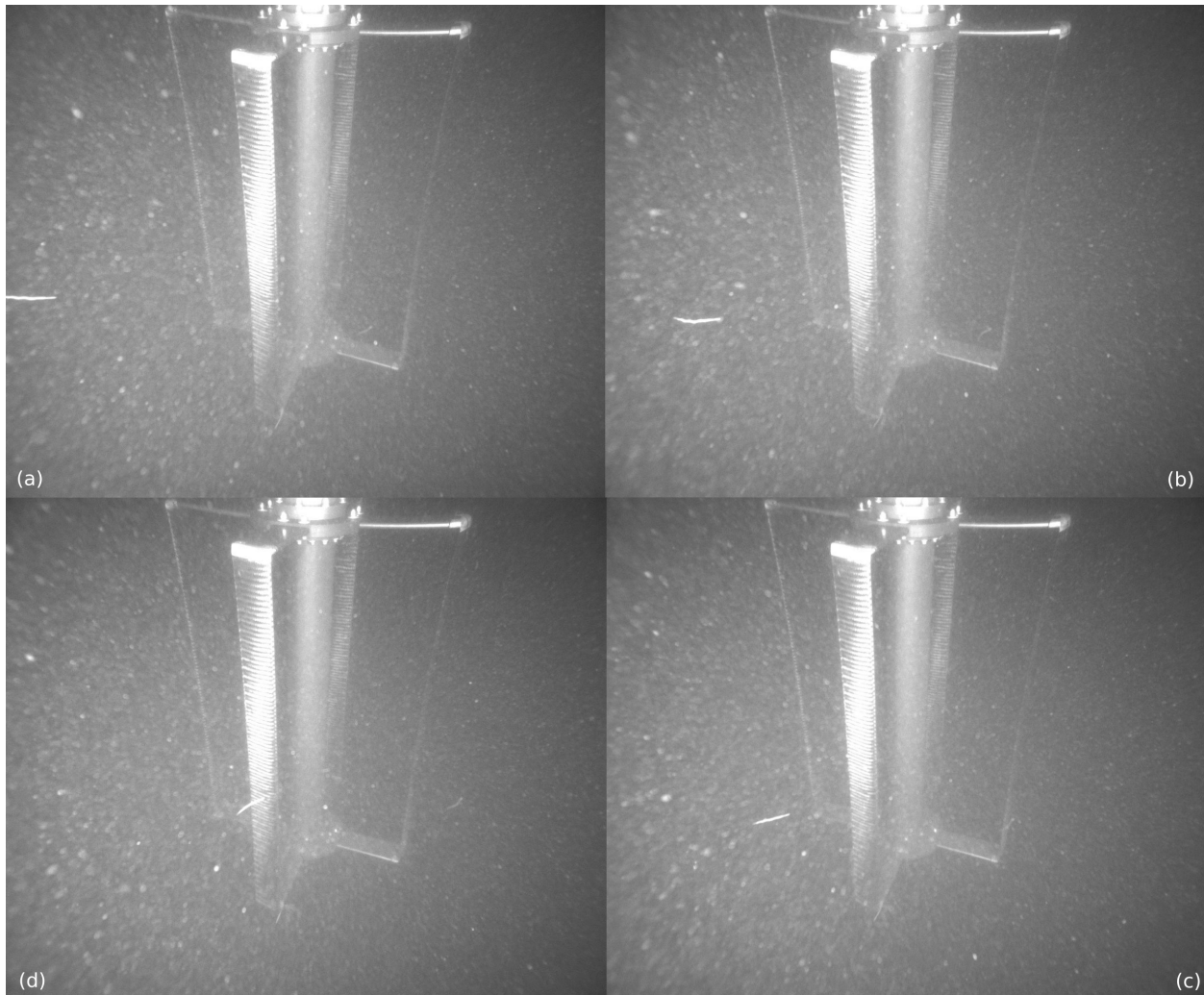


Figure 50: Example of two fish swimming in front of the turbine, with frames increasing temporally in a clockwise manner from (a) to (d). In this case, both of the fish avoid the turbine passively, therefore this case would be given a “Pass by Turbine” designation with low collision risk, had the turbine been rotating.

5.3.2 Recommendations for Future Data Collection

To improve the quality of data collected, improvements could be made to camera hardware, lighting, and study duration.

Cameras should use the “fastest” lenses available (large aperture, small f-stop) to allow more light to reach the sensor. This would reduce noise and yield better data, but may limit the number of cameras that are suitable for deployment. If data bandwidths and camera hardware allow, the cameras should sample at a higher data rate (30-60 frames per second). This should be balanced against the “speed”, or maximum aperture, of the lens because the faster sampling rate will require a larger aperture for sufficient light to reach the sensor.

Artificial lights could be used, even during the day, to fill in shadows and reduce excessive contrast due to backlighting from ambient light. Either strobes or continuous LEDs are a possibility, though strobe repetition rates can be limited by capacitor recharge time scales. Continuous lighting of either type does, however, have the possibility of altering animal behavior, such that collision risks could be biased by avoidance or attraction. This could be addressed by triggering illumination only when targets are

detected in an active sonar data stream, though, as noted in Section 2.4, target co-registration may be challenging in some circumstances. Regardless of light duration, backscatter from particulates in the water column would be reduced by placing the artificial light source far to the side and off axis from the camera lens. However, this requires the physical ability to deploy lighting in such a configuration, which may not be possible for some turbine architectures.

Finally, as previously alluded to, training an effective and reliable model for target detection and tracking in optical data would require gathering as much data as possible through multiple, long deployments under a variety of environmental conditions (e.g., low/high numbers of fish, time of day, season, turbidity, plankton blooms, tidal flow). This would likely result in models that are robust to behavioral identification under changing ambient conditions. At the same time, for prototype turbines and instrumentation, collecting long-term data can be challenging due to issues with either system that require maintenance intervention to restore functionality.

5.4 Lessons Learned

If automated identification, tracking, behavioral classification and collision risk are important goals for a project, then data collection needs to be designed with specific objectives in mind. Collecting relatively large volumes of data prior to engaging in behavioral classification is unlikely to yield desirable outcomes. If this is done, then the training data set necessary to track targets and classify behavior across a variety of environmental conditions will require at least one order of magnitude more data than was collected in Agate Pass. Similarly, data collection methods need to be optimized to collect the best quality data and maximize the likelihood of accurate and reliable target identification, tracking, and annotation.

6 Task 10.4: Collision and Encounter Risk Modeling

6.1 Introduction

Quantifying probabilities of encounters and interactions between animals and tidal turbines will help resolve the perceived risk in the operation of **tidal turbines** in the United States (Copping et al., 2020a). Currently, standard monitoring efforts to observe, characterize, and quantify encounter-impact risks are lacking, which impedes permitting and consenting of tidal turbines throughout the world. Developers are required to perform sustained monitoring to enhance mitigation measures (Rose et al., 2023; Schmitt et al., 2017), but it is not easy to collect **data at such energetic** sites (e.g., Williamson et al., 2017). The limited ability to obtain ecological data at tidal sites is directly attributable to sites being high energy environments (Shields et al., 2011) with peak tidal flows routinely exceeding 2.5 ms^{-1} (e.g., Bevelhimer et al., 2017; Sanderson et al., 2023). Ecological data constraints can lead to poorly designed studies or reduced survey efforts, which pose a lower likelihood of detecting impacts (Maclean et al., 2014), or hindering progress of development (Copping and Hemery, 2020). Identifying knowledge gaps can provide guidance to needed observations and monitoring efforts to obtain empirical data required to characterize and assess potential interactions.

This task has four primary objectives:

1. Review the literature to identify data needs to assess encounter and interaction risks between fish and tidal turbines.
2. Use empirical data to quantify conditional probabilities of fish-turbine interactions.
3. Develop an agent-based model to evaluate the influence of avoidance and aggregation behavior on encounter-impact probabilities between fish and tidal turbines.
4. Compare results, advantages, and constraints of statistical and simulation encounter-impact models.

6.2 Needs Assessment for Encounter Risk and Collision Models (Milestone 10.4.1)

Note: This milestone was completed and submitted as a report in August 2019 that is included here in its original form. The structure of the conceptual model underwent further refinement since that report and the final conceptual model is detailed in Section 6.3.

6.2.1 Rationale

A limited number of collision and encounter risk models have been developed for marine energy applications in efforts to quantify and understand animal- turbine interactions. More extensive empirical and modeling work within the wider renewable energy community has investigated collision risk between birds and bats with terrestrial or offshore wind farm turbines. Other fields that conduct collision risk models include ships, ships and oil rigs, commercial air traffic, and wildlife and vehicles. Early efforts to characterize animal-turbine interactions have relied on collections of fish downstream of turbines (e.g. Dadswell and Rulifson 1994) or annual migration studies using tagging (e.g. Rulifson et al. 1987). Among models to date, each development has occurred independently and no comparison or evaluation of models has been conducted. A dedicated effort to examine the structure and data requirements of current models will determine the suitability of models to estimate encounter rates and collision risks of fish with tidal turbines, detail differences among models, and characterize data requirements for model parameterization and input.

Current encounter/collision models are only useful if the structure and assumptions of a model fit biological conditions at a marine energy site, and that the data needed to parameterize and estimate encounter or collision risk can be collected at appropriate spatiotemporal resolutions. The utility of a

model to estimate encounter or collision risk can be evaluated using a suite of metrics to compare model predictions to empirical data. One challenge of this approach is to identify a set of metrics that can be calculated from both empirical data and model output and then compared. This approach has been used to compare agent or individual based model (IBM) output to walleye pollock (*Gadus chalcogramma*) early life history data from the Gulf of Alaska (Hinckley et al. 2016), to evaluate classes of regression models in their ability to describe, detect, and predict biological change at MHK tidal turbine sites (Linder et al. 2017, Linder and Horne 2018), and to compare model fish trajectory predictions to acoustic-based fish tracks at a turbine site (Grippe et al. 2017).

This review examines encounter rate and collision risk models to: identify potential models for use in evaluating encounter collision probabilities with MHK devices; evaluate candidate model structure, assumptions and data requirements for encounter/collision risk predictions; and select candidate models or propose a new model for parameterization and validation. The review will also include descriptions of deficiencies in model assumptions and suggestions for instrumentation and sampling designs for empirical data collections. In the proposed validation step⁴, empirical data streams collected at PNNL's Marine & Coastal Research Laboratory (MCRL) will be used to parameterize candidate model(s) and predict encounter rates and/or collision probabilities with an instream turbine. The output of this exercise will include a summary of model efficacy to quantify encounter/collision risk. It is envisioned that these efforts will result in the submission of a journal review paper that summarizes results and recommends approaches to evaluate encounter/collision risk (*sensu* Horne and Jacques 2018) for individual and populations of marine animals at tidal turbine sites.

It is important to note that definitions of encounter and collision have varied among publications. As an example, Wilson et al. (2006) distinguish encounter from collision by defining the collision rate as the encounter rate discounted by the probability of avoidance and evasion. This definition was adopted by Band et al. (2016) but the term encounter was changed to collision, "because 'encounter' could be interpreted as an animal coming close to the device but without actual contact whereas 'collision' better reflects the potential for actual physical contact between the device and the animal that is the aim of the prediction." (pg. 2, Band et al. 2016). Collisions between an aquatic animal and a device are analogous to interactions of ship's bows or keels of vessels with marine mammals (e.g. Gende et al. 2011). In this report, encounter will be separated from collision for the model review with the term avoidance associated with potential animal-device encounters and evasion associated with potential animal-device collisions. Definitions are provided below.

6.2.2 Approach

If encounter rate and/or collision risk models use empirical data for parameterization or estimation, then it is critical to evaluate model assumptions, spatial and temporal resolution of calculations, parameterization, input data requirements, and model outputs. To effectively use encounter or collision risk models, it is critical that the resolution of empirical data measurements enables prediction of potential interactions of marine animals with tidal turbines. Three classes of interactions are included: avoidance, evasion, and collision. Avoidance is defined as a change in trajectory to prevent an encounter with a turbine. Evasion is a change in trajectory to prevent contact with or strike from stationary or moving parts of a turbine. Collision or strike is defined as physical contact with any part of a turbine.

Overall, two steps will be used in this evaluation: model review and model validation. The model validation step is not part of this report. Models reviewed will include those developed for tidal turbine applications. Models included in the review fit in one of two categories: statistical probability models, or

⁴ This step did not occur due to the change in data collection location and timing.

agent-based/ Individual Based Models (IBMs). Statistical probability models may resolve collision risk for individuals or populations while IBMs use trajectories of individuals to estimate group risks or encounter/collision rates. The perspective or data indexing of models will be Eulerian (i.e., grid), Lagrangian (i.e., particle flow), or a combination of the two. After the model suitability review, one or more models will be proposed as candidates for assessment of encounter/collision risk between marine animals and instream turbines.

6.2.3 Model Review

A group of seven models in two categories that were developed for or relevant to aquatic animal - turbine encounter/collision applications were reviewed (Table 6). For each model a set of attributes including: target animal, assumptions, spatiotemporal resolution, parameters and variables, input data requirements, and model outputs are listed. The goal of the review is to compare and contrast model characteristics to determine one or more candidate models that can be used to define empirical data collection, model validation, and recommendation of sensor characteristics for empirical data collection. The 5 probability models use animal densities for risk calculations. How animal density is used differs among models. In all cases, assumptions are made on animal approaches to a device, and may or may not include behavior that may lead to avoidance or evasion of a device. Among the Agent/IBM models, Goodwin et al. (2014) determines the effects of flow fields on individual fish around a turbine, while Grippo et al. (2017) use a Eulerian-Lagrangian Agent Method (ELAM) model that adds fish behavior rules when an animal nears a turbine.

Table 6: Group of 8 models used to estimate encounter rates and/or collision risk between fish and tidal turbines.

Name	Author	Type	Objective
Statistical/Probability Models			
	Band et al 2016	Collision Risk/Mortality	Harbor seal collision/mortality rates
Exposure Time Population Model (ETPM)	Grant et al. 2014.	Collision Risk	Seabird collision risk
	Hammar et al. 2015	Collision Risk Population	Fish collision risk
	Shen et al. 2016	Encounter Probability	Fish encounter risk
	Wilson et al. 2006	Encounter Risk Population	Mammal, fish collision risk
Agent or Individual Based Models			
Eulerian Lagrangian Agent Method (ELAM)	Goodwin et al. 2014	Passage model	Fish passage through hydroelectric dams
Eulerian Lagrangian Agent Method (ELAM)	Grippo et al. 2017	Encounter/Passage model	Fish encounter rate
	Romero-Gomez and Richmond 2014	Blade strike	Fish collision risk/mortality rates

Inputs to Lagrangian agent or IBMs use trajectories of individuals, which differs from data required by statistical, density-based models. For IBMs, individual animal trajectories, often derived from acoustic tags, are needed prior to, at, and after encountering a turbine. Hydrodynamics, turbine structure, and turbine operational characteristics are needed to accurately describe the environment, fish trajectories, and potential interactions with turbine components. One challenge when comparing statistical probability to IBM models is finding an equivalent for density in IBMs. This challenge is evident when collecting empirical data as low numbers of fish used to in acoustic tag studies to track individuals around turbines will not be representative of the number of fish in an aggregation nor the number of animals in a stock or population. Estimates of avoidance, evasion, and passage rates are necessarily 'scaled' when estimating encounter and collision risk of a stock or population.

6.2.4 Model Evaluation

Characteristics of each collision/encounter model are summarized in Table 7. Among the statistical/probability models, four were developed using fish as the focal animal, with the others focusing on marine mammals (Wilson et al. 2006; Band et al. 2016), or seabirds (Grant et al. 2014). The Hammar et al. (2015) model is a generic model that is able to scale from impacts on an individual animal to impacts on a population. The Band CRM model has been considered the most flexible (Band et al. 2016) compared to the SRSL Encounter Rate Model of Wilson et al. (2006) and has been modified since its original conception (see Table 1, Band et al. 2016). Assumptions of the models spanned a range of no knowledge of turbine presence (Band et al. 2016) to avoidance and evasion of the turbine (Shen et al. 2016) during an encounter. Model spatial resolution was much more explicit in the Agent or Individual Based Models compared to the statistical/probability models. As expected, data input requirements for model parameterization were dependent on model structure. Generally, statistical/probabilistic models require data on animal densities within defined depth ranges and turbine blade speeds, while agent/IBM models require water flow speeds over tidal cycles. Model outputs include encounter probabilities or collision risks.

Table 7: Statistical/probability and agent/individual based model characterization.

Statistical/Probability Models									
Model	Author	Type	Target	Assumptions	Resolution	Parameters Needed	Input	Output	Comments
Modified Band Collision Risk Model (CRM)	Band et al. 2016	Collision Risk/Mortality	Harbor seal	No knowledge of turbine presence		Number of transits through area, probability of collision	Mean operational turbine speed, mean speed of approach to turbine, multiplier for avoidance, seal length	Collision probability at ratios of transit, then mean over radius to get risk of collision	No avoidance or evasion. Considered a flexible model
Exposure Time Population Model (ETPM)	Grant et al. 2014	Collision Risk	Seabird	Collision rate = prob of collision, constant. Collision rate low relative to pop size. No downstream mortality effects (i.e. replacement sampling)		number of deaths as a function of population size collision rate, and exposure time	'acceptable mortality rate' population demographic data	collision rate	Collision risk not modeled but collision rate associated with mortality rate in population is estimated. Determines prob of pop decline at mortality level rather than mortality from collisions
	Hammar et al. 2015	Collision Risk Population	Fish	population size is a function of demographics and movements	population model one hour time step for annual estimate	Fault tree analysis empirical measures of fish activity and current speed	avoidance, co-occurrence collision, blade strike/injury, evasion	turbine mortality, population reduction	Model structure includes many components but no data available for model validation

				all events have binary out-comes					
	Shen et al. 2016	Encounter Probability	Fish	fish within device-depth avoidance upstream evasion near-field		p1 month, diel condition, tide stage			
SRSI Encounter Rate Model	Wilson et al. 2006	Encounter Risk Population	Mammal, fish			Local population density, cross-sectional area of blades, mean speed of blades relative to animal speed			No avoidance or evasion

(cont'd). Statistical/probability and agent/individual based model characterization.

Agent or Individual Based Models									
Model	Author	Type	Target	Assumptions	Resolution	Parameters Needed	Input	Output	Comments
Eularian Lagrangian Agent Method (ELAM)	Goodwin et al. 29014	Passage Model	Fish hydroelectric dams		5 m flow resolution				
	Grippo et al. 2017	Encounter/Passage model IBM + hydrodynamic	Fish	Data and scenarios reflect behavior and causal stimuli overlay of empirical and model match fish behavior in actual conditions fish density as an index of avoidance fish behavior rules are realistic	5 m flow resolution near, 20 m flow resolution far	flow speeds over tidal cycle, drag coefficients of turbine	fish density as a function of distance from turbine fish tracks hydrodynamic output of flow and passive particles	relationship between fish tracks and distance to turbine under different states	noise measurements (frequency spectra and amplitude) of turbine as a function of distance away
	Romero-Gomez and Richmond (2014)	Passage/Encounter model Kinematic model	Fish	no fish avoidance probability of impact function of fish length swimming speed, and blade rotation speed		computational fluid dynamics turbulence simulation	Lagrangian particle trajectories	fish passage survival rates	realistic flow regimes but no fish behavior component

				injury function matched con- ventional hydro- power					
--	--	--	--	--	--	--	--	--	--

6.2.5 Recommended Candidate Model(s)

After review of existing encounter/collision models developed for marine energy applications, one of the existing models, Hammar et al. (2015), includes all components of an aquatic animal (e.g. seabird, fish, mammal) encountering and navigating through a tidal turbine and/or site. This is a good candidate model but there was no model validation included in the study. There remains a need for additional development and parameterization of encounter/collision models.

As an additional approach, potential encounter/collision between an aquatic animal and a tidal turbine can be divided into two components (entrainment, impact), each containing a series of steps with two or more possible outcomes at each step (Figure 51). A combination of animal locomotion and water flux may direct an animal toward a device. If the device is perceived, then the animal may change their trajectory to avoid the device volume (i.e., escape). If the original trajectory is maintained, then the animal will be entrained in the device with the possibility of evading or coming in contact with one or more static or dynamic parts of the device. Contact with the device may lead to no effect, injury, or fatality of the animal. The fatality of the animal may or may not impact the viability of the population or exceed the regulatory ‘takes’ of that species as defined in the Federal Energy Regulatory Commission (FERC) operating permit for that site.

6.2.5.1 Entrainment – Impact Model Description

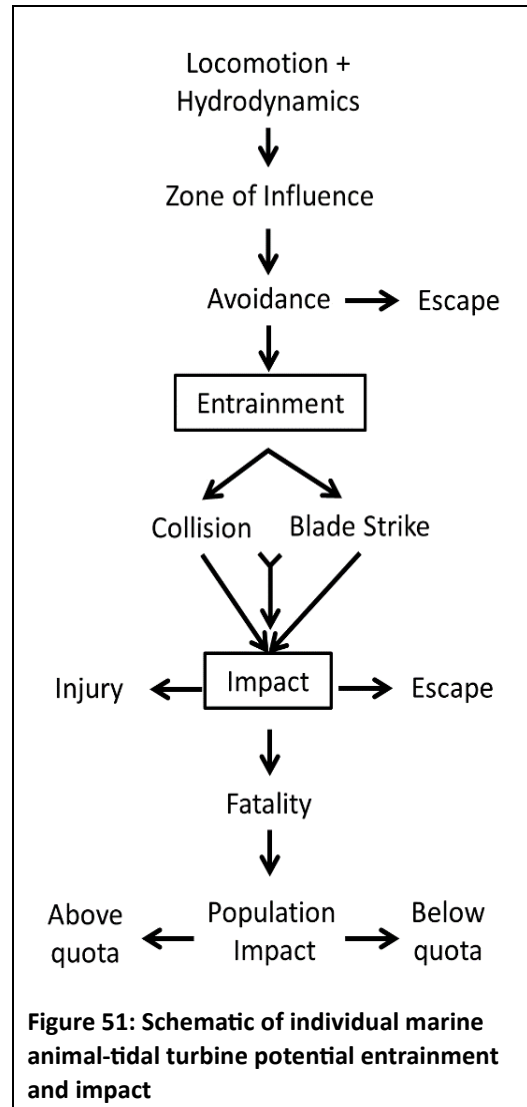
Entrainment is defined as the drawing in of a marine vertebrate animal (i.e., mammal, fish, sea bird) to a marine energy converter (i.e., tidal turbine, wave energy converter). The model is formulated using fish and tidal turbines as a case study but can be adapted to any marine vertebrate and device. Occurrence of an entrainment is a function of the animal being within the device’s zone of influence and the ability of an animal to avoid the device. The zone of influence is the three-dimensional volume that affects interaction between the animal and the device. Avoidance is defined as a change in an animal’s trajectory to prevent entrainment with the device.

The impact of a marine energy converter on a marine vertebrate animal results from a physical interaction (i.e., collision) with any part of a device and/or a strike from a moving component (e.g., turbine blade) of a device. Impact outcomes range from no effect (i.e., evasion) to injury or mortality of the animal. Impacts are dependent on the animal being entrained within the device.

The probability of entrainment is described as

$$P(E) = [P(z) \times P(1 - a|z)]$$

where



- $P(\text{entrainment}) = P(E) = f(\text{zone of influence, avoidance})$;
- $P(\text{impact}) = P(I) = f(\text{zone of influence, collision, strike})$;
- $P(\text{zone of influence}) = P(z) = f(\text{depth zone, device shape and size, tidal current speed})$ this is passive locomotion component; and
- $P(\text{avoidance}) = P(a) = f(\text{perception distance, animal size (swimming ability), flow speed})$ this is active locomotion component.

Note that for conditional probability, this is an addition rule with no interaction term ($A+B - A\&B$).

Entrainment is getting drawn into the device. The probability of entrainment will cycle with device size and shape, and tidal flow. The entrainment model component assumptions are:

- Assumes that passive entrainment is equal for all animals or constant for any length class of animal;
- Assumes that avoidance is conditional on being within device zone of influence;
- Assumes that the zone of influence is specific to any device and location but changes over tidal cycle; and
- Probability of entrainment is calculated for a single instance at a single device; does not include commercial arrays where avoidance options may be reduced; probability of avoidance may change with changes in light, turbidity, or flow.

The probability of impact is described as

$$P(I) = [P(E) \times P(c|E)] + [P(E) \times P(s|E)] - [P(c|E) \times P(s|E) \times P(s|c, E)]$$

where

- $P(\text{collision}) = P(c)$; and
- $P(\text{strike}) = P(s)$.

Note that the multiplication rule within conditional terms and addition rule with interaction term. Representing the interaction term is a challenge.

Impact is defined as the passage through a device. The values of impact range from 0 to 1 where a probability value of 0 is no collision and/or strike (i.e., evasion), and a probability value of 1 is a collision and/or strike with stationary or moving components of the device. An alternate formulation of this model is possible where the probability of an injury through mortality component could be explicitly added to this model where a probability of 0 is no impact, probability values greater than 0 results in an injury, and a probability of 1 results in mortality. There is no time lag effect included for a delayed mortality resulting from an injury. A threshold also needs to be determined where the probability of impact transitions from an injury leads to mortality. This value may be less than 1.

The impact model component assumptions are:

- An impact is conditional on an entrainment (i.e., encounter probability > 0);
- An impact probability > 0 includes at least one collision or strike (could be multiple occurrences but do multiple occurrences require explicit inclusion in the interaction terms?);
- That collision and strike are not mutually exclusive;
- A positive impact value includes only collision and strike; and
- The probability of impact ranges from 0 to 1 where 0 is evasion (i.e. no contact).

6.2.5.2 Defining a Zone of Influence

A turbine zone of influence is the three-dimensional volume that influences the interaction between the animal and the turbine. It includes at least the volume of the device and can extend to the height and width (or radius) of the reactionary distance⁵ of the animal and/or the distance where water flow entrains a non-swimming animal (i.e., passive locomotion) in a device, whichever is greater. Upstream of a turbine, the zone of influence can be represented by a two dimensional plane of the same dimensions at a distance equal to the animal reactionary distance or the turbine entrainment distance, whichever is greater. This volume dimension or planar radius will shrink and expand through a tidal cycle and will depend on current speed and animal swimming ability.

The zone of influence will depend on

- device (shape, size): sphere/circle or cube/rectangle (volume/plane); dimensions of device (radial, rectangular)
- water velocity (site bathymetry, tide state)

and avoidance of a device will depend on:

- reaction distance to the device
- fish swimming ability (species, length): Okubo (1987) relationship will provide swimming speed as a function of animal length: $Locomotion V_{loc} = 2.69 L^{0.86}$. A general passive locomotion value is also available for fish relative to water velocity $V_{fi} = 0.168 \text{ cm s}^{-1.17}$ (Okubo 1971)

To complete entrainment probability estimates, there needs to be a zone of influence assumption: is it just the outer dimensions of the device or something larger? The role of water flow has to be included in the assumption(s).

As an example, device shapes and sizes can be characterized using single or combinations of geometric shapes (Figure 52) to include the support structure and operational section of a turbine.

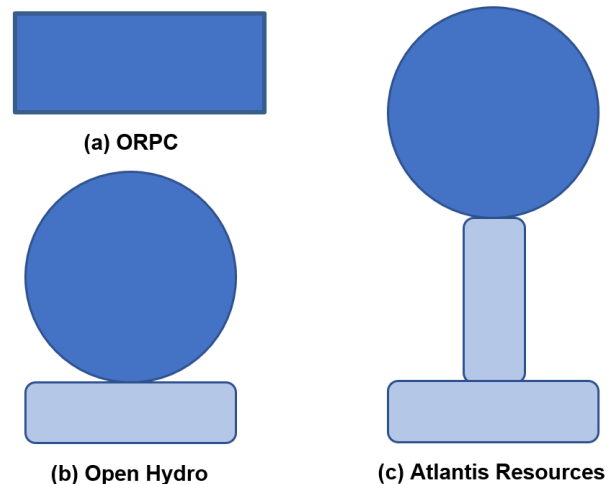


Figure 52: Geometric representations of tidal turbines with moving (dark blue) and stationary (light blue) components.

⁵ Determination of animal reaction distance could be a project in itself. The predator-prey interaction and/or traditional hydropower literature are logical places to begin a review, but what is the discount rate of reaction distance as a function of body length? Also, what is the decrease in entrainment distance with body length? Both are expected to be non-linear remembering Okubo's body length and swimming speed equation (see below).

6.2.5.3 *Potential Animal Encounter - Interaction Outcomes*

There is a range of potential outcomes when an aquatic animal encounters and interacts with a tidal turbine. These outcomes can be divided within the device's zone of influence and when an animal is entrained in a device.

Within Zone of Influence

- If fish length (speed) > flow speed, then avoid device
- If fish length (speed) = flow speed, then possible avoidance of device
- If fish length (speed) < flow speed, then entrainment within device

Within Device

- *Evasion*: no physical contact with device, resulting from a combination of passive and active locomotion
- *Collision*: no impact, injury, mortality
- *Strike*: no impact, injury, mortality

Combinations of collisions and/or strikes are also possible.

6.2.5.4 *Additional Model Products*

Given the diversity of tidal turbine shapes and sizes, a map of entrainment probability isolines as a function of current velocity that will radiate from the center of a device could be used to determine the zone of influence of any device or device component.

6.2.6 Data Streams

There is a series of data streams that are needed to parameterize the Hammar et al. (2015) and the proposed entrainment/impact model. All of these data streams can be collected at the PNNL MCRL in association with tidal turbine deployment and environmental monitoring. Additional deployment and sample resolution considerations will have to be finalized to ensure accurate parameterization of the model. Desired data streams are identified for each component of the model along with suggested sampling instrument(s) in parentheses.

Entrainment

Zone of Influence:

- dimensions of device
- flow speed in front of device through tidal cycle (ADCP)

Avoidance:

- species composition and length distributions of animals likely to encounter device
- density and trajectories of animals approaching and leaving device. Ideally monitor zone of influence, within reaction distance (echosounder, acoustic tags)

Impact

Collision:

- monitor front of device at or parallel to face (optics, imaging sonar)

Strike:

- monitor front of device at or parallel to face (optics, imaging sonar)
- monitor back of device at or parallel to face (optics, imaging sonar)

6.2.7 Characteristics of Recommended Instruments

The critical characteristic of any recommended instrumentation category is that measurement resolution of each instrument matches and is relevant to aquatic animal swimming speeds and water velocities through a tidal cycle. Cruising speeds of fish range from approximately 0.8 to 1 body length per second. For a 30 cm fish, this translates to a maximum cruising speed of 0.3 ms⁻¹. Current speeds at tidal turbine sites range from 0 ms⁻¹ to 5 ms⁻¹ or more (e.g., Bay of Fundy). Acoustic pulse rates and optical frame rates are needed to resolve the trajectories of animals toward devices and potential interactions of animals with devices. If an animal acts as a passive particle with water flow, animal velocities could average 2.5 to 3 ms⁻¹. Ideally, sample acquisition will match these speeds – 2.5 to 3 Hz when animals are present. Additional conditions on optical and acoustic camera instruments would require that images can be used to identify species and possibly measure lengths of animals within the field of view.

6.3 Statistical Encounter-Impact Probability Model (Milestone 10.4.2)

6.3.1 Model Description

The encounter-impact model computes probabilities for individual model components, and conditional probabilities of fish approaching and potentially interacting with a tidal turbine in sequential steps (Figure 53).

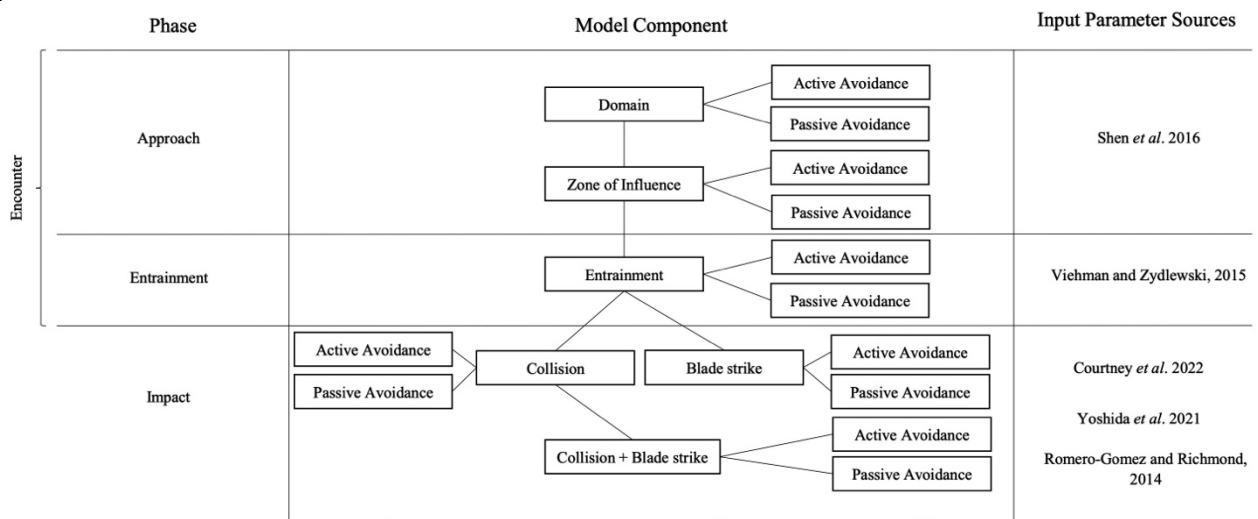


Figure 53: A schematic of the statistical encounter-impact probability model. The left column identifies the model phase, the center column details model components, and the right column identifies literature used to extract parameter values that are used in corresponding model components.

The approach phase quantifies when an animal enters the vicinity of a marine energy converter and includes the model domain, zone of influence, and estimates of active and passive avoidance. The model domain is defined as the study region encompassing the population of interest. If fish are present, then the domain model component is assigned a probability value of 1 (Table 8). We define the zone of influence as the region in which an animal is capable of sensing and reacting to the turbine. Shen *et al.* (2016) used mobile hydroacoustics to track fish approaching a cross-flow tidal turbine and observed responses to a turbine by fish, measured using change in swimming direction, at distances over a hundred meters (m). In this model, the zone of influence is set to this 140 m distance upstream from a tidal turbine (Figure 54). A vertical height of 25 m above the seafloor is used to represent approximately twice the vertical footprint of a proposed turbine in Admiralty Inlet (Jacques, 2014) and is within Shen *et al.*'s (2016) range of water depths (25 m at low tide to 32 m at high tide) at their study site. The

probability of being within the zone of influence is dependent on the device's shape and size, water depth, range of tidal current speeds, and fish swimming speed. The probability of being in the zone of influence is defined as the probability of a fish being within the domain multiplied by the complement of an individual avoiding the device (Table 8).

Table 8: Probability equations for each component of the encounter-impact model.

Model component	Probability equation
Domain	$P(\text{Domain}) = [1, 0]$
Zone of Influence	$P(\text{Zone of Influence}) = 1 * P(1 - \text{Avoid})$
Entrainment	$P(\text{Entrainment}) = P(\text{Zone of Influence}) * P(1 - \text{Avoid} \mid \text{Zone of Influence})$
Collision	$P(\text{Collision}) = P(\text{Entrainment}) * P(\text{Collision} \mid \text{Entrainment})$
Blade strike	$P(\text{Blade strike}) = P(\text{Entrainment}) * P(\text{Blade strike} \mid \text{Entrainment})$
Collision and Blade strike	$P(\text{Collision and Blade strike}) = P(\text{Entrainment}) * [P(\text{Collision}) * P(\text{Blade strike} \mid \text{Collision})]$
Overall Impact	$P(\text{Overall Impact}) = \{1 * P(1 - \text{Avoid}) * [P(\text{Zone of Influence}) * P(1 - \text{Avoid} \mid \text{Zone of Influence})] * [P(\text{Entrainment}) * P(\text{Collision} \mid \text{Entrainment})]\}$ $+ \{1 * P(1 - \text{Avoid}) * [P(\text{Zone of Influence}) * P(1 - \text{Avoid} \mid \text{Zone of Influence})] * [P(\text{Entrainment}) * P(\text{Blade strike} \mid \text{Entrainment})]\}$ $+ \{1 * P(1 - \text{Avoid}) * [P(\text{Zone of Influence}) * P(1 - \text{Avoid} \mid \text{Zone of Influence})] * [P(\text{Entrainment}) * (P(\text{Collision}) * P(\text{Blade strike} \mid \text{Collision}))]\}$ <p><i>Simplified:</i> $P(\text{Overall Impact}) = P(\text{Collision}) + P(\text{Blade strike}) + P(\text{Collision and Blade strike})$</p>

Entrainment occurs when a fish is within the area adjacent to the device, normal to the device face. If an animal continues its current trajectory with no avoidance, it will collide with the turbine base or be struck by a turbine blade. The turbine base and entry area are half the vertical height of the turbine (Figure 54). Areal dimensions of the cross-flow turbine base (i.e., vertical-axis turbines that rotate blades perpendicular to tidal flow direction) and turbine entrance are both 30 m by 10 m. Areal dimensions of the axial-flow turbine base (i.e., horizontal-axis turbines that rotate blades facing direction of flow) and turbine entrance are 5 m by 10 m. The probability of entrainment is defined as the probability of a fish being within the zone of influence multiplied by the probability of 1 minus avoiding the device given that the individual is within the zone of influence (Table 8).



Figure 54. A two-dimensional schematic showing dimensions of the encounter-impact model components for (A) axial and (B) cross-flow turbines.

Interactions between a fish and a tidal turbine are composed of collisions and/or blade strikes. We define collision as physical contact between an animal and the turbine base or a non-moving device component (e.g., Müller et al., 2023). We define blade strike as contact between an animal and a rotating blade (e.g., Castro-Santos and Haro, 2015; Courtney et al., 2022). In the model, collision and blade strike are treated as potential sequential events, where fish can collide with a turbine support structure and then be struck by a rotating blade. This might be an untrivial interaction as turbine dimensions can exceed 15 to 20 m in length and width (c.f. Courtney et al., 2022; Shen et al., 2016; Viehman and Zydlewski, 2015), which provides large surface areas for fish to collide with a turbine base or non-rotating structures when active avoidance is not possible.

Impact is defined as one or more interactions between a fish and a turbine through collision and/or blade strike. Blade strikes constitute the greatest risk to fish and are a concern among researchers and regulators (Copping et al., 2020b). Therefore, most experimental (Yoshida et al., 2020, 2021) and field (Courtney et al., 2022) research has been done to quantify blade strike rates. Impact probabilities are calculated for each model subcomponent and overall potential impact (Table 8) based on field (Courtney et al., 2022), laboratory (Yoshida et al., 2020, 2021), and simulation model (Romero-Gomez and

Richmond, 2014) blade strike data. All impact probabilities depend on whether an animal is present within the entrainment area. The probability of collision with a turbine is calculated as the probability of entrainment multiplied by the probability of collision given that a fish is entrained. The probability of blade strike is defined as the probability of entrainment multiplied by the probability of a blade strike given that a fish has entered the device. Lastly, the probability of collision and blade strike is defined as the probability of entrainment, multiplied by the probability of collision, multiplied by the probability of blade strike given that a fish collided with the device. The overall probability of impact is calculated as the sum of the three potential interaction events: collision, blade strike, and collision and blade strike.

All phases of the encounter-impact model include active and passive avoidance (Figure 53). Avoidance is defined as a change in a fish's trajectory in response to tidal devices. In behavioral studies, fish have been shown to actively avoid predation and navigate around obstacles, even at long distances (e.g., Bender et al., 2023). Tidal flow speeds often surpass fish swimming capabilities (c.f. Okubo, 1987, He, 1993), potentially leading to passive transport through the water and passage around or through tidal turbines. Therefore, the definition of avoidance is expanded to a fish's response and movement away from a device and/or its avoidance due to hydrodynamic forces (Copping and Hemery, 2020). We define the threshold between active and passive avoidance using the ratio of swimming capability to tidal flow. Average Pacific herring (*Clupea pallasii*) fork length from Admiralty Inlet net samples is used to estimate swimming speed using Okubo's (1987) locomotion equation:

$$SS = 2.69 \cdot L^{0.86} \quad (6.1)$$

where SS is swimming speed (ms^{-1}), and L is fish length (m). Active locomotion is assumed when the ratio of swimming speed to tidal flow is greater than 1 body length per second (bls^{-1}) (He, 1993). Passive locomotion occurs when the tidal speed exceeds 1 bls^{-1} , in this study 0.155 ms^{-1} .

6.3.2 Tidal Turbine Dimensions

For this study, representative axial and cross-flow tidal turbines are used in calculations of encounter and impact probabilities. Tidal turbine dimensions used are based on an axial-flow Verdant Power Kinetic Hydropower System (KHPS) (Bevelhimer et al., 2017) (Figure 54A) and a cross-flow Ocean Renewable Power Company TidGen Power System (Shen et al., 2016) (Figure 54B). Verdant Power KHPS turbine characteristics include a three-bladed, single-rotor turbine. The height of the device is approximately 10 m, with a rotor-swept area of 5 m in diameter, defining an area of 5 m by 10 m. The TidGen device is 31.2 m long and 9.5 m high with foils (i.e., rotating blades) 6.7 - 9.5 m above the seafloor, defining an area of 30 m by 10 m.

6.3.3 Empirical Data Description

Data were previously collected for the potential deployment of two Open Hydro turbines in northerly Admiralty Inlet, Puget Sound, Washington, a proposed tidal energy site in the Snohomish Public Utility District (Horne et al., 2013). The proposed site is approximately 750 m off Admiralty Head at a depth of 55 m mean tide level. Data sources included a 120 kHz Simrad EK-60 echosounder on a mobile surface vessel an autonomous bottom-deployed 1 MHz Nortek AWAC acoustic doppler current profiler (ADCP), and midwater trawls conducted by the vessel.

The mobile echosounder operated from May 2 to May 13 and June 3 to June 14, 2011, day and night, where collected data were from 324 parallel transects that were 0.7 to 1.5 km long and 0.5 km apart, extending northwest and southeast of the proposed turbine location (see Horne et al., 2013 for survey details). The ADCP was used concurrently with the mobile echosounder to obtain tide state (slack, moderate, or extreme; flood, ebb) and tidal velocity measurements. The ADCP was deployed May 9-10,

2011, and retrieved June 9-10, 2011, and sampled for 12 minutes every two hours, resulting in 10% coverage of the entire deployment time (Jacques, 2014).

A Marinovich midwater trawl, a 6 m x 6 m box trawl fished with 4.6 m x 6.5 m steel V-doors, was used to capture samples to quantify species composition and length-frequencies of the fish community. Among captured species, Pacific herring was the most abundant species, comprising 32% of the total catch by number. Therefore, in this study, all acoustic backscatter is attributed to Pacific herring in acoustic density calculations. The average length of Pacific herring caught in the midwater trawl was 0.155 m and is used in all acoustic and swimming speed calculations. Given analogous fish lengths and time of year, the target strength conversion equation for Pacific herring from Thomas *et al.* (2002): $26.2 \cdot \log_{10}(L_{cm}) - 72.5$ is used to transform acoustic-derived densities ($m^2 m^{-3}$) to fish densities (fish m^{-2}).

6.3.4 Factors Contributing to Model Component Probabilities

No turbine was deployed during data collection. Instead, the Admiralty Inlet dataset is used to explore possible impacts of multiple turbine types on different fish densities and distributions under different light regimes. To observe how acoustic densities varied with light, probabilities of fish presence for each model component during day and night are calculated for each turbine type. Fish densities are estimated by dividing each surveyed transect in horizontal 140 m, 30 m, or 5 m bins (corresponding to turbine type, Figure 54A, B) and then grouping bins to match the size of each model component.

Probability estimates in the encounter-impact model are also influenced by active and passive avoidance. The model uses three avoidance scenarios. The first scenario assumes fish are unable to avoid the turbine. In the second scenario, fish can avoid the turbine using active and passive avoidance. Active avoidance rates are estimated from the Admiralty Inlet dataset by multiplying the proportion (i.e., 0.372, Shen *et al.*, 2016) of fish who avoid model components and the turbine. Passive avoidance rates are estimated by tabulating fish observations swimming around or above model components, assuming avoidance will occur to the side or above a device. The proportion of time passive avoidance occurs is determined by the tidal cycle – when tidal flow speeds surpass fish swimming speeds. The third scenario uses Shen *et al.*'s (2016) active avoidance rate of 0.372 without incorporating passive avoidance. When an avoidance rate from Admiralty Inlet or Shen *et al.* (2016) is incorporated into the model, estimates of fish impact are calculated using conditional probabilities from sequential model components. This approach evaluates a fish's ability to avoid a device across model components and provides insight into the likelihood of impact for each model phase and overall encounters with tidal turbines. When an avoidance rate is not included, calculated impact probabilities are not dependent on sequential model components and analogous to rates in published studies.

6.3.5 Estimating Statistical Probabilities

Probabilities of fish presence during day and night is determined by enumerating acoustic abundance estimates detected within bins along each mobile survey transect, aligned with areas of each model component (Figure 54A, B). To obtain fish presence probabilities, acoustic density was derived in Echoview 12 (<https://echoview.com>) based on the factors and avoidance scenarios described. Acoustic energy was extracted by setting cell grids of 140 m by 25 m for the zone of influence, and 30 m by 10 m or 5 m by 10 m for the entrainment area along each transect. This energy, known as the area backscattering coefficient (Simmonds and MacLennan, 2005), can be converted to obtain density estimates of Pacific herring. Density of Pacific herring is calculated as the product of the area backscattering coefficient and model component areas divided by the backscattering cross-section (Simmonds and MacLennan, 2005). The backscattering cross-section is $7.39 \times 10^{-5} m^2$ in its linear form, obtained from the target strength equation $26.2 \cdot \log_{10}(L_{cm}) - 72.5$ (Thomas *et al.*, 2002) using the average

Pacific herring length of 0.155 m (Horne et al., 2013). Fish abundances in cells are summed to estimate total abundance for each transect. Probabilities of individual fish presence within each model component are determined by dividing the number of individuals detected within each cell of each model component by total fish abundance.

Since no data on fish-turbine interactions are available from Admiralty Inlet, encounter and impact published values are used in model calculations. At this time, there are no published probability estimates of collisions between fish and stationary tidal structures or collisions followed by blade strikes. Collision probabilities are estimated by calculating the complement of published blade strike probabilities and discounting by length-dependent swimming speed and time of day avoidance rates published in Viehman and Zydlewski (2015). Blade strike probabilities are taken from field measurements (Courtney et al., 2022), laboratory experiments (Yoshida et al., 2021), and calculated using a blade-strike model (Romero-Gomez and Richmond, 2014):

$$P(\text{strike}) = \frac{nNL \cos(\alpha)}{U} \quad (6.2)$$

where $P(\text{strike})$ is the probability of a blade strike, n is the number of blades, N is a fixed rotation rate [i.e., 0.357 s^{-1} for a cross-flow turbine (Viehman and Zydlewski, 2015) and 0.667 s^{-1} for an axial-flow turbine (Bevelhimer et al., 2017)], L is fish length (m), α represents the fish approach angle perpendicular to the blade plane ($\alpha = 0$), and U is tidal velocity (ms^{-1}). Blade strike probabilities are estimated using equation (6.2) for tidal velocities observed in Admiralty Inlet that ranged from 1.0 ms^{-1} to 3.0 ms^{-1} (Horne et al., 2013) in increments of 0.2 ms^{-1} . Incremental changes in tidal velocities depict the progression of a tidal cycle, yielding a range of strike probabilities in response to periodic flow conditions. The encounter-impact model also uses blade strike rates from Courtney *et al.* (2022) (0.13) and Yoshida *et al.* (2021) (0.02 – 0.05) in blade strike calculations. Inclusion of these rates in the blade strike model component compensates for limited data availability and introduces a range of probability estimates that incorporate turbine design, time of day, and turbine avoidance.

The sequential probability of collision and blade strike is determined by multiplying collision and published blade strike probability estimates. Probabilities of collision, blade strike, and collision and blade strike are reduced by avoidance rates in model calculations. Overall impact probabilities are calculated by summing estimated probabilities of each impact subcomponent (Table 8).

6.3.6 Results

Probabilities for each component of the encounter-impact model are influenced by turbine type, time of day, and avoidance. Based on their vertical distribution in Admiralty Inlet, approximately 6.36 to 6.49% of Pacific herring (hereafter fish) would be swept into zone of influence (Tables A1.1, A1.2, A1.3, A1.4). If fish are within the zone of influence, 0.245 to 4.08% of those individuals are likely to be entrained with the device for an axial-flow turbine (Tables A1.1, A1.2) and 1.18 to 4.08% of individuals for a cross-flow turbine (Tables A1.3, A1.4). If entrained, probabilities of impact depend on events of collision, blade strike, or sequential collision and blade strike. About 0.0364 to 32.4% of fish that are entrained with the device will collide with both turbine types, and approximately 0.0261 to 40% of fish will be struck by the turbine's blades (Tables A1.1, A1.2, A1.3, A1.4). If both events occur, about 0.000242 to 6.78% of fish might collide then be struck by either turbine type's blade (Tables A1.1, A1.2, A1.3, A1.4). Overall, approximately 0.110 to 66.6% of fish will be impacted by an axial-flow turbine and 0.110 to 68.9% of fish will be impacted by a cross-flow turbine (Table 9).

Table 9: Impact probability estimates for axial and cross-flow turbines for avoidance scenarios using alternate blade strike probability estimates.

Avoidance scenario	Blade strike probability estimate	Axial-Flow Turbine		Cross-Flow Turbine	
		Day	Night	Day	Night
No avoidance	Courtney <i>et al.</i> 2022	0.172	0.455	0.172	0.455
	Yoshida <i>et al.</i> 2021	0.0928	0.353	0.0928	0.353
	Romero-Gomez and Richmond, 2014	0.436 - 0.175	0.666 - 0.171	0.337 - 0.138	0.689 - 0.423
Admiralty Inlet avoidance	Courtney <i>et al.</i> 2022	0.00204	0.00541	0.00204	0.00541
	Yoshida <i>et al.</i> 2021	0.00110	0.00419	0.00110	0.00419
	Romero-Gomez and Richmond, 2014	0.00515 - 0.00206	0.00805 - 0.00545	0.00907 - 0.00191	0.0176 - 0.00529
Shen <i>et al.</i> (2016) avoidance	Courtney <i>et al.</i> 2022	0.00687	0.0185	0.00687	0.0185
	Yoshida <i>et al.</i> 2021	0.00370	0.0144	0.00370	0.0143
	Romero-Gomez and Richmond, 2014	0.0164 - 0.00699	0.0276 - 0.0187	0.0304 - 0.00647	0.0357 - 0.0181

When comparing probabilities, about 0.194 to 10% fish are likely to interact with model components and the turbine at night than during the day for both turbine types (Tables A1.1, A1.2, A1.3, A1.4). However, blade strikes are more likely to occur during day than at night, with an average 0.24% difference for the axial and cross-flow turbine (Tables A1.1, A1.2, A1.3, A1.4). When comparing overall impact probabilities in light regimes, fish are more likely to interact with the device at night than during the day for both turbine types, with estimates ranging over three orders of magnitude (Table 9). Impact probabilities vary within three orders of magnitude depending on other parameters applied to the model. Turbine design/size influences impact probabilities, with an axial-flow turbine exhibiting the lowest risk of impact across factors and avoidance scenarios (Table 9).

As expected, fish are more likely to encounter each model component when no avoidance is included, where model components are not conditioned on preceding events in calculations (Tables A1.1, A1.2, A1.3, A1.4). Probabilities are lowest when the proportion of fish in Admiralty Inlet was not in the vertical range of model components or turbine, reflecting the inclusion of conditional probabilities in model calculations. The vertical distribution of fish within the zone of influence across all avoidance scenarios is the same for both turbine types (Tables A1.1, A1.2, A1.3, A1.4). Fish are more likely to be entrained with the device when Shen et al.'s (2016) avoidance rate (4.08% of herring) is applied to the model for both turbine types (Tables A1.2, A1.4). Probabilities of impact are highest by two to three orders of magnitude when no avoidance is included for a cross-flow turbine (Table 9). Collision probabilities (32.4% of herring), blade strike probabilities (40% of herring), and sequential collision and blade strike probabilities (6.78% of herring) are all highest for both turbine types when subcomponents are modeled with no avoidance (Tables A1.1, A1.2, A1.3, A1.4). Minimum and maximum probability values are similar between subcomponents and overall impact estimates, with larger values occurring when no avoidance is applied and lowest when avoidance rates from Admiralty Inlet are used in model calculations (Table 9). Conditional probability estimates from this study are both lower and higher than other published values (Table 10). Shen et al. (2016) and Bangle et al. (2022) observed order of magnitude higher probabilities of fish approach and encounter with a tidal turbine than average approach estimates in this study. Similarly, Viehman and Zydlewski (2015) and Bevelhimer et al. (2017) found that approximately 18.8 and 15.4% of fish are directly aligned with a tidal device. Band et al. (2016) observed order of magnitude higher probabilities of collision for Harbor seals (*Phoca vitulina*) with turbine rotors when compared to results of this study. In contrast, Wilson et al.'s (2006) non-conditional encounter probabilities for Pacific herring are two orders of magnitude lower than those estimated in this study.

Regardless of the combination of factors, a minimum of 0.00242 to a maximum of 32.4% of fish will encounter or interact with a tidal turbine. Additionally, 0.110 to 68.9% of fish will potentially collide, be struck, or collide and then be struck by a tidal turbine. Probability values are particularly low when conditioned on fish occurring within a turbine's zone of influence, where subsequent entrainment may lead to an impact. All highest probability values occur at night with no avoidance in calculations for a cross-flow turbine.

Table 10: Comparison of average fish presence probabilities for each phase of the encounter-impact model to published literature values.

Encounter-Impact Model Phase	Encounter-Impact Model Probabilities		Literature Model Phase	Literature Results		Literature Source	Literature Focal Species
Approach	Day	Night		Day	Night	Shen <i>et al.</i> 2016	Unidentified
	0.0636	0.0649		0.432			
Entrainment				0.15 – 0.4		Bangley <i>et al.</i> 2022	Striped bass
	0.0200	0.0203		0.0432	0.333	Viehman and Zydlewski, 2015	Unidentified
Collision	0.0200	0.0203	Collision	0.154		Bevelhimer <i>et al.</i> 2017	Unidentified
	0.0126	0.0982		0.306		Band <i>et al.</i> 2016	Harbor seal
Blade strike	0.0567	0.0543	Encounter	0.000212		Wilson <i>et al.</i> 2006	Pacific herring
Collision and Blade strike	0.00243	0.0126	Encounter	0.000363		Wilson <i>et al.</i> 2006	Harbor porpoise

6.3.7 Discussion

Probabilities of fish presence within Admiralty Inlet and potential interaction with the tidal turbine are influenced by model component, time of day, turbine type, and avoidance scenario. Across all model components including overall impact, estimates of fish-turbine encounters and impacts are generally low, spanning one to four orders of magnitude. Impact probabilities are particularly low when conditioned on fish being within the zone of influence susceptible to entrainment by the device. Conditional events are crucial in understanding a fish's approach to a turbine situated hundreds of meters away and how fish can actively or passively avoid the device to prevent a potential interaction. Influence of light and dark cycles on the vertical distribution of fish and impact probabilities is limited. Differences based on diel cycles are potentially driven by changes in herring vertical distribution (Munk *et al.*, 1989), where a slight increase in probability values is observed for model estimates based on empirical data obtained at night compared to day. Studies in the field (Viehman *et al.*, 2015; Viehman and Zydlewski, 2015; Williamson *et al.*, 2019) and laboratory experiments (Yoshida *et al.*, 2021) indicate that light intensity affects fish distribution in the presence of MRE devices. Williamson *et al.* (2019) noted a 2.63 times greater increase in fish aggregation rates around turbine structures at night compared to day, supporting previous findings that indicate higher probabilities of turbine entry for fish at night (Viehman and Zydlewski, 2015). Viehman *et al.* (2015) reported that fish are more evenly distributed at night, highlighting fish presence in dark conditions where turbines are present. Results from our study and current literature suggest that analyzing fish behavior in light and dark conditions can provide insights into fish-turbine detection distances and potential interactions.

Fish approaching and encountering tidal turbines at various distances are observed in controlled field (e.g., Courtney et al., 2022; Hammar et al., 2013) and laboratory flume-study experiments (e.g., Amaral et al., 2015; Bevelhimer et al., 2019; Castro-Santos and Haro, 2015; Yoshida et al., 2020, 2021). Although valuable, these studies are constrained in their assessment of fish approach due to limitations in their experimental designs such as relying on short time-based trials and sensor capabilities. In the natural environment, Shen et al. (2016) found evidence suggesting that a fish's initial opportunity to avoid tidal turbines occurs at approximately 140 m during flood tide. In our model, the zone of influence represents this 140 m range in which fish can detect and respond to a turbine and predicts whether a fish's approach will result in a close fish-turbine interaction or avoidance behavior. Recent research also highlights interactions at closer distances, with several studies suggesting that fish exhibit evasive behaviors (e.g., Hammar et al., 2013; Viehman and Zydlewski, 2015). Our model identifies entrainment as the fish-turbine encounter area, which is dependent on turbine size and archetype. Estimates of fish presence within the entrainment component in Admiralty Inlet are lower than those within the zone of influence, indicating fish avoidance as they transition from one area to the other. As an analogy, studies by Bevelhimer et al. (2017) and Viehman and Zydlewski (2015) used DIDSON acoustic cameras (Belcher et al., 2002) to capture interactions between fish and turbines. Bevelhimer et al. (2017) monitored fish interactions with an axial-flow turbine for over 20 days in East River, NY, finding evidence that 12.5% of fish adjusted their swimming direction and velocity when approaching the operating turbine. Similarly, Viehman and Zydlewski (2015) employed two DIDSON cameras to observe fish behavior around a cross-flow turbine, where 15.5% of fish schools avoided the device by passing above, below, or through the turbine (Viehman and Zydlewski, 2015).

The impact phase of the model includes subevents of collision, blade strike, and collision and blade strike. Probabilities of fish-turbine interaction assuming no avoidance predict higher estimates than scenarios where avoidance is considered. Analogous studies found impact probabilities in models with no avoidance (e.g., Wilson et al., 2006) result in higher values by one to two orders of magnitude compared to our model predictions that include avoidance. In our model, Yoshida et al.'s (2021) fish-turbine blade strike probabilities predict lower impact estimates when combined with an avoidance scenario. Yoshida et al.'s (2021) lower probability values are attributed to a slower turbine blade rotational speed to fish swimming speed ratio, resulting in greater avoidance and lower blade strike rates. In contrast, our model predicts higher blade strike estimates when coupled with Romero-Gomez and Richmond's (2014) blade strike model that does not include fish avoidance. After review, our range of impact estimates demonstrate that avoidance is an important factor influencing potential interactions, both as a scenario within the model and experimentally with fish and a turbine present.

Admiralty Inlet offers dynamic tidal channels favorable for tidal energy development. While we had some field data from Admiralty Inlet, at the time of data collection there were no tidal turbines deployed in Admiralty Inlet. Fish density data used in probability calculations lack information on fish-turbine interactions, necessitating the use of published avoidance and blade strike values. Use of published literature supports conditional probability values which are calculated using empirical acoustic transect data along sequential steps. The data serve as a series of spatiotemporal snapshots of fish distributions but do not explicitly include individual fish trajectories as they pass through a model domain. Although Admiralty Inlet boasts a diverse species composition, Pacific herring was the primary focus of this study because of their dominant representation within the trawl catch data (Horne et al., 2013). Representing a mixed fish community by a single species in the conversion of acoustic backscatter measurements to density and abundance estimates is potentially biased, but biases in the data are assumed constant. Pacific herring are used to represent pelagic, schooling fish that are common constituents of any fish

community at a tidal energy site. The model's adaptability allows for examination of culturally significant fish species in the region, acknowledging that other marine species, such as marine mammals, may raise regulatory concerns (Copping and Hemery, 2020). Nevertheless, estimating impact probabilities for Pacific herring in Admiralty Inlet emphasizes utilization of acoustic data and highlights existing data gaps that must be addressed to obtain accurate statistical-based encounter-impact probabilities.

Numerical modeling is a tool used to quantify information gaps and estimate uncertainties to contribute to additional research and monitoring (Buenau et al., 2022). However, models are still affected by lack of information available to accurately validate potential interactions. The construction of the encounter-impact model consists of a combination of empirical data from Admiralty Inlet and literature values. To obtain probability estimates that are validated, ideally, the entire structure of the model should be parameterized with empirical data obtained from the field with a tidal turbine device present. The potential risk of an individual colliding with a stationary component of a device or colliding then being struck by a turbine blade has not been studied in field or laboratory-based research. This area of direct, potential impacts should be prioritized when developing future fish-turbine monitoring studies as it can be labeled a likely interaction for larger marine energy structures. The current model also lacks additional possibilities of impact that should be considered, such as hydraulic shear stress (Cada et al., 2007) and barotrauma (Brown et al., 2012), noting that both of these drivers are significantly amplified for hydropower turbines relative to tidal turbines. Flume studies are one opportunity to examine hydraulic conditions when fish are entrained with the turbine, yet it can be difficult to monitor whether fish would have an immediate effect from the turbine itself or flume hydraulics (Castro-Santos and Haro, 2015). Our model does not consider the possibility of what might happen to a fish after it has interacted with a turbine in the form of a collision and/or blade strike. Effects from impact might include fish injury, mortality, or population displacement (Copping et al., 2021, 2023). Fish mortality and population displacement can be labeled as delayed impacts, where long-term effects of fish-turbine interactions are not observed immediately. Broadening knowledge of these direct and delayed impacts is a crucial first step in environmental assessment, especially when estimating interactions between individual species with a single device (Copping et al., 2023).

Moving forward with data collection, model adaptation, application, and validation to estimate potential impacts, we must consider factors that can contribute to high-risk estimates. Probabilities of encounter and impact are highest at night (e.g., Viehman and Zydlewski, 2015; Williamson et al., 2019). Turbine design is another factor that contributes to higher probability estimates of impact. A turbine with greater dimensions, like the approximately 30 m by 10 m TidGen cross-flow turbine (Shen et al., 2016), has a greater chance for fish to interact with the device. Compared to the dimensions of the Verdant Power KHPS axial-flow turbine (Bevelhimer et al., 2017) used in this study, a cross-flow turbine is six times larger than an axial-flow turbine. The empirical data estimates show higher probabilities of entrainment and collision for the cross-flow turbine, most likely due to the amount of space the device is taking in the water column. Ultimately, when collecting empirical data on animal-turbine interactions, results of this study support monitoring potential impacts for day and night continuously, as well as the two different types of turbine structure. By considering these different factors, data collection will entail a more inclusive outlook of empirically-based encounters and impacts.

6.4 Agent-based Encounter-Impact Simulation Model (Milestone 10.4.3)

6.4.1 Model Framework

The encounter-impact, agent-based simulation computes probabilities of fish approaching and potentially interacting with model spatial components and two different tidal turbine types in a three-

dimensional environment over time (Figure 53; Figure 54A, B). Within the model domain, the dimension parallel to tidal flow (x-axis) is 400 meters (m) (i.e., approximately double the length of model components and turbine), the horizontal dimension orthogonal to the tidal flow (y-axis) is set at 100 m, and water depth (z-axis) is set at 55 m (which is analogous to the tidal turbine site at Admiralty Inlet, WA, USA; Horne et al., 2013) (Figure 3). Other than the turbine, model spatial volumes have no influence on fish trajectories and are only used in tabulating fish presence for probability calculations. Periodic boundary conditions define a cyclic state of flow across boundary surfaces and are applied along the y-axis where fish can enter at one end of the y-axis and exit at the other end. Periodic boundary conditions are not applied to the x- or z-axes. The x-axis allows fish to exit either end of the domain without re-entering the environment. The z-axis (i.e., the top and bottom boundaries of the domain) uses reflective boundary conditions to prevent fish from exiting the environment. Fish that encounter these boundaries are reflected back into the domain at the same incident angle resulting in retention within the simulated volume.

6.4.1.1 Spatial Environment

The model includes unidirectional tidal flow in the positive x-direction, where velocities range from 0 to 3.0 ms^{-1} (as observed at Admiralty Inlet, WA, USA; Horne et al., 2013) (Figure 55). Tidal velocities from 0 to 0.25 ms^{-1} do not restrict fish active locomotion, which allow fish to swim in all directions with little influence from tidal flow. Tidal velocities exceeding 0.25 ms^{-1} represent passive locomotion, or drifting, where current flow exceeds maximum fish swimming speed. A tidal flow of 0 ms^{-1} enables fish to move independently of the water. The model characterizes a full tidal cycle, but probability calculations exclude negative tidal velocities (i.e., where flow direction moves right to left) since a negative flow exceeding 0.25 ms^{-1} prevents fish from encountering the turbine. Within the model, results from the second half of a tidal cycle (i.e., negative tidal velocities with fish swimming right to left) will parallel those in the positive direction.

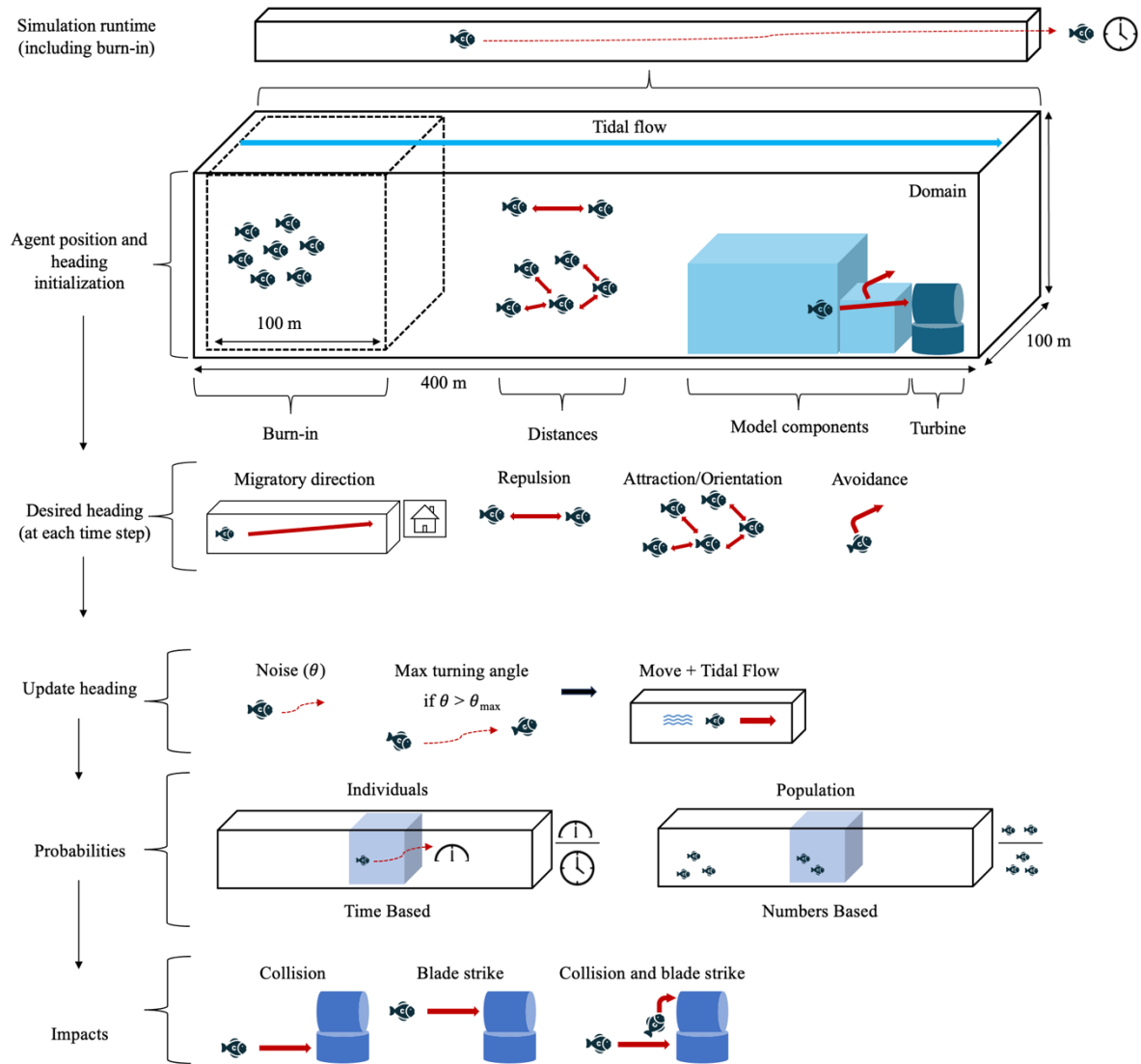


Figure 55: A schematic of the overall agent-based model structure including domain size, agent initialization, agent behavior, computation of probability estimates, and types of potential impacts.

6.4.1.2 Tidal Turbines within the Spatial Environment

Three-dimensional footprints of representative axial and cross-flow tidal turbines are modeled in this study. Axial-flow turbine dimensions are based on the Verdant Power Kinetic Hydropower System (Bevelhimer et al., 2017), while cross-flow turbine dimensions are based on the Ocean Renewable Power Company TidGen Power System (Shen et al., 2016). For the axial-flow turbine, the turbine base is modeled as a cylinder with a height and a radius of 5 m. The upper portion is also cylindrical, with the same 5 m height and radius to match the turbine base but oriented horizontally (y -axis) with the circular ends pointing to the left and right (see example in Figure 55). The cross-flow turbine is also modeled with both the base and the upper portion as cylinders. The base has a height of 15 m and a radius of 10 m, while the blade radius height is 10 m to match the turbine base. Turbine placement in the model is adjacent to the entrainment model component volume at approximately (x -375, y -50, z -0) on the right side of the environment.

6.4.1.3 Fish and Migration

Pacific herring (*Clupea pallasii*, hereafter herring) undergo annual feeding and spawning migrations and form aggregations through their annual movement cycle (Huse et al., 2002). Misund (1993) collected data from a multi-beam acoustic sonar and found that herring tend to swim alongside others of similar body lengths and in shallow waters up to 60 m deep. Agents (i.e., individual fish) within the simulation are modeled to reflect herring behavior and physiology. Assigned traits and rule-based behaviors govern agent interactions with their neighbors and the environment. Consequently, fixed parameters chosen in Table 11 reflect herring behavior and school size.

Table 11: Fixed parameter values and experimental factors for the agent-based, encounter-impact model.

Parameter	Value
Migratory direction weight	0.2 ± 0.04
Repulsion distance (m)	2 ± 0.4
Attraction distance (m)	15 ± 3
Alignment distance (m)	10 ± 2
Attraction and alignment weight	0.2 ± 0.04
Avoidance strength, k	-0.1 ± 0.02
Maximum turn angle (radians)	0.8 ± 0.16
Turn noise scale (radians)	0.01 ± 0.002
Swimming speed (bls^{-1})	1

Within the model domain, herring swimming direction is influenced by a migratory direction, with a preferred bearing (Bernardi and Scianna, 2020) in the positive x-direction. Migratory direction is the highest behavioral priority among all behavioral components in the model (Figure 55), influencing the net direction of individual fish. Equation (6.3) defines the migratory direction of an individual fish, indexed by i , at each time step $t + 1$:

$$\text{Direction}_{\text{migratory}_i}(t + 1) = \text{Direction}_{\text{migratory}_i}(t) + \alpha \cdot (1, 0, 0) \quad (6.3)$$

where migratory direction is based on the fish's current direction at its current time step t , modified by a weight parameter, $\alpha = 0.2$ (Table 11), that determines the change in direction in the positive x-direction (Couzin et al., 2005). The weight parameter, α , is multiplied by $(1, 0, 0)$, which is a unit vector in three-dimensional space where 1 indicates its magnitude in the x-direction and 0 indicates no magnitude in the y- and z-directions.

6.4.1.4 Fish Social Interactions

Herring movement is based on the zonal schooling model described in Couzin et al. (2002, 2005). Aggregation behavior incorporates repulsion, attraction, and alignment forces within specified radii of each fish (Reynolds, 1987). Among these three forces fish to fish repulsion is prioritized, where each individual fish, with the position of each fish indexed by i , maintains a separation from their neighbors, whose positions are indexed by j , within a zone of repulsion. The repulsion force minimizes collisions among individuals (Figure 56). Equation (6.4) defines a normalized repulsion vector for each fish based on surrounding neighbor within the repulsion zone at each time step t :

$$\text{Repulsion}_i(t+1) = \sum_{j \neq i} \frac{-(\text{position}_i - \text{position}_j)}{\|\text{position}_i - \text{position}_j\|} \quad (6.4)$$

where the total repulsion force for each fish is the sum of individual repulsion forces from each neighbor within the repulsion zone. Attraction and alignment forces govern how fish move as a cohesive group (Aoki, 1982). The attraction force is the inclination of fish to move towards each other, and the alignment force orients their direction of movement with nearby neighbors (Figure 56). To determine the strength of attraction and alignment forces, a weighted attraction and alignment term, ω , is used to balance the two forces, where a value of 1 equals maximum attraction and a value of 0 denotes maximum alignment (Couzin et al., 2005). Equation (6.5) summarizes the combined influence of attraction and alignment forces:

$$\text{Attraction \& Alignment}_i(t+1) = \sum_{j \neq i} \omega \cdot \frac{(\text{position}_i - \text{position}_j)}{\|\text{position}_i - \text{position}_j\|} + (1 - \omega) \cdot \frac{(\text{heading}_j)}{\|\text{heading}_j\|} \quad (6.5)$$

where a normalized attraction vector and normalized alignment vector (i.e., heading direction) is calculated for each neighbor. The total force on each fish i at each time step t is the sum of individual attraction and alignment vectors from each neighbor within the zone of attraction and zone of alignment, with a weighted term, $\omega = 0.2$ (Table 11), set to match tight herring schooling formations that are often disc-shaped and spherical (Misund, 1993). The resultant schooling force governing the direction of fish at time $t+1$ is the total of all forces at the current time step t :

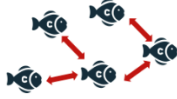
$$\text{Schooling}_i(t+1) = [\beta \cdot \text{Attraction \& Alignment}_i(t)] + \text{Repulsion}_i(t) \quad (6.6)$$

where equation (6.6) includes a schooling parameter, β , ranging from 0 to 1, which influences the degree of schooling behavior. A value of 0 signifies asocial behavior (individuals act independently) and a value of 1 denotes a stronger tendency towards attraction and alignment forces.

$$\text{Repulsion}_i(t+1) = \sum_{j \neq i} \frac{-(\text{position}_i - \text{position}_j)}{\|\text{position}_i - \text{position}_j\|}$$



$$\text{Attraction \& Alignment}_i(t+1) = \sum_{j \neq i} \omega \cdot \frac{(\text{position}_i - \text{position}_j)}{\|\text{position}_i - \text{position}_j\|} + (1 - \omega) \cdot \frac{(\text{heading}_j)}{\|\text{heading}_j\|}$$



$$\text{Avoidance}_{i, \text{turbine}}(t+1) = \begin{cases} 0 & \text{if distance} > 140 \\ e^{-\frac{\text{distance}}{k}} & \text{if distance} \leq 140 \end{cases}$$



Figure 56: Schooling behavior including a migratory direction, noise and maximum turning angle equations, and turbine avoidance equations.

6.4.1.5 Fish Avoidance Behavior

Turbine avoidance by fish is defined as a change in a fish's trajectory in response to tidal devices (Bender et al., 2023; Hammar et al., 2013). Active avoidance involves fish swimming to evade model components or the turbine. Passive avoidance occurs as fish drift through model components or the turbine, where trajectories are influenced by tidal speed. Initiation of fish-turbine active avoidance at each time step t occurs at distances less than 140 m (c.f., Shen et al. 2016), with an amplitude inversely proportional to the distance between a fish, indexed by i , and the turbine's base or blade (Figure 56). Equation (6.7) models fish avoidance behavior as an exponential decay function relative to the distance from a turbine:

$$\text{Avoidance}_{i, \text{turbine}}(t+1) = \begin{cases} 0 & \text{if distance} > 140 \\ e^{-\frac{\text{distance}}{k}} & \text{if distance} \leq 140 \end{cases} \quad (6.7)$$

where k is the amplitude of avoidance strength and *distance* is the distance between a fish and the turbine. If the distance between a fish and a turbine exceeds 140 m, then no avoidance behavior occurs.

6.4.1.6 Combining all Behavioral Forces

Updated positions and headings of each fish at time step $t+1$ are determined by combining migratory direction (Eq. 6.3), aggregation (Eq. 6.4-6.5), and avoidance behavior (Eq. 6.7) into a single equation:

$$\begin{aligned} (\text{Position} + \text{Heading})_i(t+1) &= \text{Position}_i(t) + \alpha \cdot (1, 0, 0) + \\ &\sum_{j \neq i} \frac{-(\text{position}_i - \text{position}_j)}{\|\text{position}_i - \text{position}_j\|} + \left[\beta \cdot \left[\sum_{j \neq i} \omega \cdot \frac{(\text{position}_i - \text{position}_j)}{\|\text{position}_i - \text{position}_j\|} + (1 - \omega) \cdot \frac{(\text{heading}_j)}{\|\text{heading}_j\|} \right] \right] \\ &+ \begin{cases} 0 & \text{if distance} > 140 \\ e^{-\frac{\text{distance}}{k}} & \text{if distance} \leq 140 \end{cases} \end{aligned} \quad (6.8)$$

Random noise in positions and headings is introduced at each time step to add variability in individual fish trajectories (Codling et al., 2008; Li et al., 2009) (Figure 3). In equation (3.7), the dot product is used

to calculate the angle difference, $\theta_{\Delta \text{ heading}_i}$, between the fish's current heading at time t and its updated heading at $t + 1$ after incorporating random noise (0.01 radians, Table 11).

$$\theta_{\Delta \text{ heading}_i} = \cos^{-1} \left(\frac{(\text{Heading}_i(t) \cdot (\text{Heading} + \text{Noise})_i(t + 1))}{(|\text{Heading}_i(t)| \cdot |(\text{Heading} + \text{Noise})_i(t + 1)|)} \right) \quad (6.9)$$

To prevent fish from making excessive directional changes at each time step $t + 1$, the maximum turning angle is restricted to 0.8 radians (approximately 45 degrees) (Table 11) (Figure 55). The choice of 0.8 radians is supported by the experimental studies of Domenici and Blake (1997) who found maximum turning angles for pelagic fish ranged between 45 to 50 degrees. Each fish's heading is calculated by comparing the angle between the current and updated headings:

Heading_{*i*} ($t + 1$) =

$$\begin{cases} v(t) \cdot \cos(\theta_{\max}) + \left(\frac{v(t) - (v(t+1) \cdot v(t)) \cdot v(t)}{\|v(t+1) - (v(t+1) \cdot v(t)) \cdot v(t)\|} \right) \cdot \sin(\theta_{\max}) & \text{if } \theta_{\Delta \text{ heading}_i} > \theta_{\max} \\ (\text{Heading} + \text{Noise})_i & \text{else} \end{cases} \quad (6.10)$$

If the desired turning angle exceeds the maximum turn angle, then the fish's heading is adjusted by rotating the initial heading vector, $v(t)$, towards the desired heading vector, $v(t + 1)$ by the maximum allowable angle. If the desired heading is within the allowable range ($\theta \leq \theta_{\max}$), then the desired heading is updated with a degree of randomness, represented by $(\text{Heading} + \text{Noise})_i$ (Eq. 6.10) (Figure 56).

6.4.1.7 Distances between Neighboring Fish and the Tidal Turbine

To determine whether individual fish are interacting with their neighbors and/or a tidal turbine from their current position, we calculate distances between them to find whether we apply behavior forces or turbine avoidance. Fish to neighboring fish distances are computed using the Euclidean distance formula in a three-dimensional space:

$$D_{i,j} = \sqrt{(x_i - x_j)^2 + (y_i - y_j)^2 + (z_i - z_j)^2} \quad (6.11)$$

where $D_{i,j}$ is the calculated distance between an individual fish, i , and a neighboring fish, j (Figure 57). The distance between a fish and the turbine base is calculated using the Euclidean distance formula (Equation 6.11), with $D_{i,turbine}$ being the distance between fish and the turbine base, representing individual fish coordinates at their current position (x_i, y_i, z_i) , and the turbine base at fixed coordinates (375, 50, 5) for an axial-flow turbine and (375, 50, 15) for a cross-flow turbine.

To calculate the distance between a fish and the turbine rotor, we use the center of the turbine's cylindrical face represented by the coordinates $(x_{turbine}, y_{turbine}, z_{turbine})$ (see example of turbine face in Figure 57). This calculation involves two main components: the turbine face distance in the x -direction (Eq. 6.12) and the radial distance in the y - z plane (Eq. 6.13).

$$\text{Turbine face distance} = ||x_i - x_{turbine}|| - \frac{\text{turbine height}}{2} \quad (6.12)$$

$$\text{Radial distance} = (y_i - y_{turbine})^2 + (z_i - z_{turbine})^2 \quad (6.13)$$

$$D_{i,turbine} = \begin{cases} \text{Turbine face distance}, & \text{if radial distance} \leq r \\ \sqrt{(\text{Turbine face distance})^2 + (\text{Radial distance})^2}, & \text{if radial distance} > r \end{cases} \quad (6.14)$$

where r is 5 m for the radius of the axial turbine and 10 m is the radius of the cross-flow turbine. The turbine face distance (Eq. 6.12) is the absolute difference between the fish's and turbine's x -coordinates, adjusted by half the turbine's height. The radial distance (Eq. 6.13) is the squared difference

between the fish's and turbine's y - and z -coordinates. The final distance, $D_{i,turbine}$, is a piecewise function (Eq. 6.14). If the radial distance is less than or equal to the turbine's radius r , the final distance is the turbine face (Eq. 6.12). If the radial distance exceeds r , the final distance is the Euclidean distance combining the turbine face (Eq. 6.12) and radial distances (Eq. 6.13) (Figure 57).

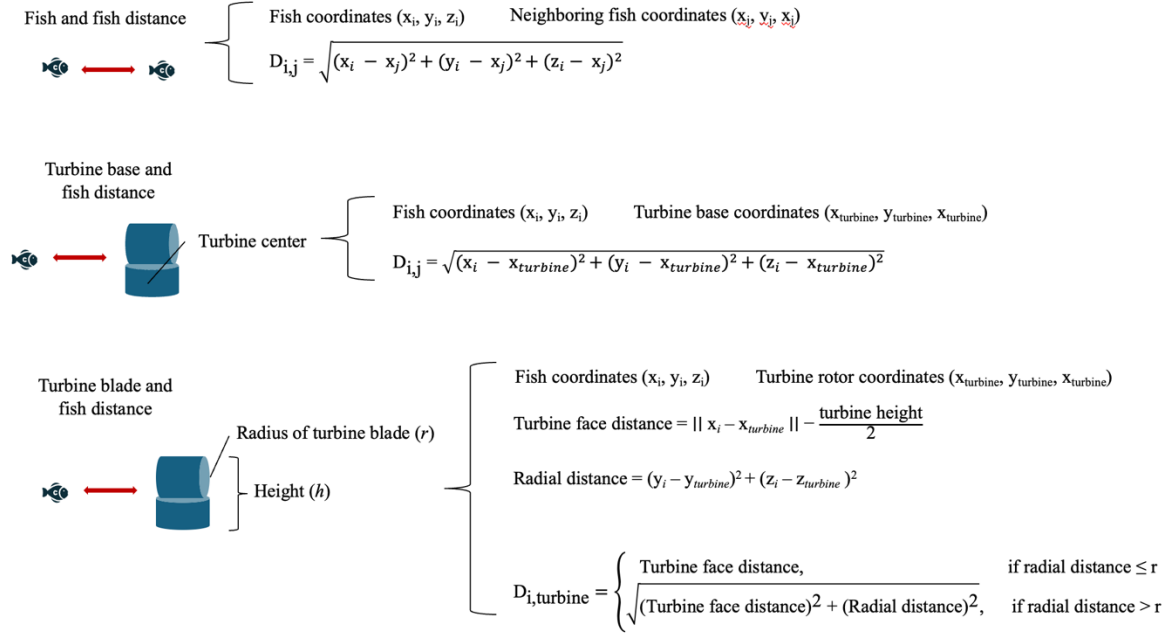


Figure 57: Distance equations between fish and neighboring fish and between fish and turbine structures.

6.4.1.8 Fish movement

Fish movement is characterized by a constant swimming speed of 1 body length per second (He, 1993) (Table 11), which is within the range of fish aerobic swimming. In equation (6.15), fish position and bearing at the next time step, $t + 1$, is based on current position at time t , swimming speed and updated heading at time t , and tidal influence including speed and direction:

$$(\text{Position} + \text{Heading}_i)(t + 1) = \text{Position}_i(t) + [\text{Speed}_i \cdot \text{Heading}_i(t)] + [\text{Tidal speed} \cdot (1,0,0)] \quad (6.15)$$

6.4.1.9 Fish Initialization within the Domain

Fish are initialized in the domain with random starting positions (x_i, y_i, z_i) and orientations $(\theta_{\text{heading}_i})$. The initial numbers of fish aggregations are randomly allocated using a constant density, ρ , and a dimensionless scaling factor, F that determines the number of aggregations:

$$\text{Number of aggregations} = F \cdot \sqrt[3]{\rho} \quad (6.16)$$

At a constant density ρ , a larger F value (e.g., 5) results in more numerous but smaller fish aggregations. Conversely, decreasing the F value (e.g., 2) leads to fewer, yet larger fish aggregations. Fish are initialized in a 55 by 100 by 55 m burn-in volume at the left end of the model domain (Couzin et al., 2005), where fish spend approximately 5% of the total simulation runtime in this volume to swim and form initial schools.

6.4.1.10 End Conditions of Simulation Run

Each simulation is considered an individual run, beginning when fish are initialized within the burn-in volume and ending when all fish in the domain exit the environment from either the right or left side (x -

axis). After the final fish exits the model domain, the total number of time steps is tabulated, and the simulation is restarted for the next run (Figure 3).

6.4.1.11 Data Acquisition from Simulation Runs

Interactions between fish and tidal turbines can include collisions and/or blade strikes (c.f. Section 6.3, Peraza and Horne, 2023) (Figure 55). Within the model, a fish will react to the turbine based on their distance to the device and fish-turbine avoidance (Equation 6.7). If a fish does not evade a device, then a fish can collide with a stationary component of the turbine. Once a collision has occurred, the fish's bearing in the next time step is determined by the vector originating from its current position extending towards the turbine's location, which is used to determine the direction and strength of a rebound at a mirrored incident angle. Blade strikes occur when a fish enters the upper half of the turbine structure, where fish are randomly assigned a probability of being struck or passing through turbine blades. Probabilities of blade strike range from 0.02 (Yoshida et al., 2020, 2021) to 0.13 (Courtney et al., 2022). When a fish enters the turbine rotor-swept area, the number of time steps spent inside this area is tabulated, and individuals are assigned a random probability of escapement. If this probability is less than or equal to 0.11, a blade strike occurs, and then the fish continues their current trajectory. If the probability of escapement is greater than 0.11, then the fish avoids interacting with the turbine blades and passes through.

Probabilities of encounter and impact are computed for individuals within a population, and for all fish in the simulation as a population (Figure 55). Individual probability values are calculated using the time each fish spends in each model component volume and the turbine. Probabilities are determined by counting fish duration (i.e., number of time steps) in each volume component, divided by the duration of the simulation. The total number of time steps varies in each simulation run, as the model runs until the last fish is no longer in the model domain. Fish population probabilities are based on the number of fish that end up in each volume component. These population probability estimates are based on the summation of fish counts in each volume component, divided by the total number of fish in the simulation. Fish-turbine impacts are calculated for the population by dividing fish count occurrences by total fish abundance, where the turbine upper section is the turbine rotor-swept area that results in a blade strike or pass through, and the lower portion of the turbine as a stationary base. In addition to calculating fish presence probabilities for each model component and the turbine (Figure 54), the time individual fish spend within the rotor-swept area and the number of fish entering this area is recorded to assess how quickly fish escape once inside the rotor area. The average amount of time an individual fish spends within each model component and the average proportion of fish in the population who encounter model components is also calculated.

6.4.1.12 Experimental Structure

The simulation can be used to examine the relative importance of different factors influencing animal-turbine interactions (Figure 55). Three experimental factors are analyzed: 1) fish abundance, 2) fish aggregation behavior, and 3) tidal flow speed (Figure 58). To explore how the density of individuals in the model domain influences aggregation and turbine avoidance, a baseline number is set to 328 fish. This number is based on the catch of Pacific herring from 36 mid-water trawls conducted in Admiralty Inlet (Horne et al., 2013). The effect of density change is examined by doubling the value to 656 fish in one set of simulations and halving the value to 164 fish in a second set of simulation runs (Table 11; Figure 55).

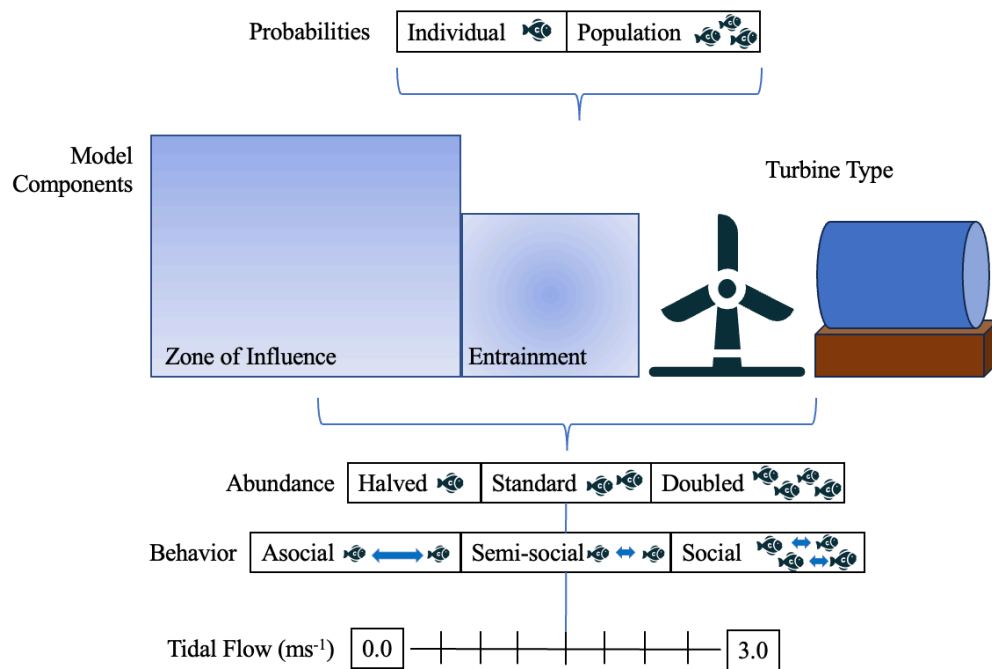


Figure 58: A schematic of the experimental design for simulation runs. Probabilities are computed for individual fish and populations. Probabilities are computed for each model component and turbine design, where the simulation's structure is shaped by component and turbine characteristics. Experimental factors investigated in simulation runs include fish abundance (categorical), aggregation behavior (categorical), and tidal flow (continuous).

Levels of fish social interaction that potentially impact dynamics of fish aggregation and their encounters with the turbine are also examined. The aggregation weight parameter is varied across three levels (0, 0.5, 1) to represent asocial, semi-social, and social fish aggregation behaviors (Table 11; Figure 55). Asocial behavior does not include an attractive force among fish, resulting in independent fish trajectories. The semi-social scenario results in the formation of multiple, small aggregations of fish. The highest level of social behavior includes a rapid formation of a cohesive single aggregation.

The final experimental factor investigated is tidal flow, a factor that determines a fish's ability to swim independent of water motion in a dynamic environment. Tidal speeds are increased by 0.25 ms^{-1} increments from 0 to 1 ms^{-1} to examine fish behavior at slower tidal speeds. Tidal speeds beyond 1 ms^{-1} are increased by 0.5 ms^{-1} to examine fish behavior at higher speeds. This tidal range enables a detailed examination of how incremental increases in flow influences encounter-impact probabilities (see Table 11; Figure 55). Model parameters listed in Table 11 are held constant at their base values, while remaining experimental factors (i.e., abundance, aggregation behavior, flow speed) are systematically varied through each factor level in sets of 1000 simulations.

6.4.1.13 Sensitivity Analysis

The choice of factors and parameter values within an agent-based model can potentially influence the outcome of each simulation run and corresponding metrics derived from simulations. Parameter values that influence fish behavior in the simulation are based on empirical data, literature values, or biological reasoning (e.g. physiological limits) but ultimately are assigned arbitrarily (Table 11). A sensitivity analysis is used to quantify the impact of parameter value choices and the relative magnitude of parameter

effects. Results from a sensitivity analysis can also be used to identify important empirical data streams that are needed to evaluate and validate parameter value choices in simulation models (Frey and Patil, 2002). A local sensitivity analysis (Saltelli, 2004) examines model sensitivity around a set of parameter values, with a $\pm 20\%$ change from an initial value. One parameter is adjusted based on the $\pm 20\%$ change while remaining parameters are set to baseline values (Table 11). Sensitivity analyses simulations are run 1000 times for each $\pm 20\%$ parameter change. Probabilities for each parameter change are expressed as a 95% confidence interval, where results are presented as the percent change deviation from the lower and upper confidence bounds (Saltelli, 2008).

6.4.1.14 Analysis Between Statistical and Simulation Model

A comparison of results between the statistical and agent-based modeling approaches enables an examination of the structure of the encounter-impact model (Figure 53). The statistical model uses animal density and distribution data along with published blade strike values but does not incorporate population fish-turbine interactions or avoidance. To compare probability estimates, average probabilities, based on their respective sample sizes, are tabulated by model type (i.e., statistical or simulation), model component (e.g., zone of influence, entrainment), and turbine type (i.e., axial-flow, cross-flow).

Following the calculation of average encounter-impact probabilities from the simulation model, a non-parametric Wilcoxon T-test (Wilcoxon, 1945) is used to compare the means of paired groups. In this case, the mean probabilities are compared for each model component and each model type.

6.4.2 Results

Probability of occurrences are obtained for individuals and populations of fish organized by model component, turbine design, fish abundance, aggregation behavior, and tidal flow (Figure 58). As expected, based on the dimensions of model components (Figure 53), more fish enter the zone of influence than any other model component, with up to 40% of fish entering this zone. A much smaller proportion of fish physically contact the turbine, with collision and blade strike probabilities never surpassing 0.0025 across all model configurations.

6.4.2.1 Effects of Fish Abundance

Varying fish density over a factor of four has no effect on the amount of time individual fish spend within the zone of influence, entrainment, and turbine rotor-swept area model components (Figures A2.1, A2.3, A2.5). Overall, individual fish spend up to 50% of their time within the zone of influence, up to 25% of their time within the entrainment component, and up to 3% of their time within the turbine rotor-swept area (Figures A2.1, A2.3, A2.5).

Similarly, there is no difference in the proportion of the fish population, that interacts with model components across densities. Instead, across all fish abundances, as fish approach each model component their risk of interacting with components or the turbine decreases. Based on the average probabilities in Table 12 and Figures A2.7 and A2.8, fish are more likely to collide with the turbine than be struck by a turbine's blade. Fish populations are also less likely to interact with an axial-flow turbine than a cross-flow turbine among the three fish abundances (Table 12).

Table 12: Summary table of average agent-based, encounter-impact population probability estimates comparing fish abundance.

Fish Population Probabilities			
Fish abundance (number of individuals)	Model Components	Axial-Flow (50 m²)	Cross-Flow (300 m²)
164 fish	Zone of Influence	0.1212	0.3247
	Entrainment	0.07531	0.2382
	Collision	0.0004778	0.01468
	Turbine Rotor Entry	0.0001323	0.02075
	Blade strike	0.00001377	0.002392
	Collision and blade strike	0.000001806	0.0001741
328 fish	Zone of Influence	0.1190	0.3663
	Entrainment	0.07475	0.2588
	Collision	0.0003404	0.01484
	Turbine Rotor Entry	0.0001148	0.03077
	Blade strike	0.00001422	0.003779
	Collision and blade strike	0.000001242	0.0003562
656 fish	Zone of Influence	0.1258	0.3803
	Entrainment	0.08190	0.2700
	Collision	0.0008459	0.009181
	Turbine Rotor Entry	0.0001696	0.03419
	Blade strike	0.00005043	0.004290
	Collision and blade strike	0.000003240	0.0001959

6.4.2.2 Effects of Aggregation Behavior

When comparing effects of aggregation behavior on the amount of time individual fish spend within the zone of influence and the turbine rotor-swept area, asocial fish spend less time (i.e., where individual fish trajectory probabilities are lower) in these areas compared to semi-social and social fish (Figures A2.1, A2.5). However, fish spend the same amount of time within the entrainment model component among the three aggregation behaviors (Figures A2.3).

In cases where fish exhibit social behaviors, a higher proportion of the fish population are more likely to encounter model components or interact with the tidal turbine compared to asocial fish. Under asocial conditions, fish are, on average, 0.045% more likely to collide with an axial-turbine compared to semi-social and social fish. Additionally, asocial fish are 0.3% more likely to collide with a cross-flow turbine than their semi-social and social counterparts (Table 13). Like the comparison of fish densities, asocial and aggregating fish are more likely to interact with a cross-flow turbine than an axial-flow turbine (Table 13).

Table 13: Summary table of average agent-based, encounter-impact population probability estimates comparing fish aggregation behavior.

Fish Population Probabilities			
Aggregation behavior	Model Components	Axial-Flow (50 m²)	Cross-Flow (300 m²)
Asocial behavior	Zone of Influence	0.09312	0.3091
	Entrainment	0.06305	0.2391
	Collision	0.0006238	0.01338
	Turbine Rotor Entry	0.00006063	0.006663
	Blade strike	0.000007452	0.0007498
	Collision and blade strike	0.000001242	0.00005623
Semi-social behavior	Zone of Influence	0.1354	0.3899
	Entrainment	0.08880	0.2551
	Collision	0.00006775	0.009683
	Turbine Rotor Entry	0.0001011	0.03862
	Blade strike	0.00001025	0.004645
	Collision and blade strike	0.0000003871	0.0002873
Social behavior	Zone of Influence	0.1344	0.4060
	Entrainment	0.08221	0.2925
	Collision	0.0003400	0.01169
	Turbine Rotor Entry	0.0002686	0.04860
	Blade strike	0.00002893	0.006225
	Collision and blade strike	0.000002419	0.0003723

6.4.2.3 Effects of Tidal speed Variation

The amount of time fish spend within model components varies proportionally with tidal speed. Periodic tidal conditions significantly influence this interaction, potentially affecting fish exposure to tidal turbines. As tidal speed increases, fish spend less time in the zone of influence and entrainment model components compared to slower tidal speeds (Figures A2.1, A2.3). In contrast, the amount of time fish spend within the turbine rotor-swept area increases as fish transition from active to passive locomotion (Figure A2.5).

As tidal speed increases, the proportion of fish encountering the zone of influence decreases. However, the opposite is true for the entrainment model volume, where the proportion of fish entrained with the turbine increases as tidal speeds increases. The proportion of fish entering the rotor-swept area and/or being impacted by the turbine through collision and/or blade strikes also increases as tidal speed increases. For an axial-flow turbine, impacts of collision, blade strike, and sequential collision and blade strike occur when tidal speeds exceed 0.25, 1, and 1.5 ms⁻¹ respectively. For a cross-flow turbine, impacts of collision, blade strike and sequential collision and blade strike occur when tidal speeds exceed 0, 0.25, and 0.5 ms⁻¹ respectively.

Table 14: Summary table of average agent-based, encounter-impact population probability estimates comparing tidal speeds.

Fish Population Probabilities			
Tidal speed	Model Components	Axial-Flow (50 m²)	Cross-Flow (300 m²)
0 ms ⁻¹	Zone of Influence	0.1272	0.3883
	Entrainment	0.06221	0.1779
	Collision	0.0000003048	0.0008876
	Turbine Rotor Entry	0	0.000001161
	Blade strike	0	0
	Collision and blade strike	0	0
0.25 ms ⁻¹	Zone of Influence	0.1236	0.3767
	Entrainment	0.06896	0.2254
	Collision	0.00002957	0.002252
	Turbine Rotor Entry	0	0.0005078
	Blade strike	0	0.00009581
	Collision and blade strike	0	0.000003484
0.5 ms ⁻¹	Zone of Influence	0.1228	0.3718
	Entrainment	0.07116	0.2463
	Collision	0.00003719	0.004099
	Turbine Rotor Entry	0.0000003048	0.002248
	Blade strike	0	0.0004547
	Collision and blade strike	0	0.00002322
0.75 ms ⁻¹	Zone of Influence	0.1240	0.3701
	Entrainment	0.07789	0.2624
	Collision	0.00005365	0.006835
	Turbine Rotor Entry	0.0000006097	0.01071
	Blade strike	0.0000003048	0.002043
	Collision and blade strike	0	0.0001004
1.0 ms ⁻¹	Zone of Influence	0.1233	0.3676
	Entrainment	0.07946	0.2716
	Collision	0.00007652	0.005218
	Turbine Rotor Entry	0.000002134	0.02162
	Blade strike	0.0000006097	0.003683
	Collision and blade strike	0.0000003048	0.0001768
1.5 ms ⁻¹	Zone of Influence	0.1240	0.3635
	Entrainment	0.08450	0.2833
	Collision	0.0002435	0.01466
	Turbine Rotor Entry	0.00003963	0.04374
	Blade strike	0.000006097	0.005966
	Collision and blade strike	0.0000009146	0.0003095
2.0 ms ⁻¹	Zone of Influence	0.1199	0.3568
	Entrainment	0.08651	0.2897
	Collision	0.0004530	0.01873

	Turbine Rotor Entry	0.0001564	0.06054
	Blade strike	0.00001737	0.006986
	Collision and blade strike	0.0000009146	0.0004285
2.5 ms ⁻¹	Zone of Influence	0.1205	0.3611
	Entrainment	0.08893	0.2991
	Collision	0.0008902	0.02255
	Turbine Rotor Entry	0.0004158	0.07145
	Blade strike	0.00003932	0.007864
	Collision and blade strike	0.000001829	0.0005476
3.0 ms ⁻¹	Zone of Influence	0.1181	0.3592
	Entrainment	0.08930	0.3043
	Collision	0.001184	0.02501
	Turbine Rotor Entry	0.0007137	0.07081
	Blade strike	0.00007987	0.007766
	Collision and blade strike	0.000008231	0.0005749

6.4.2.4 Sensitivity analysis

A local sensitivity analysis indicates that entrainment is most sensitive model component to parameter value changes compared to all other model components. Entrainment has the greatest range of percent change estimates from the baseline mean, with axial-flow turbines being the most sensitive to parameter value changes (Table 15). Conversely, collision and blade strike probabilities are least sensitive compared to other volume-based model components due to less variability in probability estimates (Figures A2.7, A2.8, A2.9). Percent change for collision from baseline parameter values range from -0.92 to -0.037%, and 0.0054 to 0.99% change for blade strike. For overall impacts, maximum turn angle is the most sensitive parameter influencing the probability of collision for an axial-flow turbine and blade strike for a cross-flow turbine. Avoidance strength is the most sensitive parameter affecting the probability of collision for a cross-flow turbine (Table 15). Sequential collision and blade strike is omitted from the sensitivity analysis as no probabilities of impact were obtained.

Table 15: Percent changes of baseline mean values organized by model component, turbine type, and parameters from a 95% confidence interval for each 20% change. A dash in the columns indicates that a percent change was not quantified.

Model Component	Parameter	Percent Change	
		Δ 20%	Δ 20%
		Axial-Flow	Cross-Flow
Zone of Influence	Max turn angle	0.46	0.23
	Turn noise scale	0.11	0.12
	Avoidance strength	0.34	0.17
	Repulsion distance	0.45	0.21
	Attraction distance	1.44	0.11
	Alignment distance	1.27	0.16
	Desired direction weight	0.31	0.03
	Attraction & alignment weight	0.45	0.25
Entrainment	Max turn angle	5.04	1.29
	Turn noise scale	2.67	1.01
	Avoidance strength	9.40	7.64
	Repulsion distance	5.22	0.88
	Attraction distance	-1.82	-1.03
	Alignment distance	11.40	0.88
	Desired direction weight	7.13	2.60
	Attraction & alignment weight	-4.94	-0.11
Collision	Max turn angle	1.03	0.05
	Turn noise scale	—	0.068
	Avoidance strength	-0.97	0.15
	Repulsion distance	—	0.052
	Attraction distance	—	-0.037
	Alignment distance	—	0.056
	Desired direction weight	—	0.11
	Attraction & alignment weight	-0.92	-0.15
Blade strike	Max turn angle	—	0.99
	Turn noise scale	—	—
	Avoidance strength	—	0.0054
	Repulsion distance	—	—
	Attraction distance	—	—
	Alignment distance	—	—
	Desired direction weight	—	—
	Attraction & alignment weight	—	—

6.4.2.5 Comparison of Statistical Model Results to Agent-based Results

Results from the statistical encounter-impact model are averaged based on model component and turbine type to enable comparison to average simulation encounter-impact results. Analyses from Wilcoxon t-tests (Wilcoxon, 1945) support evidence that the proportion of fish, adjusted for the number of fish in each model type, are different for each model component (Table 16). The greatest differences in average encounter-impact probabilities between the statistical and simulation models occur in the

subcomponents of collision, blade strike, and sequential collision and blade strike. Simulation probabilities are one to four orders of magnitude lower than statistical probabilities. The remainder of model components are within the same order of magnitude across turbine type (Table 16).

Table 16: Comparison of average encounter-impact probabilities between the statistical and simulation-based model. Statistical probability estimates are based on day and night probabilities and avoidance. (*) indicates that averages from the statistical and simulation model are statistically significant.

Encounter-Impact Model Component	Average Statistical Encounter-Impact Probabilities	Average Simulation Encounter-Impact Probabilities	Average Statistical Encounter-Impact Probabilities	Average Simulation Encounter-Impact Probabilities
	Axial-Flow (50 m ²)		Cross-Flow (300 m ²)	
Zone of Influence	0.06425 <i>N</i> = 4988	0.02311* <i>N</i> = 8856000 (12% of fish)	0.06425 <i>N</i> = 4988	0.08163* <i>N</i> = 8856000 (37% of fish)
Entrainment	0.01820 <i>N</i> = 129016	0.001355* <i>N</i> = 8856000 (7.5% of fish)	0.02221 <i>N</i> = 22032	0.01139* <i>N</i> = 8856000 (26% of fish)
Collision	0.05430 <i>N</i> = 48	0.0003404* <i>N</i> = 8856000	0.05654 <i>N</i> = 48	0.01484* <i>N</i> = 8856000
Blade strike	0.06129 <i>N</i> = 48	0.00001422* <i>N</i> = 8856000	0.04984 <i>N</i> = 48	0.003779* <i>N</i> = 8856000
Collision and Blade strike	0.007458 <i>N</i> = 48	0.000001242* <i>N</i> = 8856000	0.007660 <i>N</i> = 48	0.0003562* <i>N</i> = 8856000

6.4.3 Discussion

Probability estimates of fish-turbine encounters and interactions, whether at individual or population levels, are influenced by the intricacies of model components, turbine designs, and experimental variables including fish abundance, aggregation behavior, and tidal flow. In the current model, tidal flow is the most important factor influencing fish-turbine interaction risk. At high tidal speeds, fish will drift into model components more frequently as tidal speed surpasses fish swimming speed. This results in fish potentially colliding with or being struck by turbine blades. Current encounter-impact models often do not include these behavioral or tidal flow conditions; therefore, it is important to include both active and passive avoidance behaviors when developing simulation encounter-impact models, especially since tidal turbine sites are located in high-flow environments (Pelc and Fujita, 2002).

Fish aggregation behavior also plays a fundamental role in how fish potentially encounter and/or interact with tidal turbines. Asocial fish exhibit lower probabilities of collision and/or blade strike compared to their socially-oriented counterparts. When schooling, fish prioritize aligning and fostering cohesion with neighboring individuals until individuals prioritize obstacle (i.e., turbine) avoidance over group formation and maneuvers (Domenici and Batty, 1997). This behavioral pattern is evident during low tidal speeds, where active swimming dictates fish trajectories, without any additional external environmental influences (Marras and Domenici, 2013). Results from the sensitivity analysis indicates that variation in aggregation parameters did not influence the impact component of the model. This suggests that chosen parameter values were robust and not merely artifacts of the model structure. In summary, tidal speed and social aggregation are two factors that heavily influence encounter-impact estimates. It is important

to acknowledge that fish exhibit a wide range of behaviors beyond those simulated in the ABM, and that hydrodynamics are more complex than the tidal flow and direction included in the model. Therefore, the association between tidal flow and aggregation, along with their respective encounter-impact probability estimates, are thought to represent maximum risks when applied to real-world scenarios.

Despite ABMs being a powerful tool that can incorporate empirical data and behavioral rule sets (c.f., Bonabeau, 2002), there are caveats to the interpretation of simulation results that should be addressed. ABMs can become computationally intensive as the number of agents and the complexity of interactions increase. For example, incorporating more complex behavioral and environmental conditions, such as fish predators, wind-induced waves, tides, or eddies, would require significantly more computational power or extended simulation run times. To maximize the efficiency of numerous simulation runs, we concentrated on the influence of social aggregation and tidal flow, to meet the objective of incorporating avoidance and aggregation behaviors in a fish-turbine interaction ABM.

In the context of this study, the lack of empirical data on aggregative and avoidance behaviors of individual fish poses a significant challenge when parameterizing an ABM. To mitigate this challenge, our study used aggregation parameters that mimicked fish movements from previous modeling studies by Couzin et al. (2002, 2005). By selecting parameters that represent herring behavior in our simulations, we found that parameter choices potentially influence encounter-impact probabilities. Results of the sensitivity analysis suggest that probabilities of impact were not artifacts of the model structure nor parameter choice. Impact probabilities exhibited minimal to no change from those estimated using baseline parameter values. Our model primarily focuses on simulating interactions up to collision and blade strike, we do not quantify direct injury, mortality, or any downstream indirect effects. Currently, such data are unavailable, with the exception of Sanderson et al. (2023) who found no evidence of collisions or blade strikes when Atlantic salmon (*Salmo salar*) were examined downstream of a turbine installation. This data limitation restricts our ability to fully assess all impacts stemming from animal-device interactions. Our model also does not include other behaviors such as diel vertical migration (Rossington and Benson, 2020) that could enhance a fish's ability to evade a device at short or long approach distances. Incorporating more intricate behaviors into the simulation could potentially reduce probability estimates, as additional behavioral cues could increase device avoidance (c.f. Copping et al., 2021).

To date, few published marine and avian studies use simulation models to estimate interaction risks between animals and renewable energy devices. Eichhorn et al. (2012) developed an ABM to predict the risk of wind turbine blade and bird interactions based on bird proximity to wind turbines, integrating findings from the CRM (Band, 2006). They found that when 99-99.5% of birds recognize and actively avoid the wind turbine, the maximum annual mortality rate is 0.4 for birds within 1000 m of the device. In a MRE parallel example, Rossington and Benson (2020) developed a quasi-Lagrangian ABM to predict eel-turbine interactions to reproduce turbine rotor and interaction risk estimates from the CRM (Band et al., 2016). They used their ABM to integrate eel swimming speed, animal length, approach direction, and vertical migration scenarios, finding that 0.3-1.1% of eels will interact with the turbine. Variability in their probability estimates is largely dependent on eel swimming and vertical migration behaviors. Despite structural, focal species, and parameter value differences among the two published animal-turbine ABM models and this study, comparing numerical results from each simulation provides insight on how model parameters influence estimates of encounter-interaction risk. For example, Rossington and Benson's (2020) ABM estimated interaction risk to be two orders of magnitude higher than our axial-flow turbine results, but their estimates are similar in order of magnitude to our cross-flow turbine results. This contrast suggests that differences in numerical outcomes may arise among turbine types, although these

differences cannot be clearly separated from potential effects of including fish avoidance and aggregation behaviors in the current encounter-impact ABM.

A key insight gathered from our study is the comparison between results from the statistical model (q.v. Section 6.3) and the simulation model. For the zone of influence and entrainment model components, spatial occupancy is within the same order of magnitude in both models, despite the Wilcoxon t-test (Wilcoxon, 1945) indicating that the means differ between the two sets of probabilities. In contrast, probabilities of overall impacts (i.e., collision, blade strike, collision and blade strike) differ by orders of magnitude among model and turbine types/sizes. For both turbine designs, overall impact statistical estimates are calculated using conditional probabilities of fish-turbine interactions and published literature values (e.g., Courtney et al., 2022; Romero-Gomez and Richmond, 2014; Yoshida et al., 2021) due to the lack of information on fish-turbine interactions in the Admiralty Inlet dataset. While overall impact simulation probabilities also incorporate literature-based probabilities, the simulation contains a tidal device with probabilities of turbine rotor passage or blade strike. Turbine rotor passage is an additional factor in the agent-based model, which results in lower overall blade strike and sequential collision and blade strike probabilities compared to the statistical model (c.f. Viehman and Zydlewski, 2015). The integration of spatial occupancy data and conditional probabilities from literature sources highlights significant differences in probability estimates of encounter and impact between the statistical and simulation models, emphasizing the importance of model selection in accurately assessing fish-turbine interaction risks.

A conceptual encounter-impact model was developed to serve as a framework for this and future modeling efforts using either a statistical or simulation approach. Potential improvements to the current simulation model could incorporate additional behaviors such as fish responses to light and turbine noise and expanding the model's scope to include more complex environmental characteristics (e.g., eddies, water levels, salinity) that may influence fish behaviors. Incorporating fish demographics and variations in schooling formations will increase the model's biological complexity but with a concurrent increase in realism. Integrating fully developed physical and hydrodynamic models (e.g., Salish Sea Model, Khangaonkar et al., 2017) within an ABM should further refine probability estimates of animal interactions with renewable energy devices. The simulation model can be further adapted to accommodate variable turbine rotor rotation with changes in tidal speed that will affect blade strike probabilities.

In summary, interactions between marine organisms and tidal turbines remain largely unquantified due to dynamic tidal sites limiting the efficacy of available optic and acoustic monitoring tools. As a complementary alternative, ABMs can be used to explore behavioral factors (e.g., aggregation and avoidance) that affect interactions between individuals, populations, and tidal turbines. This study provides insights into the dynamics of fish-turbine interactions, highlighting the influence of turbine design, fish abundance, aggregation behavior, and tidal speed on encounter and impact probabilities, which increases the understanding of factors impacting marine animal - MRE device interactions. Risk retirement is the process by which, based on current knowledge, risks associated with animals and MRE devices can be considered understood or effectively managed (Copping et al., 2020b). Regulators can use existing empirical data and encounter-impact models to accurately assess impact risks. This information can be then used to inform decisions related to turbine installation, operation, and mitigation regulations.

6.5 Lessons Learned

6.5.1 Review of the Two Modeling Approaches

Statistical and simulation models each bring unique strengths and limitations to estimating probabilities of fish-turbine encounters and interactions. Statistical models rely on empirical data, while simulation models aim to replicate real-world processes over time, drawing conclusions from simulated system behaviors (Banks, 1999). The choice between these two models depends on research objectives, available data, and computational resources. Integrating insights from both approaches offers a consistency check of the results, a method to identify important data streams that may not yet exist, and the potential for comprehensive assessments of environmental impacts, especially in dynamic ecological systems such as tidal turbine sites.

6.5.1.1 *Fish Positions and Behaviors*

Animal behavior is complex and is challenging to replicate in modeling frameworks (Parrish and Edelstein-Keshet, 1999). Fish exhibit a wide range of behaviors, including intraspecies interactions, obstacle avoidance, locomotion, and aggregation (Lopez et al., 2012). Individual and aggregated fish trajectories are ideal for analyzing fish positions over time and can help predict whether fish are attracted to or will avoid structures such as tidal turbines.

In the statistical model, fish positions and avoidance behavior are inferred from the vertical spatial distribution data collected at Admiralty Inlet, WA, USA without additional assumptions. The accuracy of the model depends on the availability and quality of observational data, particularly individual animal trajectories, which are often limited by monitoring capabilities and data resolution (Williamson et al., 2017).

The simulation model simulates fish behaviors based on physiological constraints (e.g., swimming speed) and responses to environmental factors (e.g., tidal flow rates), which influence active and passive avoidance strategies. Simulation techniques can track individual fish trajectories in both space and time, enabling analysis of spatial distributions within model components or avoidance of turbines. However, simulations rely heavily on assumptions that must be validated with empirical data and those data streams may or may not be available. Regardless of the model structure, both the statistical and simulation model require sufficient data on complex animal positions and behaviors from the field to produce realistic results.

6.5.1.2 *Hydrodynamics*

Incorporating hydrodynamics into statistical or simulation modeling techniques adds complexity, often requiring the development or integration of specialized external models such as computational fluid dynamics or incorporating data from acoustic monitoring instruments like Acoustic Doppler Current Profilers (ADCPs). Both statistical and simulation models can use empirical data and hydrodynamic inputs to quantify flow fields at marine energy sites (e.g., Day et al., 2015), enabling evaluations of fish distributions and behaviors at flow velocities through tidal cycles. For example, our statistical model was parameterized with data obtained during both day and night, through a full tidal cycle. In the simulation model, we incorporated a range of tidal velocities to represent a full tidal cycle. The integration of hydrodynamics is crucial for analyzing interactions between animals and devices to provide insight on how these interactions vary with periodic environmental conditions.

6.5.1.3 *Computation*

Both model implementations involve trade-offs on assumptions, model structure, spatial-temporal resolution, and computational demands. The statistical model relies on available data and reflects real-

world conditions, but the efficacy is limited by sufficient and appropriate data streams. For example, the spatial limitation of the statistical model is evident in its inability to use two-dimensional data to estimate three-dimensional individual fish positions and avoidance behaviors. Although the Admiralty Inlet acoustic data were collected in three-dimensional space over time, the geometry of the echosounder beam (i.e., which represents a cone) causes the data to be reported as planar density. Using a multibeam sonar with a wide sampling swath up to 180 degrees could preserve the third dimension in spatial surveys.

6.5.1.4 Overall Comparison

The simulation model offers greater flexibility in spatial and temporal structuring, allowing simulations to be tailored to address specific research questions. The simulation model can also be used to calculate probabilities for populations of fish by incorporating social behaviors. This flexibility comes at the cost of increased computational complexity and resource demands. Simulation models are contingent on the rules and assumptions within the model, potentially introducing bias or inaccuracy that must be validated against empirical data. Additionally, changes in simulation run times, which may increase with model complexity, could present practical constraints depending on model application. In summary, the statistical model offers a foundational understanding of individual behaviors based on available data without relying on assumptions. In contrast, the simulation model allows for more flexibility in exploring complex interactions within populations, though introduces additional assumptions. Both models depend on the availability of data streams and computational resources, which must be considered when determining research objectives.

6.5.2 Data availability

Data availability is a crucial component that affects statistical and simulation model validation and accuracy. Both models developed in this study exemplify the use of empirical data from Admiralty Inlet where data from mobile echosounders, stationary ADCPs, and trawl catch surveys provide information on fish distribution species composition, and tidal velocity. In cases where the Admiralty Inlet data could not be used to parameterize specific model variables (e.g., collision and/or blade strike rates, herring aggregatory behaviors), both models used literature values as substitutes for missing parameter values. These parameter values are sourced from several tidal energy sites or laboratory settings, which could influence model accuracy and encounter-impact estimates.

To validate the encounter-impact probability model, a complete dataset of fish-turbine trajectories, encounters, and interactions are needed. Currently, there are only a few data streams available that are suitable for model use. Empirical data streams that are not currently available include fish colliding with stationary turbine structures (Müller et al., 2023; Peraza and Horne, 2023) and sequential collision and blade strike rates (Peraza and Horne, 2023). Blade strike rates from the field are also needed, as the few existing rates are derived from laboratory flume studies that do not accurately represent realistic tidal environments (e.g., Yoshida et al., 2020, 2021), or are captured in the field but during a short time period (i.e., 21 days) (e.g., Courtney et al., 2022). Capturing additional individual and aggregated fish trajectories from at least a hundred meters away from a turbine, similar to the data collected in Shen et al. (2016), will provide insights into fish behaviors related to active and passive avoidance and provide encounter data within the zone of influence and entrainment model components. Turbine noise is another factor to be considered in data collection (Mitson, 1995), as hearing-sensitive fish, such as herring (Mitson, 2003), may detect low-frequency turbine noise from large distances (>100's m) that potentially serve as an initial cue for fish to avoid a device (Halvorsen et al., 2011). Once a robust dataset

is obtained to validate the encounter-impact model, resource managers can potentially extend the use of the model to estimate mortality of a given species at a particular MRE site (Copping et al., 2023).

6.5.3 Technology Requirements for Data Acquisition

There are different types of acoustic and optical technologies that can be used to acquire data appropriate for analyzing fish approach and interactions with tidal turbines. Mobile and stationary echosounders are effective tools for capturing fish trajectories as they approach tidal turbines (e.g., Shen et al., 2016). However, these technologies are unlikely to detect all fish across water depths, and often face challenges in classifying species within mixed fish communities (Williamson et al., 2017). Acoustic cameras can document interactions between fish and turbines (e.g., Bevelhimer et al., 2017; Viehman and Zydlewski, 2015), but any underwater optic instrument (e.g., DIDSON, Belcher et al., 2002) is limited in its detection range (Martignac et al., 2014), has image clarity dependent on water turbidity, and use artificial light to reduce these factors, which can affect fish behavior around devices (Staines et al., 2022). Acoustic telemetry can also be used to monitor fish movement through space and time (e.g., Bangley et al., 2022; Sanderson et al., 2023) if hydrophone receivers and bathymetry facilitate complete coverage of a site. Acoustic telemetry systems can be deployed over several months, which can provide extensive monitoring of fish behavior near tidal devices. Through a combination of these technologies, a comprehensive dataset can be acquired to thoroughly investigate the behavior and interactions of fish around tidal turbine structures.

6.5.4 Assessment of Additional Direct and Delayed Potential Impacts

Interactions between fish and tidal turbines can result in negative impacts, including collisions with turbine structures and blade strikes. These impacts exemplify direct interactions that may occur between animals and tidal turbines. Collecting data from tidal energy sites pose many challenges due to sites being high-energy environments with fast-moving and often turbid waters (Copping et al., 2020), making data collection difficult. For example, echoes of bubbles, drifting debris or solid surfaces such as rocks can result in poor quality data (Martignac et al., 2014). As an alternative, experimental flume studies (e.g., Amaral et al., 2015; Castro-Santos and Haro, 2015) have demonstrated potential fish-turbine effects and can be used to assess direct and delayed injury and/or mortality. Unfortunately, flume studies do not mimic real-world processes and the extent of injury or mortality from collisions and blade strikes remains uncertain.

Additional impacts of commercial-scale tidal arrays have not been evaluated. To maximize the economic benefits of capital infrastructure and power generation, an array of tidal turbines is necessary. Current research is largely focused on the effects of interactions with a single tidal turbine, but it remains unclear how these findings scale to large commercial sites and whether the presence and operation of multiple turbines introduce additional effects (Hasselman et al., 2024). These installations, which can occupy large areas of the seafloor, may alter fish migratory and foraging patterns, leading to further potential impacts (Hemery et al., 2021). Moving forward, it is crucial for future studies to expand beyond examining impacts of collision and blade strikes at the scale of single turbines. Given the potential alterations to fish population displacement caused by large-scale commercial tidal arrays, comprehensive research is needed to assess additional impacts to ensure the sustainable deployment of tidal energy infrastructure.

7 Conclusions

7.1 Collision and Behavioral Observation

The field observations around the turbine in Agate Pass, WA demonstrated that it is possible to automatically detect and track fish in optical camera data. While full automation of the 3D tracking was not possible given the size of the dominant fish species present during the survey, the custom feature point model should be effective in cases with additional training data, larger targets of interest, and better optical clarity. Similarly, while automatic detection of targets in acoustic imagery was not possible during the Agate Pass deployment, this was a consequence of small targets with limited backscatter in an environment with a high noise floor from air bubbles. The passive acoustic measurement techniques developed for this project included a novel approach for assessing the probable frequencies of radiated noise through motor, dockside measurements. Passive acoustic instrumentation was also effective at localizing noise from a mooring in an energetic tidal channel. In future deployments, passive acoustic and flow field information could be combined with optical camera and sonar imagery to quantify and interpret collision risk for a range of marine animals.

7.1.1 Summary of Lessons Learned

The following summarizes lessons learned from this deployment.

Turbine deployment from a surface platform complicated the study of environmental effects and ability to automate the data processing pipeline.

- The platform (R/V Russell Davis Light) introduced bubbles around the turbine, raising the noise floor for active acoustic measurements, produced significant noise from onboard systems (e.g., generators), and its mooring lines necessitated a significant stand-off for passive acoustic measurements. These factors limited our ability to employ sensors as they would around a seabed-deployed turbine.
- The high cost of keeping the platform moored in the tidal channel limited the duration of the deployment, which, in turn, limited the volume of data for model training, as well as the variability in ambient conditions (e.g., water clarity, light) and species composition.
- The complexity of mooring the platform resulted in a relatively restrictive schedule for anchoring and removal (i.e., both operations needed to take place during neap periods occurring every 14 days), which, combined with vessel and operator availability resulted in deployment during a period with relatively high primary productivity and correspondingly low water clarity. This complicated the automatic detection of targets in optical data due to contrast.

Training machine learning models to detect relatively rare events requires a sequential approach.

- There is a fundamental trade-off between assessing collision risk and ensuring sufficient data are available to train models that can detect targets of interest over a range of ambient conditions.
- At a new site, sampling at a relatively high duty cycle (e.g., continuously during daylight hours), but at relatively low acquisition rates (e.g., 1 Hz) is likely needed to capture as many events of interest as possible without accruing an unmanageable volume of data.
- As models are trained and demonstrate acceptable precision and recall, acquisition can transition to a triggered mode at higher frame rates (e.g., > 20 Hz) required to resolve collision events.
- These competing factors become easier to manage over a longer deployment, though periodic reversion to high duty cycles may be necessary to verify model performance.

The volume of data required to train automatic behavioral classification models is daunting.

- Data must be collected for a range of species and ambient conditions to ensure that 3D tracking algorithms and behavioral classification are robust. This requires at least an order of magnitude more data for a single species than was collected during the Agate Pass deployment.

This project was a microcosm of why environmental monitoring around marine energy converters is logistically difficult.

- The complexity of coordinating multiple investigators at multiple institutions (initially PNNL, University of Alaska Fairbanks, and University of Washington) around uncertain turbine deployment timelines was challenging. Multiple personnel who were initially intended to be involved in the study were either unavailable due to workload or had left their original institutions for private industry by the time we reached the point where they would have participated in the study.
- Had the fish tagging component of the study been maintained, this would have further constrained timelines due to the limits on how long fish can be held in an artificial environment once hatched and implanted with tracking tags.
- More rapid-response funding mechanisms, such as TEAMER, may be more effective for situations where critical elements of the project timeline have significant uncertainty.

The project was envisioned as a set of tasks executed in series, but parallel execution would have been more effective.

- The initial conception was of a sequential hand-off in information and interpretation from data collection to model training to behavioral assessment.
- A “co-design” framework, in which all members of the study had been engaged simultaneously in the meaningful manner would have been more expensive to execute but could have potentially contributed to more productive outcomes (e.g., needs for behavioral assessment incorporated into data collection plans to maximize value of data collected).

7.1.2 Application to Turbine Lander Deployment at MCRL

From October 18, 2023 – March 7, 2024 the same cross-flow turbine and power take-off were deployed on the seabed at MCRL and equipped with an Adaptable Monitoring Package (Figure 59).



Figure 59: Turbine Lander equipped with Adaptable Monitoring Package prior to deployment at MCRL (credit: Chris Bassett)

During this deployment, several of the approaches developed under this project were employed, including:

- Automated detection of targets of interest in optical data streams;
- Stereo tracking of harbor seals in close proximity to the turbine;
- Acoustic surveys using drifting measurements; and
- Identifying operational adjustments following a blade loss event.

Overall, this demonstrates how approaches developed and tested in one context can benefit others, sometimes in unexpected ways.

7.1.3 Automated Target Detection

Following a period of manual review and model training (YOLOv8), the AMP in Sequim Bay was set up for automated detection and classification of optical imagery and later acoustic imagery. These models were ultimately retrained and updated as volumes of detected targets increased throughout the deployment. No overall metrics for the deployment have been generated at the time of this report, but well over 100 individual events corresponding to seals, diving birds, and fish were captured. Preliminary assessments of optical data revealed that many examples of seals and diving birds in the vicinity of the rotor (Figure 60) were captured by these automated detection algorithms. Efforts to quantify detection metrics and improve model detection and classification are ongoing, but results to date make clear that adequately trained models can capture events of interest and reduce the processing burden corresponding to manual review.

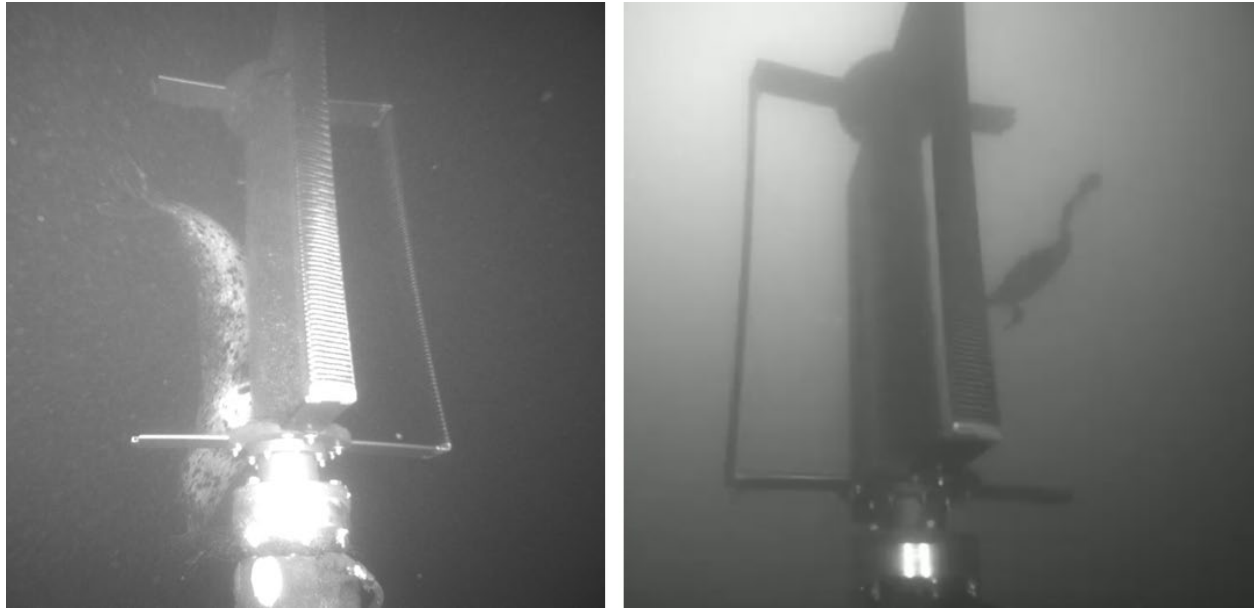


Figure 60: Two images of animals captured in near real-time using automated target detection and classification from the Sequim Bay deployment. (left) A seal at night captured when the cameras and LEDs were triggered by a detection from the acoustic cameras. (right) A double-crested cormorant capturing prey (a small fish) after pursuing it in the vicinity of the rotor. Both of these images were acquired after the loss of one blade in a debris collision event (Section 7.1.6)

7.1.4 Stereo Tracking of Harbor Seals

Manual review of data, including automated detections, performed to date suggests that diving birds and fish were typically only detected in the vicinity of the rotor during periods when the rotor was stationary. In contrast, multiple sequences were captured when seals were present near the rotor while operating. Using the stereo optical capabilities, two sequences has been annotated and processed to triangulate the position of the seal relative to the rotor. In the video of this event, the seal is seen passively drifting past the rotor while observing it. After passing downstream, the seal swims back to approach the swept area of the rotor through the wake. Throughout the sequence the seal appears in control of its movements, consistent with the relatively low velocity in the wake (Figure 47). The triangulation (Figure 61) suggests that the seal moves extremely close to the operating rotor and, potentially, briefly inside the rotor swept area under its own control before backing away. Despite some uncertainty in the triangulated positions, our confidence in this inference as quite high given that measurements of the length of the blades using the stereo optical processing was approximately 1.20 m while the known length of the blades is 1.19 cm. Use of the triangulation in this case is invaluable, as the camera position relative to the seal makes it appear that the seal is well inside the cylinder swept by the rotor. Sequences like this, coupled with good agreement between the sizes inferred from the optical measurements and their true values, make clear the benefits of stereo optical imagery and the potential for it to directly address questions related to collision.

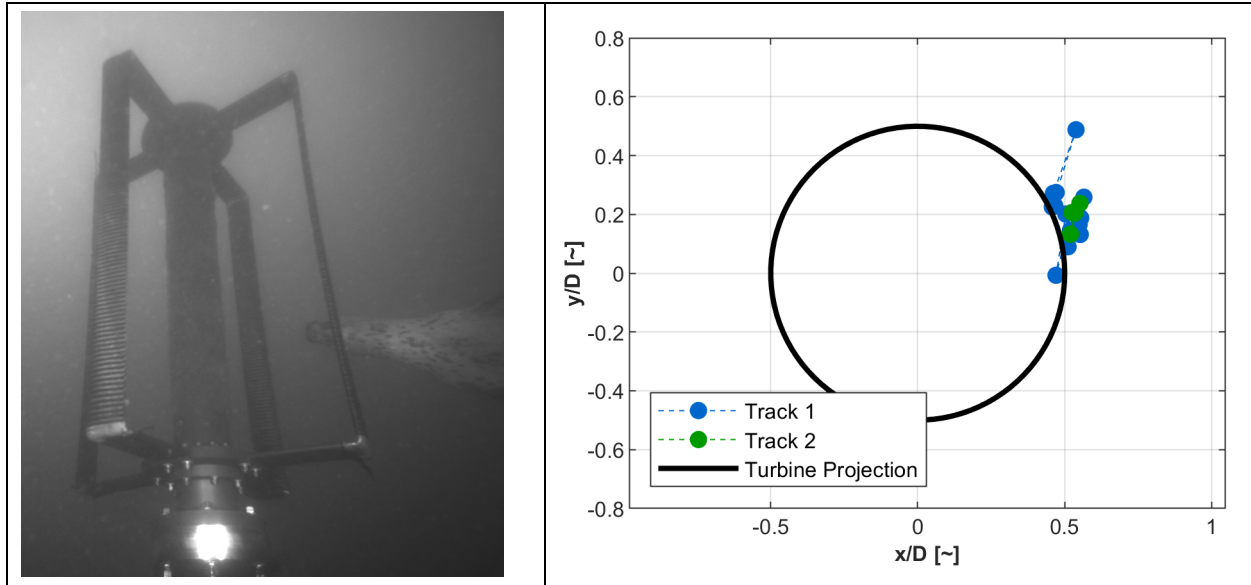


Figure 61. (left) An image of the seal in the vicinity of the operating rotor. **(right)** Triangulated location of the seal's snout on two close approaches projected into a top-down plane and normalized by the turbine rotor diameter (0.85 m turbine diameter, D). This shows that despite the position from the camera perspective in the left image, the seal's snout remains just outside the rotor swept area during both events.

7.1.5 Drifting Acoustic Surveys

DAISYS were used to survey patterns of radiated noise around the Turbine Lander. Unlike the survey in Agate Pass where the risk of mooring line entanglement necessitated a stand-off distance of 100 m from the turbine and test platform, DAISYS were able to pass within meters of the Turbine Lander. At this range, we observe expected tones from the variable frequency drive (VFD), as well as relatively broadband (1 – 8 kHz) sound from turbine mechanical noise (e.g., components of the bearing pack). The primary rotational tone is also present, but nearly masked by MCRL's seawater pump, which produces an intense tone around 200 Hz.

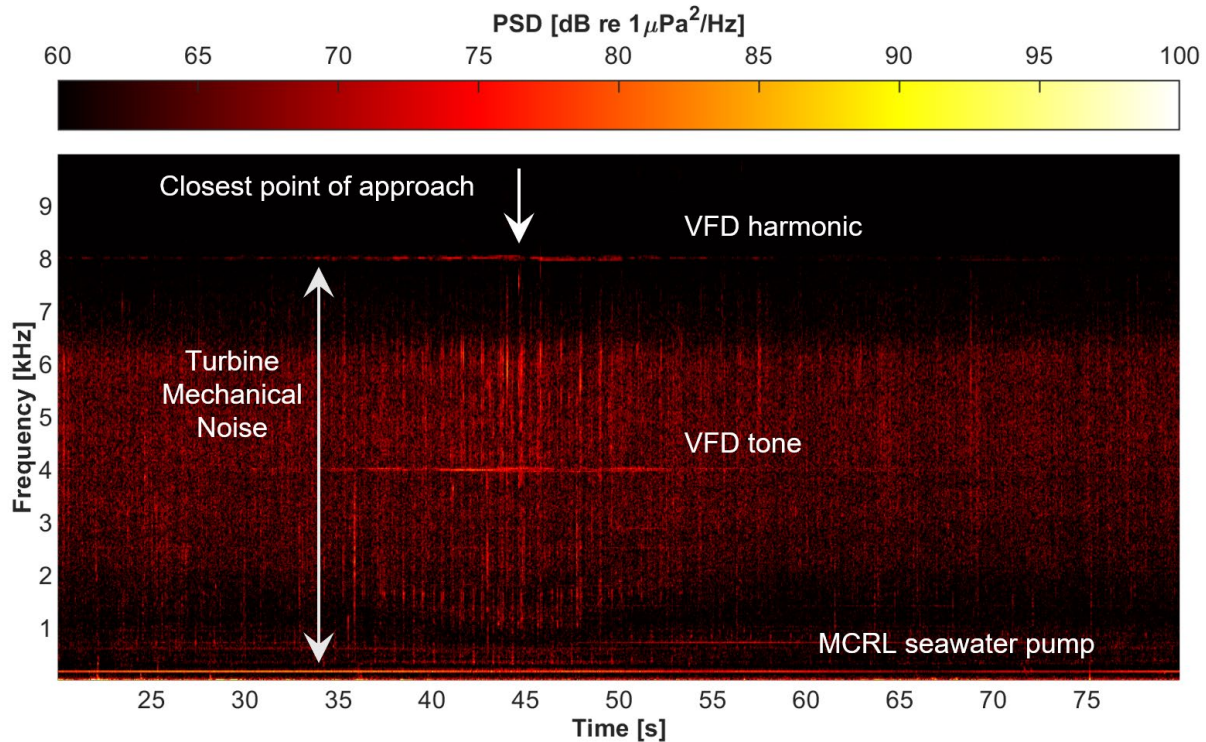


Figure 62: Measurements of radiated noise from Turbine Lander at MCRL using DAISYs. Time is duration, in seconds, relative to the start of the drift. At the closest point of approach, the DAISY is ~4 m from the Turbine Lander.

7.1.6 Adjusting for Blade Loss

On January 11, debris collision with the turbine resulted in the loss of one of the four blades. To understand the effect this would have on turbine operation, we used the scale model turbine from the lab-scale wake studies (Task 10.2). By removing one of the blades, we were able to rapidly characterize turbine performance and loads for a range of tip-speed ratios. From this, we determined that (1) even with a missing blade, substantial power generation was still possible, (2) the turbine would experience higher peak-to-average force ratios, but that these would still be within the operational limits of the bearing and foundation, and (3) that the target tip-speed ratio for the controller should marginally increase as a consequence of reduced rotor solidity (Figure 63). When this increase in tip-speed ratio was implemented on the next tidal cycle, time-average turbine power output increased by greater than 40% under comparable inflow conditions.

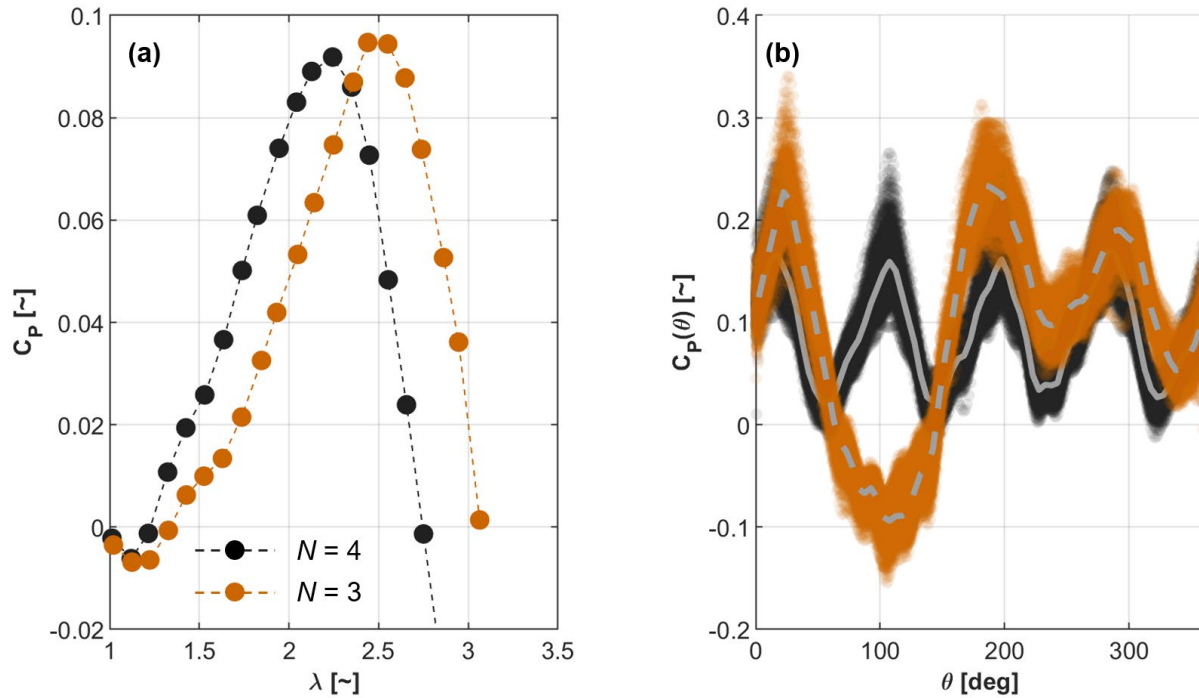


Figure 63: Performance changes associated with blade loss as estimated from laboratory-scale experiments. (a) Cycle-average efficiency as a function of tip-speed ratio for the original 4-bladed turbine and damaged 3-bladed turbine. (b) Phase-average efficiency (as a function of blade 1 angular position) at the optimal tip-speed ratio for each turbine. Markers represent individual measurements and grey lines denote the average at each azimuthal position. The influence of the missing blade is apparent.

7.2 Collision Modeling

The statistical and simulation implementations of the probabilistic encounter-impact model reveal several key insights. The statistical model found higher probabilities of encounter and impact at night with larger turbine structures, such as the representative cross-flow turbine used in this study. The simulation model highlights the importance of behavioral traits, such as avoidance influenced by fish active (i.e., swimming) or passive (i.e., drifting) locomotion and social aggregation, as crucial factors to prioritize in future models. Our series of tests on the three experimental factors in the simulation model demonstrate that tidal speed significantly affects fish-turbine interactions. Therefore, future modeling efforts should prioritize incorporating intricate fish behaviors and tidal speeds to ensure a comprehensive understanding of how these factors contribute to potential impacts from fish-turbine interactions or avoidance.

Additional research and empirical data collection are necessary to gain a thorough understanding of interactions between animals and tidal turbines. While statistical and simulation models can help predict potential animal-turbine encounter and interaction rates, it is crucial to prioritize gathering data on how and when fish detect the turbine, and whether this triggers avoidance behavior at longer distances observed by Shen et al. (2016). Additional monitoring around tidal turbines could also reveal whether fish fail to avoid the turbine and hit the turbine support structure or are struck by its blades. These data can be used to quantify direct rates of injury or mortality. Information on potential injury or mortality rates from encounter-impact models are used by regulators and managers when developing policies for tidal turbine deployment and operation in the U.S.

8 Acknowledgements

- Task 10.1: Ian Borchert operated the small boat used for the DAISY survey during the Agate Pass deployment.
- Task 10.2: Heidi Resing, Andrew Witt, and Aidan Hunt contributed to the design, fabrication, and initial testing of the scale model cross-flow turbine.
- Task 10.3: Andy Seitz (University of Alaska Fairbanks) contributed to the initial conception of this task and supported the hand-off to Oregon State University for task completion.
- Task 10.4: Andrew Berhdal and Brendan Wallace for insight and guidance on agent-based simulation modeling

9 References

- Amaral, S., Bevelhimer, M., Čada, G., Giza, D., Jacobson, P., McMahon, B., and Pracheil, B. 2015. Evaluation of Behavior and Survival of Fish Exposed to an Axial-Flow Hydrokinetic Turbine. *North American Journal of Fisheries Management*, 35, 97–113.
- Aoki, I. 1982. A simulation study on the schooling mechanism in fish. *NIPPON SUISAN GAKKAISHI*. Available at: <https://doi.org/10.2331/suisan.48.1081>
- Band, B., C. Sparling, D. Thompson, J. Onoufriou, E. San Martin, and N. West. 2016. Refining Estimates of Collision Risk for Harbour Seals and Tidal Turbines. Report by ABP Marine Environmental Research Ltd (ABPmer), Sea Mammal Research Unit (SMRU), and SMRU Consulting. pp 133.
- Bangley, C. W., Hasselman, D. J., Flemming, J. M., Whoriskey, F. G., Culina, J., Enders, L., and Bradford, R. G. 2022. Modeling the Probability of Overlap Between Marine Fish Distributions and Marine Renewable Energy Infrastructure Using Acoustic Telemetry Data. *Frontiers in Marine Science*, 9.
- Banks, J. 1999. Introduction to simulation. *Proceedings of the 31st Conference on Winter Simulation: Simulation---a Bridge to the Future - Volume 1*, 7–13.
- Bassett, C. and Polagye, B., 2020. Risk to marine animals from underwater noise generated by marine renewable energy devices, in OES-Environmental 2020 State of the Science Report: Environmental Effects of Marine Renewable Energy Development Around the World, edited by A. Copping and L. Hemery, Ocean Energy Systems (OES), pp. 67–85
- Belcher, E., Hanot, W., and Burch, J. 2002. Dual-Frequency Identification Sonar (DIDSON). *Proceedings of the 2002 International Symposium on Underwater Technology (Cat. No.02EX556)*, 187–192.
- Bender, A., Langhamer, O., Francisco, F., Forslund, J., Hammar, L., Sundberg, J., and Molander, S. 2023. Imaging-sonar observations of salmonid interactions with a vertical axis instream turbine. *River Research and Applications*, 39: 1578–1589.
- Bevelhimer, M., Scherelis, C., Colby, J., and Adonizio, M. A. 2017. Hydroacoustic Assessment of Behavioral Responses by Fish Passing Near an Operating Tidal Turbine in the East River, New York. *Transactions of the American Fisheries Society*, 146, 1028–1042.
- Bernardi, S., and Scianna, M. 2020. An agent-based approach for modelling collective dynamics in animal groups distinguishing individual speed and orientation. *Philosophical Transactions of the Royal Society B: Biological Sciences*, 375, 20190383.
- Bonabeau, E. 2002. Agent-based modeling: Methods and techniques for simulating human systems. *Proceedings of the National Academy of Sciences*, 99(suppl_3), 7280–7287.

- Brown, R. S., Carlson, T. J., Gingerich, A. J., Stephenson, J. R., Pflugrath, B. D., Welch, A. E., Langeslay, M. J., Ahmann, M. L., Johnson, R. L., Skalski, J. R., Seaburg, A. G., and Townsend, R. L. 2012. Quantifying Mortal Injury of Juvenile Chinook Salmon Exposed to Simulated Hydro-Turbine Passage. *Transactions of the American Fisheries Society*, 141(1), 147–157.
- Buenau, K. E., Garavelli, L., Hemery, L. G., and García Medina, G. 2022. A Review of Modeling Approaches for Understanding and Monitoring the Environmental Effects of Marine Renewable Energy. *Journal of Marine Science and Engineering*, 10, Article 1.
- Cada, G., Ahlgrimm, J., Bahleda, M., Bigford, T., Stavrakas, S. D., Hall, D., Moursund, R., and Sale, M. 2007. Potential Impacts of Hydrokinetic and Wave Energy Conversion Technologies on Aquatic Environments. *Fisheries*, 32, 174–181.
- Castro-Santos, T., and Haro, A. 2015. Survival and Behavioral Effects of Exposure to a Hydrokinetic Turbine on Juvenile Atlantic Salmon and Adult American Shad. *Estuaries and Coasts*, 38, 203–214.
- Codling, E. A., Plank, M. J., and Benhamou, S. 2008. Random walk models in biology. *Journal of The Royal Society Interface*, 5, 813–834.
- Copping, A.E. and Hemery, L.G., 2020. OES-environmental 2020 state of the Science report: Environmental effects of marine renewable energy development around the world. Report for ocean energy systems (OES).
- Copping, A., Sather, N., Hanna, L., Whiting, J., Zydlewski, G., Staines, G., Gill, A., Hutchison, I., O'Hagan, A., Simas, T. and Bald, J., 2016. Annex IV 2016 state of the science report: Environmental effects of marine renewable energy development around the world. Ocean Energy Systems, p.224.
- Copping, A., Hemery, L., Overhus, D., Garavelli, L., Freeman, M., Whiting, J., Gorton, A., Farr, H., Rose, D., and Tugade, L. 2020a. Potential Environmental Effects of Marine Renewable Energy Development-The State of the Science. *Journal of Marine Science and Engineering*, 8.
- Copping, A. E., Freeman, M. C., Gorton, A. M., and Hemery, L. G. 2020b. Risk Retirement—Decreasing Uncertainty and Informing Consenting Processes for Marine Renewable Energy Development. *Journal of Marine Science and Engineering*, 8, Article 3.
- Copping, A. E., Hemery, L. G., Viehman, H., Seitz, A. C., Staines, G. J., and Hasselman, D. J. 2021. Are fish in danger? A review of environmental effects of marine renewable energy on fishes. *Biological Conservation*, 262, 109297.
- Copping, A. E., Hasselman, D. J., Bangley, C. W., Culina, J., and Carcas, M. 2023. A Probabilistic Methodology for Determining Collision Risk of Marine Animals with Tidal Energy Turbines. *Journal of Marine Science and Engineering*, 11, Article 11.
- Cotter, E. and Polagye, B., 2020. Automatic classification of biological targets in a tidal channel using a multibeam sonar. *Journal of Atmospheric and Oceanic Technology*, 37(8), pp.1437-1455.
- Cotter, E. and Staines, G., 2023. Observing fish interactions with marine energy turbines using acoustic cameras. *Fish and Fisheries*, 24(6), pp.1020-1033.
- Courtney, M. B., Flanigan, A. J., Hostetter, M., and Seitz, A. C. 2022. Characterizing Sockeye Salmon Smolt Interactions with a Hydrokinetic Turbine in the Kvichak River, Alaska. *North American Journal of Fisheries Management*, 42, 1054–1065.
- Couzin, I. D., Krause, J., James, R., Ruxton, G. D., and Franks, N. R. 2002. Collective Memory and Spatial Sorting in Animal Groups. *Journal of Theoretical Biology*, 218, 1–11.

- Couzin, I. D., Krause, J., Franks, N. R., and Levin, S. A. 2005. Effective leadership and decision-making in animal groups on the move. *Nature*, 433, 7025.
- Dadswell, M.J. and Rulifson, R.A., 1994. Macrotidal estuaries: a region of collision between migratory marine animals and tidal power development. *Biological Journal of the Linnean Society*, 51(1-2), pp.93-113.
- Day, A. H., Babarit, A., Fontaine, A., He, Y.-P., Kraskowski, M., Murai, M., Penesis, I., Salvatore, F., and Shin, H.-K. 2015. Hydrodynamic modelling of marine renewable energy devices: A state of the art review. *Ocean Engineering*, 108, 46–69.
- Domenici, P., and Batty, R. S. 1997. Escape behaviour of solitary herring (*Clupea harengus*) and comparisons with schooling individuals. *Marine Biology*, 128, 29–38.
- Eichhorn, M., Johst, K., Seppelt, R., and Drechsler, M. 2012. Model-Based Estimation of Collision Risks of Predatory Birds with Wind Turbines. *Ecology and Society*, 17(2): 1.
- Frey, C. H., and Patil, S. R. 2002. Identification and Review of Sensitivity Analysis Methods. *Risk Analysis*, 22, 553–578.
- Gende, S., A.N. Hendrix, K.R. Harris, B. Eichenlaub, J. Nielsen, and S. Pyare. 2011. A Bayesian approach for understanding the role of ship speed in whale-ship encounters. *Ecological Applications* 21: 2232-2240.
- Grant, M.C., M. Trinder, and N.J. Harding. 2014. A diving bird collision risk assessment framework for tidal turbines. Scottish Natural Heritage Commissioned Report No. 773, pp. 38.
- Grippe, M., H. Shen, G. Zydlewski, S. Rao, and A. Goodwin. 2017. Behavioral Responses of Fish to a Current-Based Hydrokinetic Turbine Under Multiple Operational Conditions. Final Report. Argonne National Laboratory ANL/EVS-17/6, pp 49.
- Goodwin, R.A., M. Politano, J.W. Garvin, J.M. Nestler, D. Hay, J.J. Anderson, L.J. Weber, E. Dimperio, D.L. Smith, and M. Timko, 2014. Fish navigation of large dams emerges from their modulation of flow field experience. *Proceedings of the National Academy of Sciences* 111: 5277–5282
- Guido, J. T., 2014. 'An Approach to the Active Defense of Wireless Radio Networks', *Doctoral dissertation, University of Colorado Colorado Springs*. Available at: http://www.jeffreyguido.com/work/tdoa_page.html.
- Halvorsen, M., Carlson, T., and Copping, A. 2011. *Effects of Tidal Turbine Noise on Fish Task 2.1.3.2: Effects on Aquatic Organisms: Acoustics/Noise - Fiscal Year 2011 - Progress Report - Environmental Effects of Marine and Hydrokinetic Energy*.
- Hammar, L., L. Eggertsen, S. Andersson, J. Ehnberg, R. Arvidsson, M. Gullström, and S. Molander. 2015. A probabilistic model for hydrokinetic turbine collision risks: exploring impacts on fish. *PLoS One* 10: e0117756.
- Harrison, T. W., Clemett, N., Polagye, B., & Thomson, J., 2023 'Experimental Validation of Float Array Tidal Current Measurements in Agate Pass, WA', *Journal of Atmospheric and Oceanic Technology*. Available at <https://doi.org/10.1175/JTECH-D-22-0034.1>.
- Hasselmann, D. J., Hemery, L. G., Copping, A. E., Fulton, E. A., Gill, A. B., & Polagye, B. 2024. *Improving Understanding of Environmental Effects from Single MRE Devices to Arrays*. Presentation available at: https://pamec.energy/wp-content/uploads/2023/11/20240124_EnvironmentalEffects_Hasselmann-Daniel.pdf

- He, P. 1993. Swimming speeds of marine fish in relation to fishing gears. *ICES Marine Science Symposium*, 196: 183–189.
- Hemery, L. G., Copping, A. E., and Overhus, D. M. 2021. Biological Consequences of Marine Energy Development on Marine Animals. *Energies*, 14, Article 24.
- Hinckley, S., C. Parada, J.K. Horne, M. Mazur, and M. Woillez. 2016. Comparison of individual-based model output to data using a model of walleye pollock early life history in the Gulf of Alaska. *Deep-Sea Research II* 132: 240-262.
- Horne J., Jacques D., Parker-Stetter S., Linder H., and Nomura J. 2013. Evaluating Acoustic Technologies to Monitor Aquatic Organisms at Renewable Energy Sites Final Report (U.S. Dept. of the Interior, Bureau of Ocean Energy Management. BOEM), 2014–2057. Available at: <https://espis.boem.gov/final%20reports/5415.pdf>.
- Jacques, D. A. (2014). *Describing and Comparing Variability of Fish and Macrozooplankton Density at Marine Hydrokinetic Energy Sites*. Available at <https://digital.lib.washington.edu:443/researchworks/handle/1773/27479>
- Khangaonkar, T., Long, W., and Xu, W. 2017. Assessment of circulation and inter-basin transport in the Salish Sea including Johnstone Strait and Discovery Islands pathways. *Ocean Modelling*, 109, 11–32.
- Li, H., Kolpas, A., Petzold, L., and Moehlis, J. 2009. Parallel simulation for a fish schooling model on a general-purpose graphics processing unit. *Concurrency and Computation: Practice and Experience*, 21, 725–737.
- Linder, H.L. and J.K. Horne. 2018. Evaluating statistical models to measure environmental change: A tidal turbine case study. *Ecological Indicators* 84: 765-792.
- Linder, H.L., J.K. Horne, and E.J. Ward. 2017. Modeling baseline conditions of ecological indicators: Marine renewable energy environmental monitoring. *Ecological Indicators* 83: 178-191.
- Lopez, U., Gautrais, J., Couzin, I., and Theraulaz, G. 2012. *From behavioural analyses to models of collective motion in fish schools*. *Interface Focus* 2, 693–707. Available at: <https://doi.org/10.1098/rsfs.2012.0033>
- Marras, S., and Domenici, P. 2013. Schooling Fish Under Attack Are Not All Equal: Some Lead, Others Follow. *PLOS ONE*. doi:10.1371/ journal.pone.0065784
- Martignac, F., Daroux, aurélie, Baglinière, J.-L., Ombredane, D., and Guillard, J. 2014. The use of acoustic cameras in shallow waters: New hydroacoustic tools for monitoring migratory fish population. A review of DIDSON technology. *Fish and Fisheries*, 16, 486-510.
- Martin, S.B. *et al.*. 2021a. ‘Hybrid millidecade spectra: A practical format for exchange of long-term ambient sound data’, *JASA Express Letters*, 1(1), p. 011203. Available at: <https://doi.org/10.1121/10.0003324>.
- Martin, S.B. *et al.*, 2021b. ‘Erratum: Hybrid millidecade spectra: A practical format for exchange of long-term ambient sound data [JASA Express Lett. 1 (1), 011203 (2021)]’, *JASA Express Letters*, 1(8), p. 081201. Available at: <https://doi.org/10.1121/10.0005818>.
- Maclean, I. M. D., Inger, R., Benson, D., Booth, C. G., Embling, C. B., Grecian, W. J., Heymans, J. J., Plummer, K. E., Shackshaft, M., Sparling, C. E., Wilson, B., Wright, L. J., Bradbury, G., Christen, N., Godley, B. J., Jackson, A. C., McCluskie, A., Nicholls-Lee, R., and Bearhop, S. 2014. Resolving issues with environmental impact assessment of marine renewable energy installations. *Frontiers in Marine Science*, 1, 75.

- McMichael, G.A., Eppard, M.B., Carlson, T.J., Carter, J.A., Ebberts, B.D., Brown, R.S., Weiland, M., Ploskey, G.R., Harnish, R.A. and Deng, Z.D., 2010. The juvenile salmon acoustic telemetry system: a new tool. *Fisheries*, 35(1), pp.9-22.
- Misund, O. A. 1993. Dynamics of moving masses: Variability in packing density, shape, and size among herring, sprat, and saithe schools. *ICES Journal of Marine Science*, 50, 145–160.
- Mitson, R. B. 1995. *Underwater noise of research vessels: Review and recommendations* [Report]. ICES Cooperative Research Reports (CRR). Available at: <https://doi.org/10.17895/ices.pub.5317>
- Mitson, R. B. 2003. Causes and effects of underwater noise on fish abundance estimation. *Aquatic Living Resources*, 16, 255–263.
- Mutlu, E., 1996, Target strength of the common jellyfish (*Aurelia aurita*): a preliminary experimental study with a dual-beam acoustic system, *ICES Journal of Marine Science*, Volume 53, Issue 2, April 1996, Pages 309–311, <https://doi.org/10.1006/jmsc.1996.0040>
- Müller, S., Muhawenimana, V., Sonnino-Sorisio, G., Wilson, C. A. M. E., Cable, J., and Ouro, P. 2023. Fish response to the presence of hydrokinetic turbines as a sustainable energy solution. *Scientific Reports*, 13(1), Article 1.
- Okubo, A. 1971. Oceanic diffusion diagrams. *Deep-Sea Res.* 18: 789-802
- Okubo, A. 1987. *Lecture Notes in Biomathematics*, No. 71. Springer-Verlag, New York.
- Parrish, J. K., and Edelstein-Keshet, L. 1999. Complexity, Pattern, and Evolutionary Trade-Offs in Animal Aggregation. *Science*, 284, 99–101.
- Pelc, R., and Fujita, R. M. 2002. Renewable energy from the ocean. *Marine Policy*, 26, 471–479.
- Peraza, J. I., and Horne, J. K. 2023. Quantifying conditional probabilities of fish-turbine encounters and impacts. *Frontiers in Marine Science*, 10.
- Polagye, B., Strom, B., Ross, H., Forbush, D. and Cavagnaro, R.J., 2019. Comparison of cross-flow turbine performance under torque-regulated and speed-regulated control. *Journal of Renewable and Sustainable Energy*, 11(4).
- Polagye, B., Joslin, J., Murphy, P., Cotter, E., Scott, M., Gibbs, P., Bassett, C. and Stewart, A., 2020. Adaptable monitoring package development and deployment: Lessons learned for integrated instrumentation at marine energy sites. *Journal of Marine Science and Engineering*, 8(8), p.553.
- Pracheil, B.M., DeRolph, C.R., Schramm, M.P. and Bevelhimer, M.S., 2016. A fish-eye view of riverine hydropower systems: the current understanding of the biological response to turbine passage. *Reviews in Fish Biology and Fisheries*, 26, pp.153-167.
- Reynolds, C. W. 1987. Flocks, herds and schools: A distributed behavioral model. *ACM SIGGRAPH Computer Graphics*, 21, 25–34.
- Romero-Gomez, P. and M.C. Richmond. 2014. Simulating blade-strike on fish passing through marine hydrokinetic turbines. *Renewable Energy* 71: 401-413.
- Rose, D., Freeman, M., and Copping, A. (2023). Engaging the Regulatory Community to Aid Environmental Consenting/Permitting Processes for Marine Renewable Energy. *International Marine Energy Journal*, 6, 55–61
- Ross, H. and Polagye, B., 2022. Effects of dimensionless parameters on the performance of a cross-flow current turbine. *Journal of Fluids and Structures*, 114, p.103726.

- Rossington, K., and Benson, T. 2020. An agent-based model to predict fish collisions with tidal stream turbines. *Renewable Energy*, 151, 1220–1229.
- Rulifson, R.A., S.A. McKenna, and M.L. Gallagher. 1987. Tagging studies of striped bass and river herring in the upper Bay of Fundy, Nova Scotia. Institute of Coastal and Marine Research Technical Report 82-02. Greenville: East Carolina University.
- Saltelli, A. (Ed.). 2004. *Sensitivity analysis in practice: A guide to assessing scientific models*. Wiley.
- Saltelli, A. (Ed.). 2008. *Global sensitivity analysis: The primer*. Wiley.
- Sanderson, B. G., Karsten, R. H., Solda, C. C., Hardie, D. C., and Hasselman, D. J. 2023. Probability of Atlantic Salmon Post-Smolts Encountering a Tidal Turbine Installation in Minas Passage, Bay of Fundy. *Journal of Marine Science and Engineering*, 11, Article 5.
- Sayed, A.H., Tarighat, A. and Khajehnouri, N., 2005. 'Network-based wireless location: challenges faced in developing techniques for accurate wireless location information', *IEEE Signal Processing Magazine*, 22(4), pp. 24–40. Available at: <https://doi.org/10.1109/MSP.2005.1458275>.
- Schmitt, P., Culloch, R., Lieber, L., Molander, S., Hammar, L., and Kregting, L. 2017. A tool for simulating collision probabilities of animals with marine renewable energy devices. *PLOS ONE*, 12, e0188780.
- Shen, H. G.B. Zydlewski, H.A. Viehman, and G. Staines. 2016. Estimating the probability of fish encountering a marine hydrokinetic device. *Renewable Energy* 97: 746-756.
- Shields, M. A., Woolf, D. K., Grist, E. P. M., Kerr, S. A., Jackson, A. C., Harris, R. E., Bell, M. C., Beharie, R., Want, A., Osalusi, E., Gibb, S. W., and Side, J. 2011. Marine renewable energy: The ecological implications of altering the hydrodynamics of the marine environment. *Ocean & Coastal Management*, 54, 2–9.
- Simmonds, J., and MacLennan, D. (Eds.). 2005. *Fisheries Acoustics: Theory and Practice* (1st ed.). Wiley.
- Smallwood, K.S., 2007. Estimating wind turbine-caused bird mortality. *The Journal of Wildlife Management*, 71(8), pp.2781-2791.
- Snortland, A., Scherl, I., Polagye, B. and Williams, O., 2023. Cycle-to-cycle variations in cross-flow turbine performance and flow fields. *Experiments in Fluids*, 64(12), p.188.
- Staines, G.J., Mueller, R.P., Seitz, A.C., Evans, M.D., O'Byrne, P.W. and Wosnik, M., 2022. Capabilities of an acoustic camera to inform fish collision risk with current energy converter turbines. *Journal of Marine Science and Engineering*, 10(4), p.483.
- Thomas, G.L., Kirsch, J. and Thorne, R.E. 2002, Ex Situ Target Strength Measurements of Pacific Herring and Pacific Sand Lance. *North American Journal of Fisheries Management*, 22: 1136-1145. [https://doi.org/10.1577/1548-8675\(2002\)022<1136:ESTSMO>2.0.CO;2](https://doi.org/10.1577/1548-8675(2002)022<1136:ESTSMO>2.0.CO;2)
- Thompson, M., Beston, J.A., Etterson, M., Diffendorfer, J.E. and Loss, S.R., 2017. Factors associated with bat mortality at wind energy facilities in the United States. *Biological Conservation*, 215, pp.241-245.
- Thomson, J., Polagye, B., Durgesh, V. and Richmond, M.C., 2012. Measurements of turbulence at two tidal energy sites in Puget Sound, WA. *IEEE Journal of Oceanic Engineering*, 37(3), pp.363-374.
- Viehman, H.A. and Zydlewski, G.B., 2015. Fish interactions with a commercial-scale tidal energy device in the natural environment. *Estuaries and Coasts*, 38, pp.241-252.
- Viehman, H. A., Zydlewski, G. B., McCleave, J. D., and Staines, G. J. 2015. Using Hydroacoustics to Understand Fish Presence and Vertical Distribution in a Tidally Dynamic Region Targeted for Energy Extraction. *Estuaries and Coasts*, 38, 215–226.
- Wilcoxon, F. 1945. Individual Comparisons by Ranking Methods. *Biometrics Bulletin*, 1, 80–83.

- Williamson, B. J., Fraser, S., Blondel, P., Bell, P. S., Waggitt, J. J., and Scott, B. E. 2017. Multisensor Acoustic Tracking of Fish and Seabird Behavior Around Tidal Turbine Structures in Scotland. *IEEE Journal of Oceanic Engineering*, 42(4), 948–965.
- Wilson, B., R. Batty, F. Daunt, and C. Carter. 2006. Collision risks between marine renewable energy devices and mammals, fish and diving birds. Report to the Scottish Executive Scottish Association for Marine Science.
- Yoshida, T., Zhou, J., Park, S., Muto, H., and Kitazawa, D. 2020. Use of a model turbine to investigate the high striking risk of fish with tidal and oceanic current turbine blades under slow rotational speed. *Sustainable Energy Technologies and Assessments*, 37, 100634.
- Yoshida, T., Furuichi, D., Williamson, B. J., Zhou, J., Dong, S., Li, Q., & Kitazawa, D. 2021. Experimental study of fish behavior near a tidal turbine model under dark conditions. *Journal of Marine Science and Technology*, 22, 219–230.

10 Appendix 1

Table A1.1: Model component estimates for an axial-flow turbine during day.

Model Component				Active Avoidance		Passive Avoidance	
Domain	1						
Zone of Influence	0.0636						
Entrainment							
Empirical	0.00245						
Admiralty Inlet avoidance	0.0118			0.0236		0.790	
Shen <i>et al.</i> (2016) avoidance	0.0399			0.372		0	
Collision	Courtney <i>et al.</i> 2022	Yoshida <i>et al.</i> 2021	Romero-Gomez and Richmond, 2014	Zone of Influence (Shen <i>et al.</i> 2016)	Entrainment (Viehman and Zydlewski, 2015)	Zone of Influence (Shen <i>et al.</i> 2016)	Entrainment (Viehman and Zydlewski, 2015)
No avoidance	0.0374	0.0408	0.0258 - 0.0372		0.020		0.937
Admiralty Inlet avoidance	0.000443	0.000484	0.000305 - 0.000441	0.0236	0.020	0.790	0.937
Shen <i>et al.</i> (2016) avoidance	0.00149	0.00163	0.000103 - 0.00148	0.372	0.020	0	0.937
Blade strike							

Literature	0.13	0.05	0.40 - 0.133				
Admiralty Inlet avoidance	0.00154	0.000592	0.00473 - 0.00157	0.0236		0.790	
Shen <i>et al.</i> (2016) avoidance	0.00519	0.00199	0.0159 - 0.00532	0.372		0	
Collision and blade strike							
No avoidance	0.00486	0.00204	0.0103 - 0.00496		0.020		0.937
Admiralty Inlet avoidance	0.0000576	0.0000242	0.000122 - 0.0000588	0.0236	0.020	0.790	0.937
Shen <i>et al.</i> (2016) avoidance	0.000194	0.0000815	0.000412 - 0.000198	0.372	0.020	0	0.937

Table A1.2: Model component estimates for an axial-flow turbine at night.

Model Component		Active Avoidance	Passive Avoidance
Domain	1		
Zone of Influence	0.0649		
Entrainment			
Empirical	0.00250		
Admiralty Inlet avoidance	0.0118	0.0241	0.792

Shen <i>et al.</i> (2016) avoidance	0.0408			0.372		0	
Collision	Courtney <i>et al.</i> 2022	Yoshida <i>et al.</i> 2021	Romero-Gomez and Richmond, 2014	Zone of Influence (Shen <i>et al.</i> 2016)	Entrainment (Viehman and Zydlewski, 2015)	Zone of Influence (Shen <i>et al.</i> 2016)	Entrainment (Viehman and Zydlewski, 2015)
No avoidance	0.288	0.324	0.199 - 0.287		0.109		0.559
Admiralty Inlet avoidance	0.00343	0.00385	0.00236 - 0.00342	0.0241	0.109	0.790	0.559
Shen <i>et al.</i> (2016) avoidance	0.0117	0.0132	0.00812 - 0.0117	0.372	0.109	0	0.559
Blade strike							
Literature	0.13	0.022	0.40 - 0.133				
Admiralty Inlet avoidance	0.00154	0.000261	0.00475 - 0.00158	0.0241		0.792	
Shen <i>et al.</i> (2016) avoidance	0.00530	0.000987	0.0163 - 0.00544	0.372		0	
Collision and blade strike							
No avoidance	0.0375	0.00714	0.0678 - 0.0347		0.109		0.559
Admiralty Inlet avoidance	0.000446	0.0000849	0.000947 - 0.000456	0.0241	0.109	0.792	0.559

Shen <i>et al.</i> (2016) avoidance	0.00153	0.000291	0.00325 - 0.00156	0.372	0.109	0	0.559
-------------------------------------	---------	----------	-------------------	-------	-------	---	-------

Table A1.3: Model component estimates for a cross-flow turbine during day.

Model Component				Active Avoidance		Passive Avoidance	
Domain	1						
Zone of Influence	0.0636						
Entrainment							
Empirical	0.0144						
Admiralty Inlet avoidance	0.0118			0.0236		0.790	
Shen <i>et al.</i> (2016) avoidance	0.0399			0.372		0	
Collision	Courtney <i>et al.</i> 2022	Yoshida <i>et al.</i> 2021	Romero-Gomez and Richmond, 2014	Zone of Influence (Shen <i>et al.</i> 2016)	Entrainment (Viehman and Zydlewski, 2015)	Zone of Influence (Shen <i>et al.</i> 2016)	Entrainment (Viehman and Zydlewski, 2015)
No avoidance	0.0374	0.0408	0.0307 - 0.0389		0.020		0.937
Admiralty Inlet avoidance	0.000443	0.000484	0.000364 - 0.000461	0.0236	0.020	0.790	0.937
Shen <i>et al.</i> (2016) avoidance	0.00149	0.00163	0.00122 - 0.00155	0.372	0.020	0	0.937

Blade strike							
Literature	0.13	0.05	0.285 - 0.0951				
Admiralty Inlet avoidance	0.00154	0.000592	0.00845 - 0.00140	0.0236		0.790	
Shen <i>et al.</i> (2016) avoidance	0.00519	0.00199	0.0284 - 0.00474	0.372		0	
Collision and blade strike							
No avoidance	0.00486	0.00204	0.0219 -0.00462		0.020		0.937
Admiralty Inlet avoidance	0.0000576	0.0000242	0.000259 - 0.0000548	0.0236	0.020	0.790	0.937
Shen <i>et al.</i> (2016) avoidance	0.000194	0.0000815	0.000875 - 0.000184	0.372	0.020	0	0.937

Table A1.4: Model component estimates for a cross-flow turbine at night.

Model Component		Active Avoidance	Passive Avoidance
Domain	1		
Zone of Influence	0.0649		
Entrainment			
Empirical	0.0146		

Admiralty Inlet avoidance	0.0118			0.0241		0.792	
Shen <i>et al.</i> (2016) avoidance	0.0408			0.372		0	
Collision	Courtney <i>et al.</i> 2022	Yoshida <i>et al.</i> 2021	Romero-Gomez and Richmond, 2014	Zone of Influence (Shen <i>et al.</i> 2016)	Entrainment (Viehman and Zydlewski, 2015)	Zone of Influence (Shen <i>et al.</i> 2016)	Entrainment (Viehman and Zydlewski, 2015)
No avoidance	0.288	0.324	0.237 - 0.300		0.109		0.559
Admiralty Inlet avoidance	0.00343	0.00385	0.00113 - 0.00347	0.0241	0.109	0.790	0.559
Shen <i>et al.</i> (2016) avoidance	0.0117	0.0132	0.00388 - 0.0119	0.372	0.109	0	0.559
Blade strike							
Literature	0.13	0.022	0.285 - 0.0951				
Admiralty Inlet avoidance	0.00154	0.000261	0.00847 - 0.00141	0.0241		0.792	
Shen <i>et al.</i> (2016) avoidance	0.00530	0.000897	0.0291 - 0.00485	0.372		0	
Collision and blade strike							
No avoidance	0.0375	0.00714	0.0678 - 0.0285		0.109		0.559

Admiralty Inlet avoidance	0.000446	0.0000849	0.000806 - 0.000413	0.0241	0.109	0.792	0.559
Shen <i>et al.</i> (2016) avoidance	0.00153	0.000291	0.00277 - 0.00141	0.372	0.109	0	0.559

11 Appendix 2

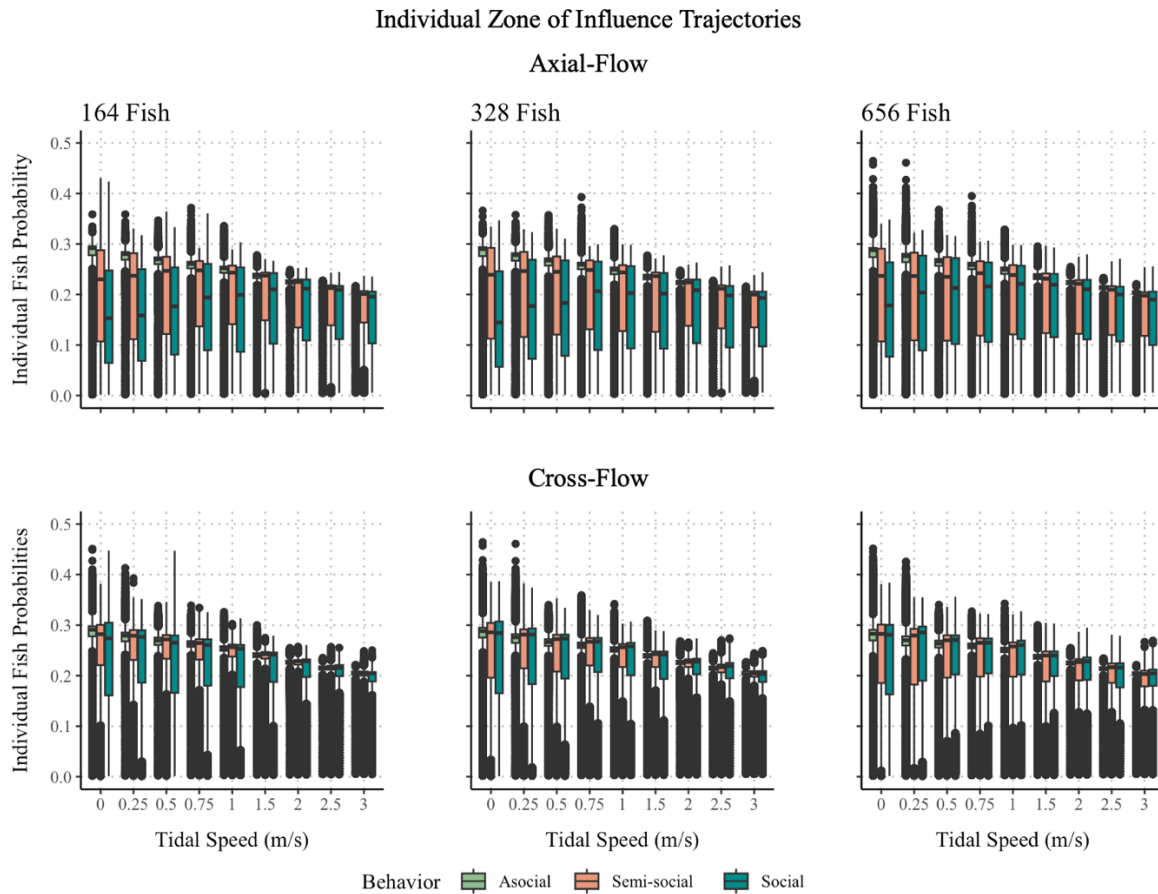


Figure A2.1: Individual fish trajectory probabilities for the zone of influence organized by turbine type (i.e., axial-flow, cross-flow), fish abundance (i.e., 164, 328, 656), and tidal speed (ms^{-1}). Probabilities are on the y-axis for each corresponding boxplot with ranges exhibiting zero to maximum probabilities per model component. Tidal speed is organized on the x-axis from 0 to 3.0 ms^{-1} . Fish behavior is organized into three categories of aggregation behavior (i.e., asocial, semi-social, social).

Zone of Influence Population Probabilities

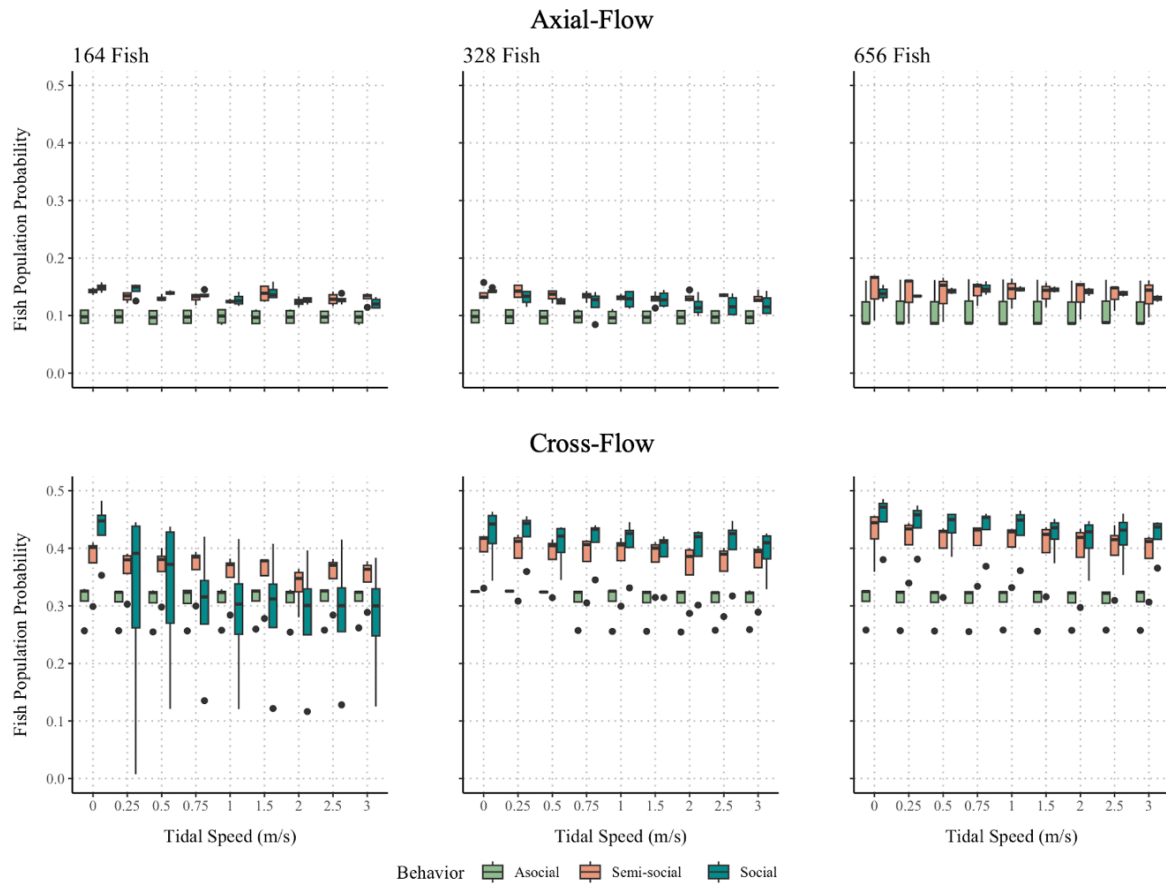


Figure A2.2: Population probabilities for the zone of influence organized by turbine type (i.e., axial-flow, cross-flow), fish abundance (i.e., 164, 328, 656), and tidal speed (ms^{-1}). Tidal speed is organized on the x-axis from 0 to 3.0 ms^{-1} . Fish behavior is organized into three categories of aggregation behavior (i.e., asocial, semi-social, social).

Individual Entrainment Trajectories

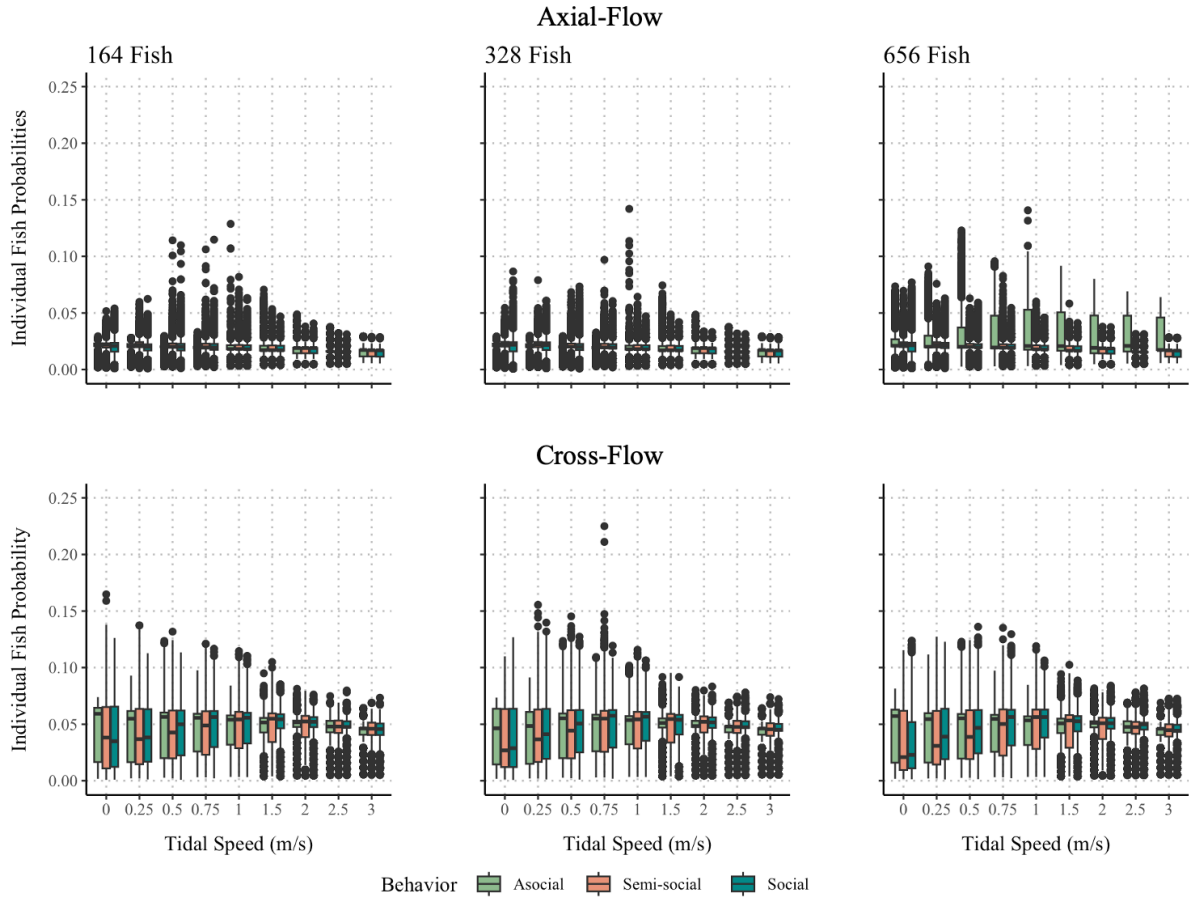


Figure A2.3. Individual fish trajectory probabilities for the entrainment component organized by turbine type (i.e., axial-flow, cross-flow), fish abundance (i.e., 164, 328, 656), and tidal speed (ms^{-1}). Probabilities are on the y-axis for each corresponding boxplot with ranges exhibiting zero to maximum probabilities per model component. Tidal speed is organized on the x-axis from 0 to 3.0 ms^{-1} . Fish behavior is organized into three categories of aggregation behavior (i.e., asocial, semi-social, social).

Entrainment Population Probabilities

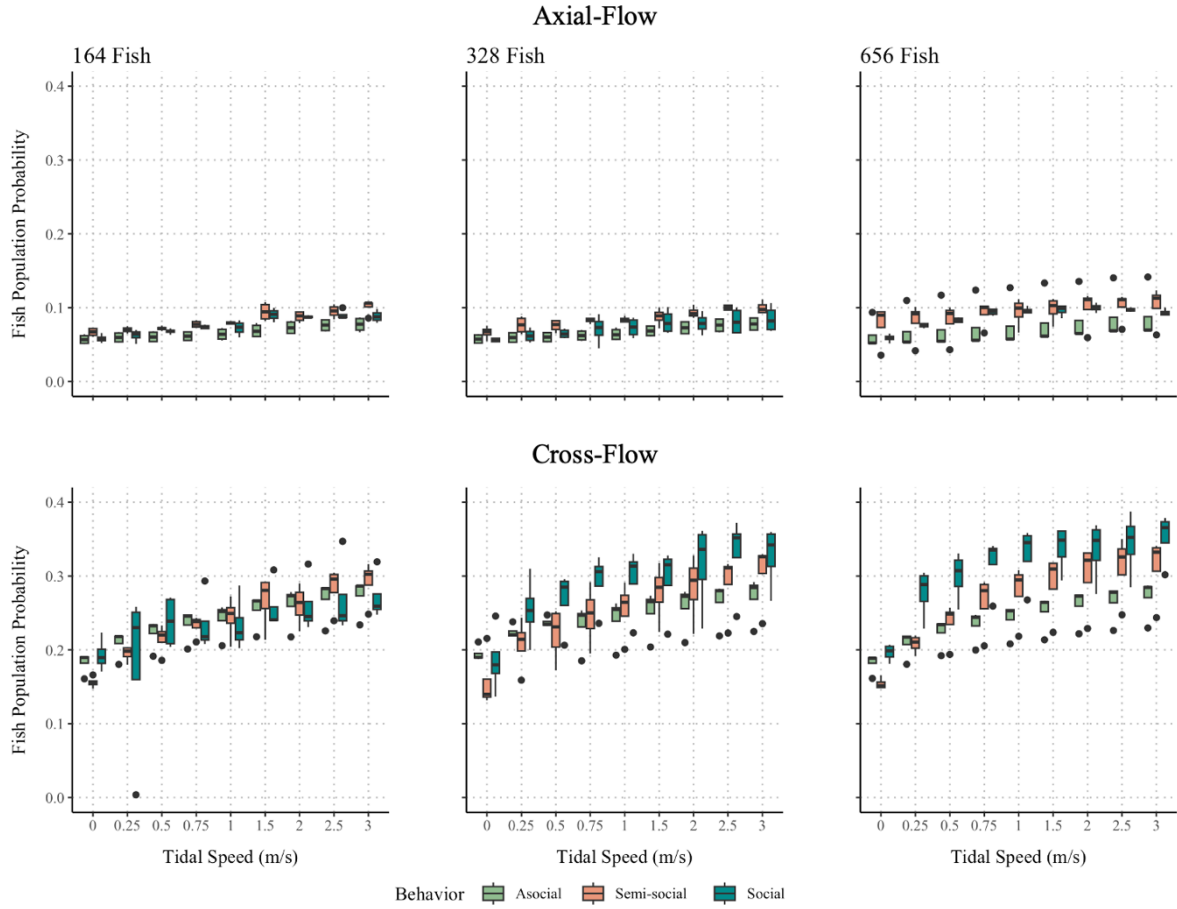


Figure A3.4: Population probabilities for the entrainment component organized by turbine type (i.e., axial-flow, cross-flow), fish abundance (i.e., 164, 328, 656), and tidal speed (ms^{-1}). Tidal speed is organized on the x-axis from 0 to 3.0 ms^{-1} . Fish behavior is organized into three categories of aggregation behavior (i.e., asocial, semi-social, social).

Individual Turbine Rotor Entry Trajectories

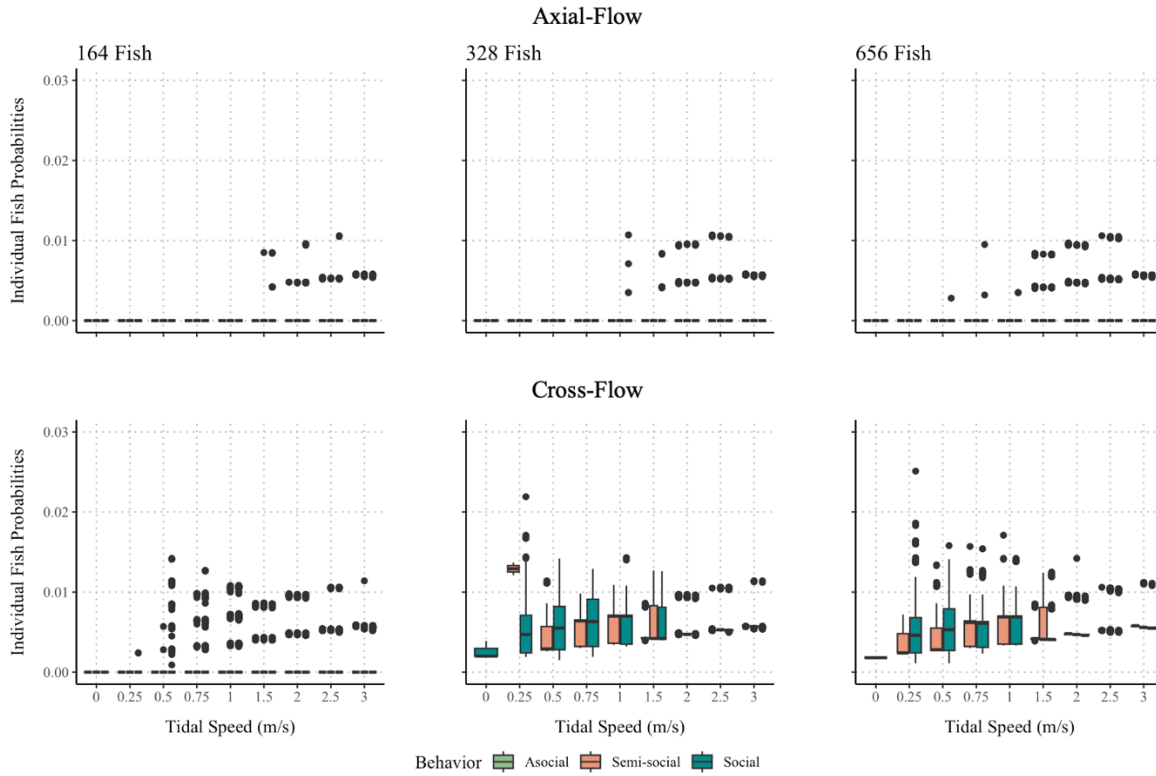


Figure A2.5: Individual fish trajectory probabilities for the turbine rotor-swept area organized by turbine type (i.e., axial-flow, cross-flow), fish abundance (i.e., 164, 328, 656), and tidal speed (ms^{-1}). Probabilities are on the y-axis for each corresponding boxplot with ranges exhibiting zero to maximum probabilities per model component. Tidal speed is organized on the x-axis from 0 to 3.0 ms^{-1} . Fish behavior is organized into three categories of aggregation behavior (i.e., asocial, semi-social, social).

Turbine Rotor Entry Population Probabilities

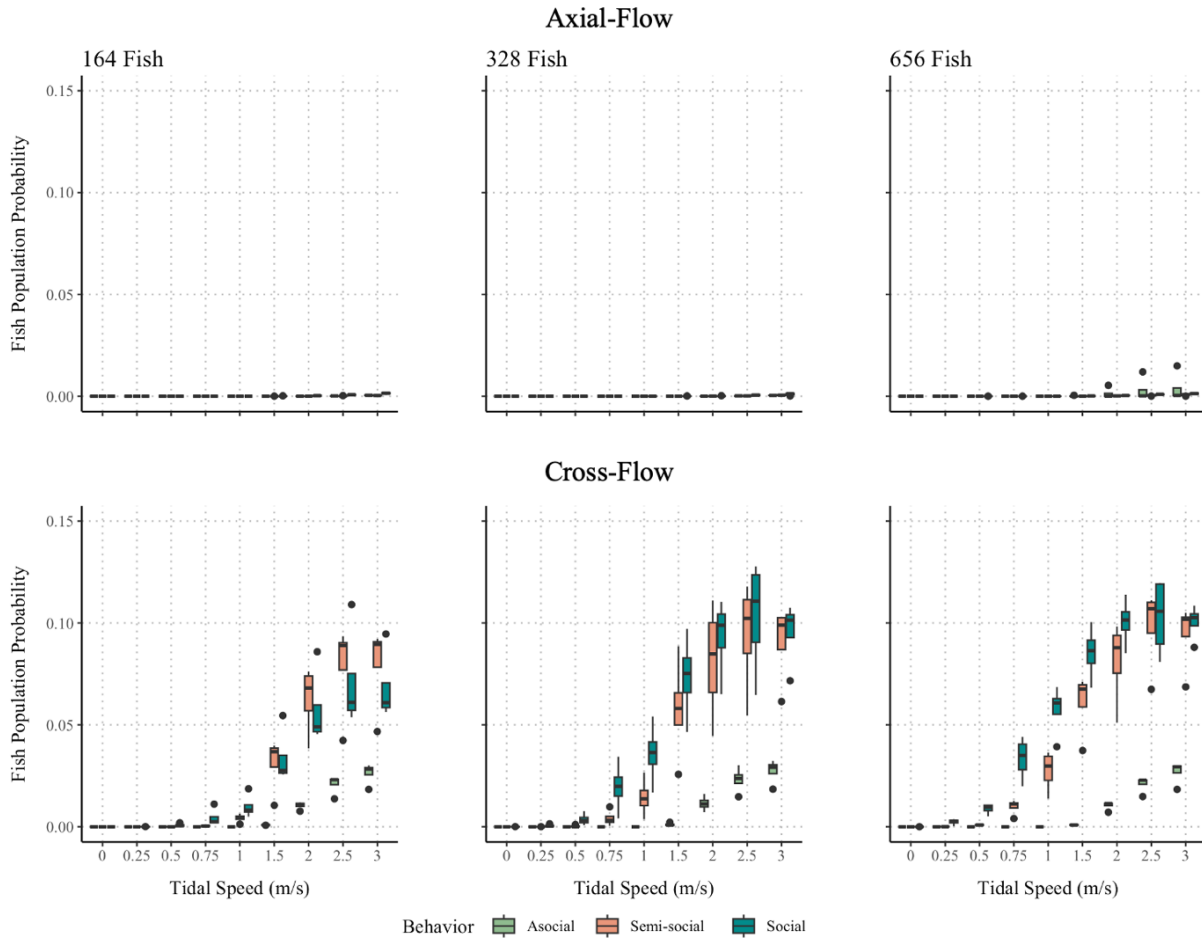


Figure A2.6: Population probabilities for the turbine rotor-swept area organized by turbine type (i.e., axial-flow, cross-flow), fish abundance (i.e., 164, 328, 656), and tidal speed (ms^{-1}). Tidal speed is organized on the x-axis from 0 to 3.0 ms^{-1} . Fish behavior is organized into three categories of aggregation behavior (i.e., asocial, semi-social, social).

Collision Population Probabilities

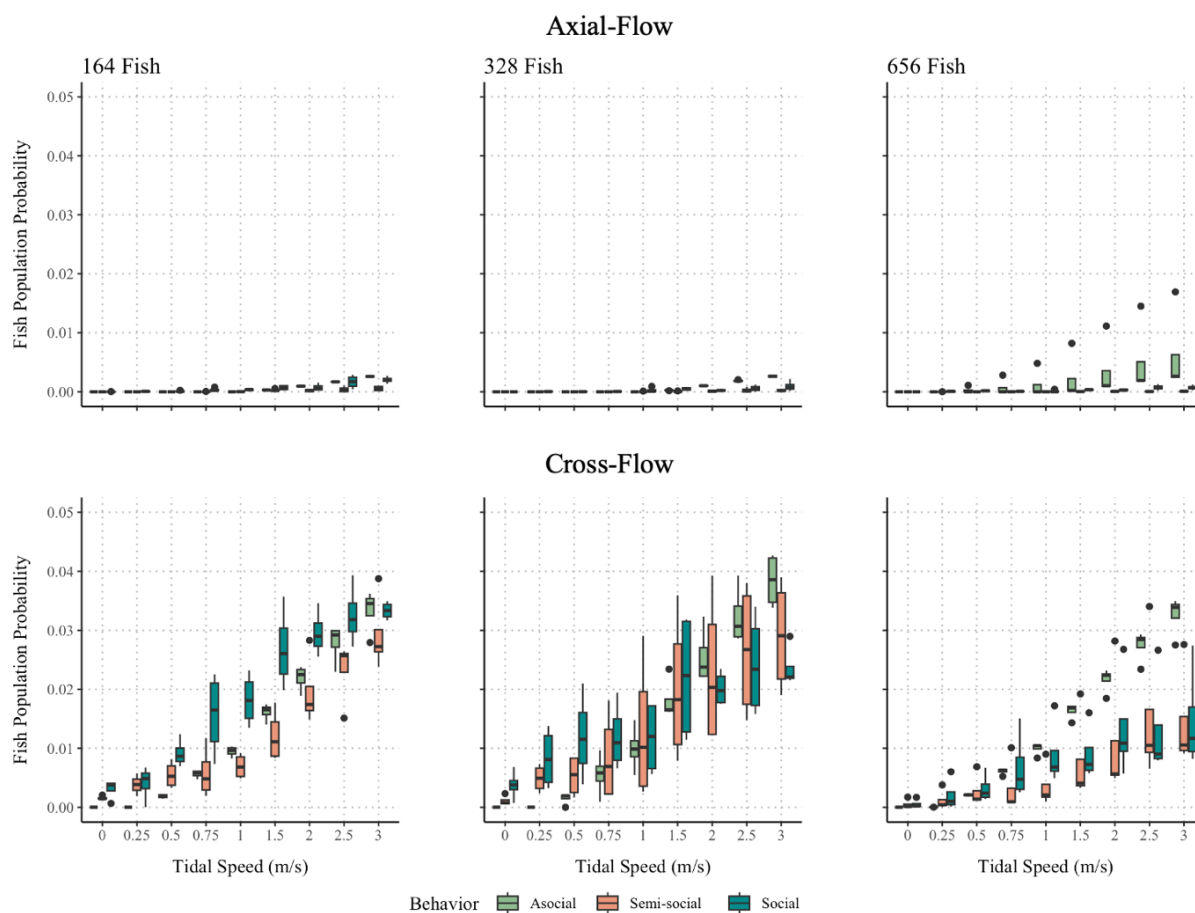


Figure A2.7: Population probabilities for collision are organized by turbine type (i.e., axial-flow, cross-flow), fish abundance (i.e., 164, 328, 656), and tidal speed (ms^{-1}). Tidal speed is organized on the x-axis from 0 to 3.0 ms^{-1} . Fish behavior is organized into three categories of aggregation behavior (i.e., asocial, semi-social, social).

Blade Strike Population Probabilities

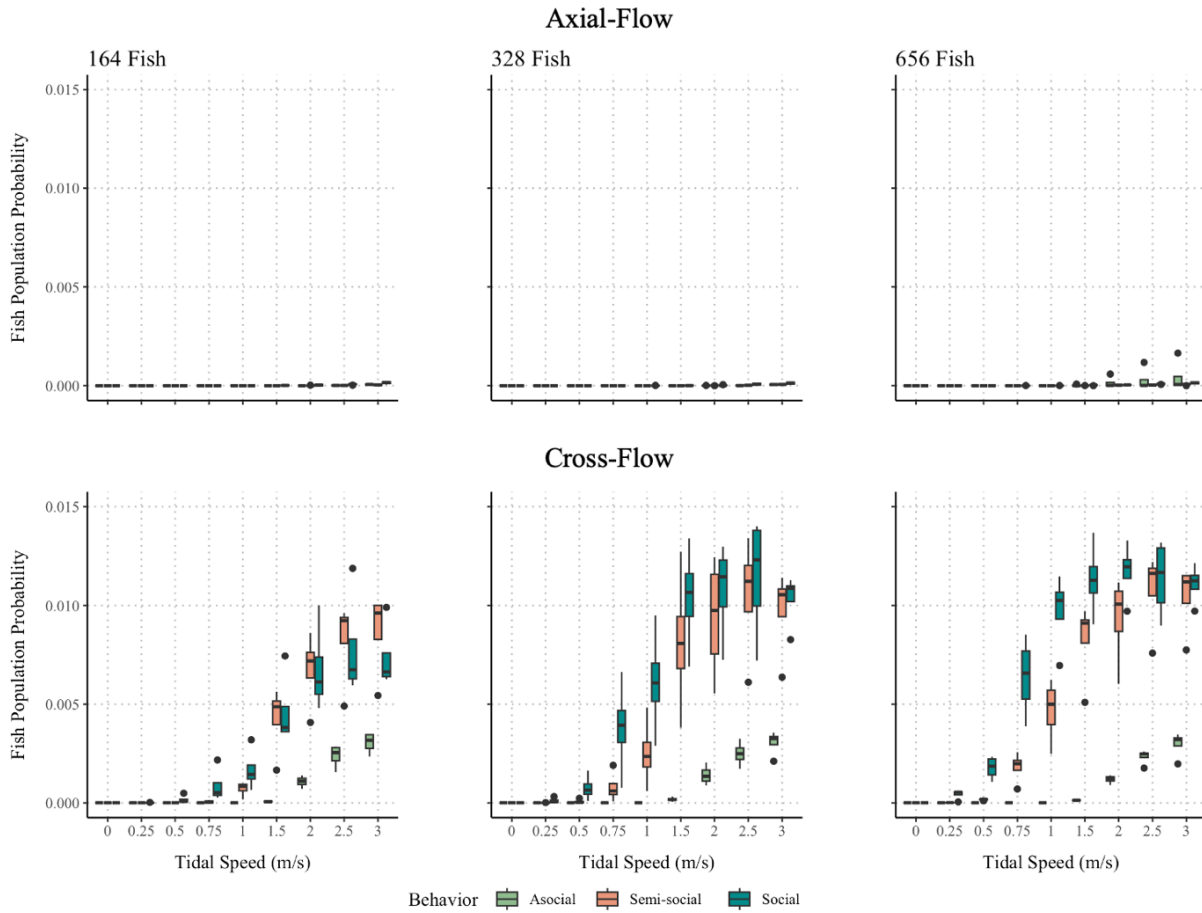


Figure A2.8: Population probabilities for blade strike are organized by turbine type (i.e., axial-flow, cross-flow), fish abundance (i.e., 164, 328, 656), and tidal speed (ms^{-1}). Tidal speed is organized on the x-axis from 0 to 3.0 ms^{-1} . Fish behavior is organized into three categories of aggregation behavior (i.e., asocial, semi-social, social).

Collision and Blade Strike Population Probabilities

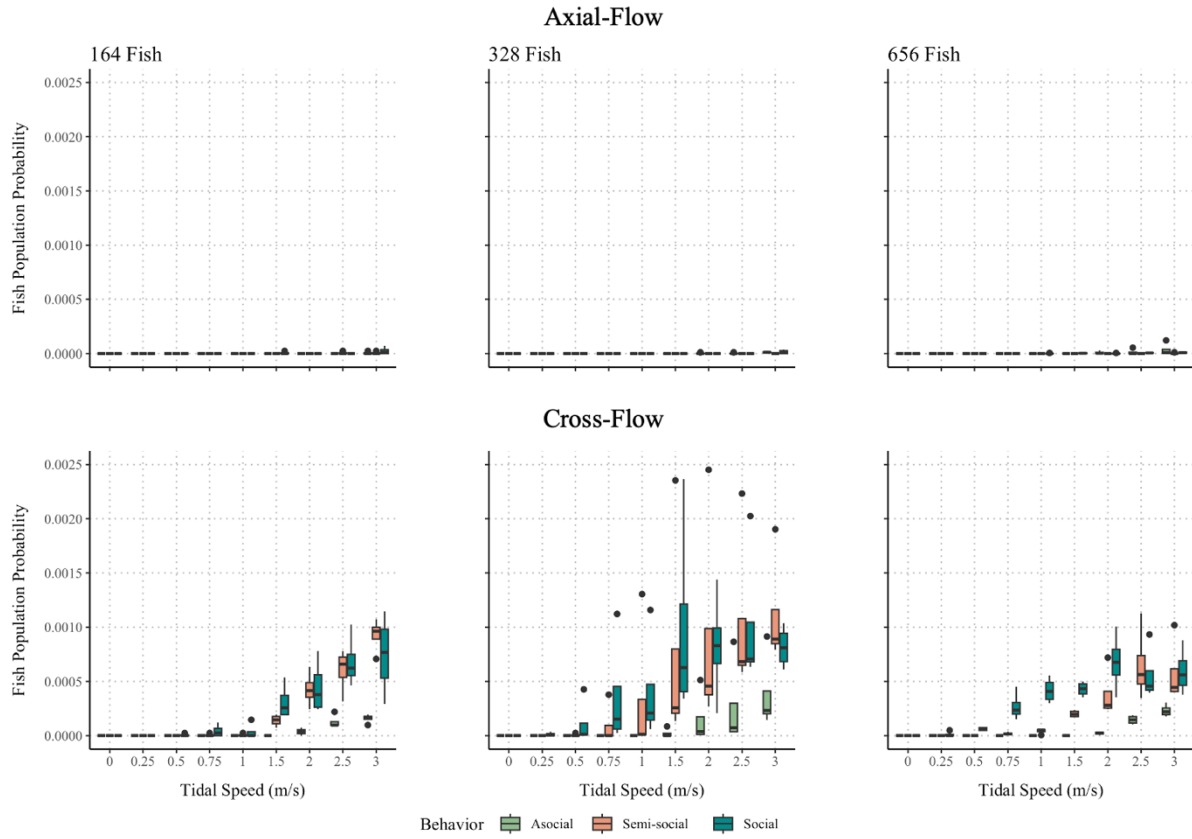


Figure A2.9: Population probabilities for sequential collision and blade strike are organized by turbine type (i.e., axial-flow, cross-flow), fish abundance (i.e., 164, 328, 656), and tidal speed (ms^{-1}). Tidal speed is organized on the x-axis from 0 to 3.0 ms^{-1} . Fish behavior is organized into three categories of aggregation behavior (i.e., asocial, semi-social, social).